BEYOND VANILLA DARK MATTER: NEW CHANNELS IN THE MULTIFACETED SEARCH FOR DARK MATTER

A DISSERTATION SUBMITTED TO THE
GRADUATE DIVISION OF THE
UNIVERSITY OF HAWAIʻI AT MĀNOA
IN PARTIAL FULFILLMENT OF THE
REQUIREMENTS FOR THE DEGREE OF

DOCTOR OF PHILOSOPHY

IN

PHYSICS

AUGUST 2014

By

David E. Yaylali

Dissertation Committee:

Jason Kumar, Chairperson
Xerxes Tata
Sandip Pakvasa
John G. Learned
Jefferey Kuhn

ACKNOWLEDGMENTS

I would like to thank Jason for the guidance, insight, and support he has provided me throughout these past years. I would also like to thank the other members of the Hawaii Theory Group, along with many other members of faculty and staff here in Watanabe Hall, for supporting me and welcoming me as one of their own. Many thanks to my collaborators and friends, Brooks and Keith. And lastly, thanks to mom and dad, to Hannah, to Jon, and Anna, to Miss Juno Crow, and to my friend Peter who lives so far away.

ABSTRACT

Though we are extremely confident that non-baryonic dark matter exists in our universe, very little is known about its fundamental nature or its relationship with the Standard Model. Guided by theoretical motivations, a desire for generality in our experimental strategies, and a certain amount of hopeful optimism, we have established a basic framework and set of assumptions about the dark sector which we are now actively testing. After years of probing the parameter spaces of these *vanilla* dark-matter scenarios, through a variety of different search channels, a conclusive direct (non-gravitational) discovery of dark matter eludes us. This very well may suggest that our first-order expectations of the dark sector are too simplistic.

This work describes two ways in which we can expand the experimental reach of vanilla dark-matter scenarios while maintaining the model-independent generality which is at this point still warranted. One way in which this is done is to consider coupling structures between the SM and the dark sector other than the two canonical types — scalar and axial-vector — leading to spin dependent and independent interactions at direct-detection experiments. The second way we generalize the vanilla scenarios is to consider multi-component dark sectors. We find that both of these generalizations lead to new and interesting phenomenology, and provide a richer *complementarity* structure between the different experimental probes we are using to search for dark matter.

TABLE OF CONTENTS

LIST OF TABLES

LIST OF FIGURES

CHAPTER 1
INTRODUCTION: VANILLA DARK MATTER AND BEYOND

There is at this point overwhelming evidence that a substantial fraction of the energy density of the universe is in the form of dark matter. Evidence of its existence has been gathered at all astronomical scales through its gravitational effects on visible matter[1]. The first convincing arguments indicating a substantial amount of "invisible" matter were given by Zwicky in 1933 [2], who studied the velocities of several galaxies within the Coma Cluster. Conservative estimates on the mass of the visible matter, based on standard expectations of the mass-to-light ratio Υ, could account for at most only ten percent of the gravitating matter in the system.

Perhaps the most well known evidence for dark matter came in the subsequent decades, by studying galactic *rotation curves*. The rotational velocity of an object in orbit around a galaxy at a radius r should scale as $v(r) \propto \sqrt{M(r)/r}$, where $M(r)$ is the mass within the orbit. If one expects that the mass profile in a galaxy should roughly trace the luminosity profile, the rotational velocity of objects orbiting at radii outside of the visible portion of the galaxy should then scale as $v(r) \propto 1/\sqrt{r}$. Instead, one finds that the velocity remains roughly constant out to much larger distances than the luminous portion of the galaxy — the rotation curve *flattens* instead of falling as expected. This then implies that the visible galaxy is only a small central region within a much larger *halo* of dark matter, with a density profile that scales as $\rho(r) \propto 1/r^2$. This effect has been observed in many galaxies, including our own [3, 4].

On even smaller scales, it has been determined that stellar velocities in the local galactic region, above and below the galactic disk, are too large to be accounted for by the gravitational potential of the matter in the disk. Recent measurements of this effect [5] have determined the DM density in the immediate vicinity of the sun to be $\rho_{\rm loc} = 0.3 \pm 0.1$ GeV/cm^3— equivalent to $\sim 3 \times 10^5$ protons in a cubic-meter box. This value is generally in agreement

[1] For a review, see [1]

with other methods of determining local dark-matter density (as reviewed in Ref. [6]), including extrapolations from the expected density profile as determined from N-body simulations (see below).

The ratio of dark matter to visible matter seems to depend on the scales and types of objects we are observing. Measurements of cosmological parameters, however, can tell us the *total* amount of dark matter in the universe, which we parametrize as $\Omega_{\rm DM} \equiv \rho_{\rm DM}/\rho_{\rm crit}$ where $\rho_{\rm crit}$ is the critical energy density needed for a flat universe.[2] The most reliable measurements of $\Omega_{\rm DM}$ come from measurements of the cosmic microwave background (CMB).

The anisotropies in the CMB spectrum are sensitive to both the total matter density $\Omega_{\rm m}$ and the total baryonic density $\Omega_{\rm b}$. These anisotropies encode the effects of baryon acoustic oscillations (BAO), which essentially can be thought of as sound waves in the primordial plasma before recombination. Gravitational attraction from overdensities in the plasma act as a restoring force to the outward radiation pressure within these overdense regions. The former effect is proportional to the total amount of gravitating matter, while the latter is proportional only to the baryonic matter which interacts with the photon gas. Density oscillations arising out of this resonating system can thus tell us about both the matter and baryon densities in the plasma, from which we can infer the total dark matter density though $\Omega_{\rm DM} = \Omega_{\rm m} - \Omega_{\rm b}$.

The anisotropies on the sky can be expanded as series of spherical harmonics, with different coefficients for each mode in the series represented by the familiar CMB *power spectrum*. It turns out [7] that the relative positions and heights of the first few peaks and troughs of this power spectrum can place precise bounds on the baryon and matter densities. The most recent measurements, determined by the Planck Collaboration [8], are $\Omega_{\rm b}h^2 = 0.02207 \pm 0.00033$ and $\Omega_{\rm DM}h^2 = 0.1196 \pm 0.0031$, corresponding to fractions of the total energy density of 4.9% and 26%, respectively.[3]

[2] We have determined that the geometry of the universe is very nearly flat ($\Omega_{\rm tot} \approx 1$), so $\Omega_i \equiv \rho_i/\rho_{\rm crit}$ conveniently gives the approximate percentage of the total energy density made up by ρ_i

[3] This measurement of the baryonic density is in good agreement with predictions from big bang nucle-

Further independent support for a large dark-matter component comes from N-body simulations of large-scale structure development in our universe. Using these computational methods allows us to study the non-linear behavior that leads to structure in universe, such as the emergence of dark matter filaments, clusters, galactic halos, and sub-halos. These simulations are valuable for two reasons. First, they tend to support the general picture of *cold* dark matter — that is, matter that is non-relativistic during the time of structure emergence in our universe. This can then place lower bounds on the mass of thermally produced dark-matter particles, and simultaneously place upper bounds on the amount of dark matter that can be made up of Standard-Model light neutrinos. Second, N-body simulations provide us with a better grasp on the shapes of the density profiles of the dark-matter halos on galactic and super-galactic scales [10]. Both of these pieces of information have important implications for direct- and indirect-detection experiments.

1.1 Vanilla Dark Matter: The usual assumptions

What we know about dark matter — as described in the previous section — is very limited. What we can take from all of the above pieces of evidence, with a good amount of confidence, is the following:

- Dark matter exists, and does not significantly interact with electromagnetic radiation.
- The density of dark matter in the universe as a whole is $\Omega_{\rm DM} \approx 0.25$, approximately five times the density of Standard-Model matter.
- Dark matter is clustered in halos around visible astronomical objects, implying that it is comprised of non-relativistic particles.
- The local density of dark matter in the solar neighborhood is $\rho_{\rm loc} \approx 0.3$ GeV/cm^3.

Beyond this, the nature of the dark sector is completely unknown. It is thus necessary, in order to make any progress, to build a general framework based on a certain set of

osynthesis [9], which independently constrain the baryon density from the observed primordial abundances of light elements to be $0.019 \leq \Omega_{\rm b} h^2 \leq 0.024$.

assumptions about the dark sector. To use a well-known adage, if we've lost our keys, it is best to first look under the illumination of the streetlight. In our case, the streetlight essentially equates to a simple particle-physics toy model for the dark-matter particles and their interactions. There exists a set of standard assumptions that go into constructing this toy model that the dark-matter community has come to accept as "the *vanilla* scenario."

One of the biggest assumptions that is typically made is that dark matter has some non-zero (non-gravitational) coupling to the Standard Model. There are several reasons why this is believed to be the case. First, there are theoretical motivations that suggest that the dark matter particle arises out of an extension of the Standard Model electroweak interactions. These *weakly interacting massive particles* (WIMPs) gained strong support after it was realized that particles characteristic of the weak scale – with masses on the order of 100 GeV and interaction strengths comparable to the electroweak interactions – will be thermally produced in the right quantities in order to account for current dark matter density in our universe. Moreover, thermal production of dark matter is itself a strong motivation for non-zero couplings between the dark sector and the Standard Model; it provides a nice and simple framework for generating the dark matter density in the early universe – the so-called *relic density*.

Another motivation for this assumption is that a significant number of "top-down" models that have been envisioned as natural extensions to the Standard Model tend to predict dark matter candidates that naturally couple to visible matter. In supersymmetric theories, the lightest supersymmetric particle (LSP) will have some non-zero coupling to the Standard Model, and is a natural DM candidate [11]: R-parity, which is usually required to prevent proton decay, ensures that the LSP is completely stable, and exotic isotope searches imply that it must be neutral (the typical candidate that is considered is the neutralino). Heavy neutrinos could also be potential dark matter candidates, and serve as obvious candidates for the typical WIMP scenario. Other common possible candidates which arise naturally in extensions to the Standard Model are the lightest T-odd particle in the so-called *little Higgs* modes with T-parity (LHT) [12] and the lightest Kaluza-Klein

particle in theories of universal extra dimensions [13], both of which couple to the Standard Model in potentially detectable ways.

We thus have a variety of possible, and reasonably well motivated, candidates for dark matter which couple to the Standard Model. The way these particles couple, however, is clearly model-dependent, proceeding through exchanges of different types of particles coupled in various different ways. In order to probe the dark sector in the most general possible way, it is thus beneficial to hide all of these model-dependent details within an *effective* dark-matter/visible-matter contact interaction. Indeed, since the interactions between the dark and visible sectors are by definition suppressed, it is somewhat natural to think that they are coupled through high-scale dynamics (*e.g.*, extremely heavy mediator-particles) which can be safely integrated out. For a (Dirac) fermionic dark-matter particle χ, such contact interactions typically involve bilinear coupling structures of the form

$$(\bar{\chi}\,\Gamma\,\chi)\,(\bar{\psi}\,\Gamma'\,\psi)\ , \tag{1.1}$$

where ψ denotes a Standard-Model particle and where Γ and Γ' represent different possible choices of Dirac gamma-matrix combinations $\{\mathbf{1},\ i\gamma^5,\ \gamma^\mu,\ \gamma^\mu\gamma^5,\ \sigma^{\mu\nu}\}$. Different choices for Γ and Γ' correspond to different Lorentz and parity properties for the underlying interactions, and can thus lead to drastically different dark-matter phenomenologies (and therefore different predictions for associated event rates) at dark matter experiments. For this reason, coupling structures which lead to attractive phenomenologies and greater event rates tend to be studied ubiquitously in the dark-matter literature, while those leading to suppressed event rates are typically neglected. As we shall see, the scalar ($\Gamma = \Gamma' = \mathbf{1}$) and axial-vector ($\Gamma = \Gamma' = \gamma_\mu\gamma^5$) couplings generally lead to the highest event rates at direct-detection experiments. Moreover, these types of couplings arise naturally when the dark matter is the LSP, which is by far the most widely studied dark matter candidate. As a result, scalar- and axial-coupled dark matter is, in a sense, synonymous with the vanilla dark matter scenario.

Another assumption that is motivated by the various top-down models mentioned above is that the dark matter particles making up $\Omega_{\rm DM}$ are of a *single species*. This arises in these scenarios due to the conservation of some new $\mathbb{Z}$-type symmetry, such as R-parity or KK-parity. In addition to these motivations, assuming a single component in the dark-sector greatly simplifies analyses and search strategies. For this reason, a vast majority of research in the field has been in the context of single-component dark matter.

We will now see how this basic single-component contact-coupled framework can be used to probe dark-matter models in a variety of different ways. By using the generality of this framework, we are able to cast a very wide net in our hunt for dark matter.

1.2 Dark Matter Complementarity

In recent years, many search techniques have been exploited in the hunt for dark matter [14–19]. These include possible dark-matter production at colliders; direct detection of cosmological dark matter through its scattering off ordinary matter at underground experiments; and indirect detection of dark matter through observation of the remnants of the annihilation of cosmological dark matter into ordinary matter at terrestrial or satellite-based experiments.

Each search technique is associated with its own set of strengths and weaknesses. Direct detection, for instance, is rather insensitive to dark matter which couples to leptons only, or to dark matter particles with a mass of ~ 5 GeV or below. In addition, the signal at direct-detection experiments is highly sensitive to the local dark-matter density and velocity distributions; although we have reasonable estimates for these quantities in the general galactic neighborhood, small fluctuations in the immediate solar region could drastically alter results. Collider production of dark matter, on the other hand, is sensitive to a wider variety dark matter couplings, and can be sensitive to models which couple DM only to leptons [20]. These experiments, however, would not be able to make a conclusive dark matter discovery since there is no way to tell whether non-interacting exotic particles that may be produced are stable on cosmological time scales (and are thus good candidates for

particles making up the cosmological dark matter density $\Omega_{\rm DM}$). Lastly, indirect detection and astrophysical probes, which are also potentially sensitive to a wide variety of DM-SM couplings, suffer from severe uncertainties in astrophysical backgrounds. With these issues in mind, a conclusive discovery of dark matter will most likely come from a complementary approach, where compatible discoveries can be confirmed by two or more of the above types of experiments.

At first glance, these different techniques may seem to rely on three independent properties of dark matter, namely its amplitudes for production, scattering, and annihilation. However, these three amplitudes are often related to each other through various crossing symmetries. As a result, the different corresponding search techniques are actually correlated with each other through their dependence on a single underlying interaction which couples dark matter to ordinary matter, and the results achieved through any one of these search techniques will have immediate implications for the others as well as for this underlying interaction. This is the origin of the celebrated **complementarity** which connects the different existing dark-matter search techniques (for a review, see Ref. [21]).

To illustrate this complementarity, let us suppose that a dark matter fermion χ can couple to a Standard-Model fermion ψ, as above, through an effective four-point interaction Lagrangian of the form

$$\mathcal{L}_{\rm eff} = c_{\chi\psi}(\bar{\chi}\Gamma^X\chi)(\bar{\psi}\Gamma^Y\psi). \tag{1.2}$$

Here, we note that since the combined bilinear structures are of dimension six, the coupling constant $c_{\chi\psi}$ must have units of (energy)$^{-2}$. It can be instructive to think of this coupling as arising from the exchange of a mediator of mass M^*, so that $c_{\chi\psi} \sim 1/M^{*2}$.

This interaction can be pictured generally by the diagram given in Fig. 1.1. This diagram now clearly illustrates that the three experimental processes – collider production, direct detection, and indirect detection – are constructed out of the exact same underlying interaction. Though the specific coupling in Eq. (1.2) describes only the $\bar{\chi}\chi \longleftrightarrow \bar{\psi}\psi$ annihilation/production process indicated by the horizontal arrows, the other directions in the diagrams can directly be found by applying crossing symmetries to the matrix element.

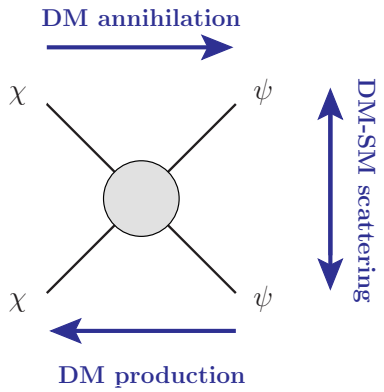

Figure 1.1: The complimentary processes that are related to each other through matrix element crossing symmetries.

Thus, though all three processes will have different rates depending on the kinematics and particle densities involved, the rates depend on fundamental theoretical parameters common to *all* processes — the coupling $c_{\chi\psi}$ between the dark matter and the Standard-Model matter, the mass m_χ of the dark matter particle, and the coupling structure of the theory, which here is encoded in the gamma matrix structures Γ^X and Γ^Y. Thus, for specific choices of these variables, we are able to predict the rates for two different processes and search for those correlated rates experimentally.

We will now briefly review each experimental process in order to see how exactly this complementarity can be applied in practice. Some of this will be reiterated in the chapters to come, when we are calculating actual rates for models and applying complementarity in practice.

1.2.1 Direct Detection

The interaction illustrated in Fig. 1.1 schematically implies that there is some non-zero probability for a dark-matter particle to scatter off of a Standard-Model particle. The aim of direct-detection experiments [15, 19] is to discover these potential scattering events within a mass of detector material as galactic-halo dark matter streams through the laboratory. Due to the extremely low cross-sections expected for these scattering events, the detector

mass typically has to be very well isolated and all backgrounds have to be known to a high precision, or strongly suppressed.

In general, there are only three observables at direct detection experiments: directionality, total event rate, and recoil energy spectra. The first of these, directionality, is extremely valuable as it can tell us the general direction of dark matter flow in the solar neighborhood. If we were to discover a dark matter signal with directionality consistent with the motion of the earth through the galaxy (including the Earths annual motion around the Sun), there would virtually be no doubt that the signal was truly dark matter and not a background.

The other two observables, total event rate and recoil energy spectra, encode all of the particle physics that direct detection experiments are able to shed light on. The recoil energy spectra – that is, the scattering rate at a detector as a function of recoil energy – are given generally by,

$$\frac{dR}{dE_R} = \frac{N\rho^{\rm loc}}{m_\chi} \int_{v_{\rm min}(E_R)}^{v_{\rm esc}} v\mathcal{F}(\vec{v}) \left(\frac{d\sigma_{\chi T}}{dE_R}\right) d^3v, \tag{1.3}$$

where N represents the number density of nuclei in the detector, m_χ represents the mass of the incoming dark-matter particle, and $\rho^{\rm loc}$ represents the matter density of dark matter in our local region of the galactic halo. Here, $\mathcal{F}(\vec{v})$ is the velocity distribution of the dark-matter particles in the reference frame of the detector. Its form is typically determined by assuming a Maxwellian distribution of velocities, with the characteristic velocity of that Maxwellian distribution given by the expected orbital velocity around the galactic center at the location of the Sun. As mentioned earlier, uncertainties and local fluctuations in both $\rho^{\rm loc}$ and $\mathcal{F}(\vec{v})$ can vastly alter the determinations of the fundamental parameters of dark-matter particles which these experiments seek to detect. Also, as indicated in Eq. (1.3), the rate depends on the local dark-matter number density $\rho^{\rm loc}/m_\chi$, so that higher-mass dark matter candidates typically lead to lower event rates.

The integration limits deserve some further clarification. The differential event rate dR/dE_R gives the rate of expected scattering events that have a specific recoil energy E_R in the detector. The lower integration limit $v_{\rm min}$ represents the minimum dark matter

velocity needed to impart this recoil energy to a target nucleus of mass m_T, and is given by $v_{\min} = \sqrt{E_R m_T / 2\mu_{\chi T}^2}$ where $\mu_{\chi T}$ is the reduced mass of the χ/nucleus system. The upper limit $v_{\rm esc}$ represents the escape velocity of the galaxy at our radius from the galactic center. It can be assumed that the bulk of the dark matter in the galactic halo is captured in stable orbits around the galactic center, which necessitates $v \lesssim v_{\rm esc}$; the upper integration limit serves as a cutoff for the otherwise continuous distribution $\mathcal{F}(\vec{v})$. It is typical to take $v_{\rm esc} \approx 550$ km/s at our radius from the galactic center.

The remaining input to the differential event rate is the differential cross section, $d\sigma_{\chi T}/dE_R$, and it is this quantity which encodes the entirety of the particle physics represented in the coupling diagram of Fig. 1.1. For now, for the purposes of illustrating complementarity between experiments, we will qualitatively describe how we translate from a coupling structure such as Eq. (1.2) to the differential cross section $d\sigma_{\chi T}/dE_R$ at a direct-detection experiment. In the following chapters, we will calculate this transition explicitly.

From quark-level to nucleus-level couplings

Since direct-detection is essentially only sensitive to dark matter which couples to nuclei, we will assume there is a four-point effective coupling of the form Eq. (1.2) which couples χ to Standard-Model quarks[4]. There are two essential steps we must take, then, before we attempt to calculate the differential χ-nucleus cross-section in terms of our fundamental coupling coefficients $c_{\chi q}$.

First, we must determine how the individual quark-level couplings translate to effective *nucleon-level* couplings. This translation is essentially encapsulated by factors $\Delta q^{(N)}$ which relate the quark-level matrix elements to the nucleon-level matrix elements:

$$\langle N_f | \bar{q} \Gamma^Y q | N_i \rangle \equiv \Delta q^{(N)} \langle N_f | \bar{N} \Gamma^Y N | N_i \rangle, \tag{1.4}$$

where $N = n, p$ is an index labeling the nucleon type as either a neutron or a proton. It is

[4]For the sensitivity of direct detection to *leptophilic* dark matter — which couples only to SM leptons — see, *e.g.*, [22, 23].

clear that, dimensionally, the $\Delta q^{(N)}$ must be pure numbers. We can thus colloquially think of the $\Delta q^{(N)}$ factors as the *contribution* of the quark q to the nucleon matrix element. The actual numerical values of the $\Delta q^{(N)}$ can be determined either experimentally or on the lattice; much more will be said of these quantities in Chapter 2.

The total effective χ-nucleon coupling then can be rewritten as

$$\mathcal{L}_{\text{eff}} = g_{\chi N}(\bar{\chi}\Gamma^X\chi)(\bar{N}\Gamma^Y N), \tag{1.5}$$

where,

$$g_{\chi N} = \sum_{q=u,d,c,\ldots} c_q \Delta q^{(N)}. \tag{1.6}$$

We can at this point make an important simplification. Since typical dark-matter velocities are of order $v \lesssim 10^{-3}$, we are justified in working in the non-relativistic regime. The full relativistic expressions for the bilinear matrix elements simplify considerably, and can be rewritten in terms of a small set of quantities such as mass, velocity, and spin. For instance, it is easily shown that the matrix element of the scalar bilinear reduces to

$$\langle\psi_f|\bar{\psi}\psi|\psi_i\rangle \to 2m_\psi(\xi_\psi^{s'})^\dagger\xi_\psi^s, \tag{1.7}$$

while, for example, the matrix element for the axial-vector bilinear reduces to

$$\langle\psi_f|\bar{\psi}\vec{\gamma}\gamma^5\psi|\psi_i\rangle \to 2m_\psi(\xi_\psi^{s'})^\dagger\vec{\sigma}\ \xi_\psi^s. \tag{1.8}$$

Here, ξ_ψ^s represents the two-component spinor corresponding to a fermion ψ of spin s. We note that, since $\frac{1}{2}(\xi_\psi^{s'})^\dagger\vec{\sigma}\ \xi_\psi^s$ is the quantum mechanical spin operator, the axial-vector coupling leads to an interaction in the non-relativistic limit which is *spin-dependent*. On the other hand, $(\xi_\psi^{s'})^\dagger\xi_\psi^s$ essentially contributes unity to the squared matrix element, so that scalar couplings involving bilinears such as Eq. (1.7) are *spin-independent*.

The final step in the calculation of the χ-nucleus differential cross-section $d\sigma_{\chi T}/dE_R$ now involves summing individual χ-nucleon couplings over the entire nucleus. We essen-

tially need the nucleus-level matrix element of the effective nucleon operators found above, $\langle T_f|\bar{N}\Gamma^Y N|T_i\rangle$, where $T_{i,f}$ represents the initial and final states of the target nucleus. For operators leading to the scalar interactions as in Eq. (1.7), the matrix element turns out to be proportional to the sum of nucleons in the target nucleus,

$$\mathcal{M} \propto \{g_{\chi p} Z + g_{\chi n}(A - Z)\}, \tag{1.9}$$

where Z and $(A - Z)$ are the number of protons and neutrons in the nucleus, respectively. Thus to probe spin-independent dark-matter interactions, experiments can take advantage of an $\mathcal{O}(A^2)$ enhancement to the cross-section by using heavier nuclei within the detector substrate.

For operators which lead to spin-dependent interactions, as in Eq. (1.8), the χ-nucleus matrix element is essentially

$$\mathcal{M} \propto \{g_{\chi p}\langle S_p\rangle + g_{\chi n}\langle S_n\rangle\}, \tag{1.10}$$

where $\langle S_N\rangle$ represents the total spin of the nucleons of type N within the nucleus. In order to be in the ground state the spins tend to anti-align, so that $\langle S_N\rangle \sim 0$ or $\langle S_N\rangle \sim \frac{1}{2}$ for nuclei with an even or odd number of nucleons N, respectively. For this reason, there are no $\mathcal{O}(A^2)$ enhancements in spin-dependent scattering, so direct-detection bounds tend to be weaker than similar bounds for spin-independent scattering.

The simple summation over nucleons described assumes coherent scattering with the entire nucleus. However, since the Compton wavelength associated with the energy transfer in direct-detection settings can be on the order of the size of the nucleus, there is some coherence loss that must be taken into account. This is accomplished through energy-dependent form factors, which vary depending on the type of interaction and target nucleus, and will be discussed further in the chapters to come.

The rather qualititive explanation above illustrates how we can probe the mass and cou-

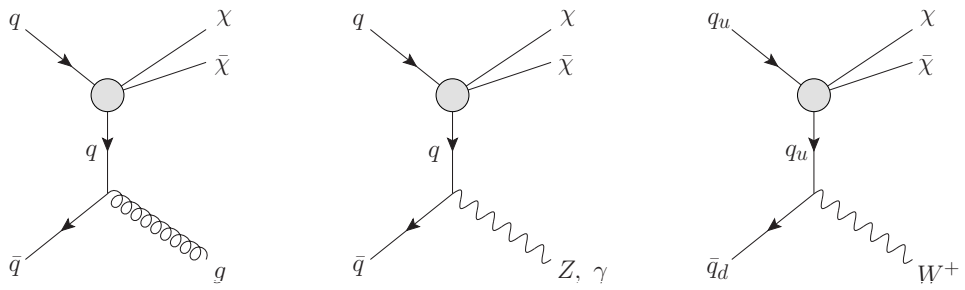

Figure 1.2: Examples of processes which can create dark matter through χ-quark couplings at hadron colliders. The Standard Model bosons which are radiated off the incoming beams are necessary in order to "see" the dark matter which is produced. By detecting these Standard Model particles, we can deduce the presence of the dark matter through missing momentum in the detector.

plings $c_{\chi\psi}$ of a given dark-matter theory by searching for nuclear recoils at direct-detection experiments.

1.2.2 Collider Production

If there is some non-zero coupling between dark matter and the Standard Model, it becomes possible to directly produce dark matter at colliders. This process is represented in the complementarity diagram of Fig. 1.1 by the left-pointing horizontal arrow.

Since, by definition, dark matter is weakly interacting, any dark matter produced by the colliding beams will free-stream through the detector and escape detection. However, if dark matter is produced in association with some visible initial-state radiation, one can search for the recoil of this visible matter off of the dark matter. Thus, the main strategy used to search for dark matter at colliders is to search for high-p_T Standard-Model particles in association with missing energy or momentum. A standard subset of event topologies is typically searched, chosen such that background subtraction is straight-forward and can be confidently performed. Examples of such channels, where dark matter couples to Standard-Model quarks, are shown in Fig. 1.2. The LHC collaborations have actively searched for such signals, reporting bounds on cross-sections for the various channels in terms of an effective theory coupling constant $c_{\chi q}$ as defined in Eq. (1.2). These collaborations have

typically chosen a small representative subset of coupling types – that is, choices for the gamma matrices Γ^X and Γ^Y – and stated bounds with respect to these choices. The subsets most often chosen are the scalar-scalar interaction ($\Gamma^X = \Gamma^Y = \mathbf{1}$) representative of spin-independent scattering at direct-detection experiments, and the axial-axial interaction ($\Gamma^X = \Gamma^Y = \gamma^\mu\gamma^5$) representative of spin-dependent scattering. To translate these bounds to other couplings structures, one needs to know how the event rates for one coupling structure translate to the rates for another. For basic phenomenological studies, this can be done by calculating rates for both coupling structures using Monte Carlo event generators, thus finding the overall scale factor between two coupling structures. Since collider searches for dark matter experiments are essentially counting experiments (in other words, the collaborations simply look for an excess number of events above background estimates), bounds on the $c_{\chi\psi}$ essentially scale as the square root of the number of events.

In this way, we can find collider bounds for essentially any contact operator — even four-point operators involving bosonic scalar- or vector-type dark matter — based on the bounds determined by the LHC collaborations on the scalar-scalar and axial-axial operator. We can thus place bounds on the various $c_{\chi\psi}$ factors in our effective field theory, subject to the condition that the effective field theory is a good description of the interaction at the energies involved at the LHC.

1.2.3 Indirect Detection

The same processes which lead to a thermal relic dark-matter component also govern annihilation processes which may be occurring at the present time. The relic density from freeze-out is reliant on the fact that annihilation rates fall below the expansion rate of the universe; annihilation ceases to occur in the early universe when this condition is reached. The universe today, however, is a very different place, and small density perturbations have caused matter to clump into dense stable regions in an otherwise expanding universe. Thus, the dark matter which has collapsed into these gravitational wells may once again achieve a density such that annihilation can again take place at observable rates. The essential dif-

ference is that, now, the reverse process of baryonic matter-antimatter annihilation cannot occur; some mechanism has created a matter-antimatter asymmetry.

Thus, in the present day, it is possible that dark matter could be undergoing pair-annihilation, producing energetic photons, neutrinos, or cosmic rays. The rate of these annihilations will depend on the square of the density of annihilating dark matter, and also the annihilation cross-section. The former can be inferred from various astrophysical measurements and N-body simulations as described above, and for certain astrophysical objects these densities are known with high confidence. The cross-section, however, is dependent on the fundamental parameters of the effective theory: mass, coupling structure, and coupling constant $c_{\chi\psi}$. Thus by searching for excesses in the flux of energetic particles from objects such as clusters or galactic cores, one can in principle place bounds on m_χ and $c_{\chi\psi}$ given a choice of coupling structure Γ^X/Γ^Y.

1.2.4 Relic Abundance

A four-Fermi interaction between dark and visible sectors assures that in the early universe, when temperatures were high enough, dark matter and Standard-Model matter were in thermal equilibrium. Through the interactions pictured in Fig. 1.1, dark matter in the primordial plasma would annihilate to Standard-Model particles, and Standard Model particles would in turn annihilate to dark matter particles. In the early universe, temperatures where high enough such that the kinematics did not favor one direction over the other; even if $m_\chi > m_\psi$, the Standard-Model particles had enough kinetic energy from the thermal bath to pair-produce heavier χ particles. As the universe continued to expand and cool, however, these mass differences became important and the dark matter fell out of equilibrium; dark matter annihilation can still proceed to lighter particles, but the opposite process which creates dark matter becomes Boltzman-suppressed.

If this were the entire picture, dark matter would continue to annihilate and its number density would asymptotically go to zero. However, since the universe is *expanding* as it cools, dark matter number density n_χ falls and thus the annihilation rate $\Gamma = n_\chi \langle \sigma_A v \rangle$,

where the term in angled brackets is the thermally-averaged annihilation cross-section times the relative velocity, falls as well. Dark matter ceases to annihilate once the annihilation rate falls below the rate of expansion, which is given by the approximate relationship $\Gamma \sim H$, where $H \equiv \dot{a}/a$ is the Hubble parameter characterizing the expansion rate.

This process is called *thermal freeze-out*, and the dark matter remaining after this process of freeze-out, if stable enough to survive to the present time, is called a *thermal relic*.[5] It turns out that, to first order, the dark-matter density $\Omega_{\rm DM}$ generated through thermal freeze-out depends only on annihilation cross-section, and not on other details such as dark-matter mass, temperature at freeze-out, or annihilation channels; indeed, to first order, density is given by $\Omega_{\rm DM}h^2 \approx 3 \times 10^{-37}$ cm^3 s$^{-1}/\langle\sigma_A v\rangle$, and annihilation cross-sections on order of $\sim$1pb tend to give relic densities on the same order of what we observe today, $\Omega_{\rm DM} \sim 0.2$.

Thus there is a clear correspondence between the coupling strength in our theory, $c_{\chi\psi}$, and the relic density that will be generated in the early universe. We should be careful to note, however, that this process will not necessarily generate the entire dark-matter density $\Omega_{\rm DM}$. If, for instance, there is more than one dark-matter species that couples to the Standard Model by such an interaction, there will be multiple contributions to the overall dark-matter density. Additionally, there could exist stable particles which do not couple at all to the Standard Model, but are created in the early universe by mechanisms of an entirely different nature. These particles, of course, would also contribute to the overall dark-matter density, diluting the components making up $\Omega_{\rm DM}$ which are thermal relics.

All this being said, it is still important to know the thermal relic-density generated in a certain model. This tells us an important piece of information: barring some caveats[6], since the density of a thermal relic must be less than the total dark matter density, we can calculate an upper bound to the coupling coefficients $c_{\chi\psi}$.

[5]Freeze-out generally needs to occur before BBN at $T \sim 100$ keV so that annihilations do not effect the formation of light elements. In the standard WIMP scenario of GeV-TeV scale masses, freeze-out occurs much earlier, at temperatures $\sim 10^1$-10^3 GeV

[6]For instance, if there are sources which dump additional entropy s into the universe after freeze-out (such that $s \to \gamma \cdot s$), the actual relic density scales down as $\Omega_{\rm DM} \to \Omega_{\rm DM}/\gamma$. This can occur, for example, during a first-order phase transition after freeze-out [24].

We now qualitatively see how the different directions in Fig. 1.1 — dark-matter production, annihilation, and scattering — can serve as independent and complementary probes of the fundamental parameters of a given dark-matter model. This can be advantageous in two different ways. First, using many different search strategies such as these can greatly increase the *coverage* of our model parameter space. For instance, direct-detection experiments are typically only sensitive to dark-matter masses above ~ 5 GeV due to the kinematics involved in χ-nucleus scattering at these experiments. Collider experiments, on the other hand, are excellent at constraining low-mass dark matter, since there is typically more than enough beam energy in the incoming partons to create lighter dark-matter particles. Thus collider experiments and direct-detection experiments are very much complementary in covering the m_χ-axis of the parameter space.

The second and perhaps more important reason why this complementarity between experiments is advantageous to us is that it provides *correlations* between the various different phenomenon. As mentioned at the beginning of this section, a claimed discovery in a single one of these experimental routes will almost assuredly be met with a certain amount of skepticism. Indeed, this is very reasonable; we have already mentioned that each experimental channel is associated with certain assumptions and potentially severe uncertainties. But dark matter complementarity provides us with "more handles to grasp," so to speak, and if a discovery in one channel is confirmed in another channel, and if the inferred values of the model parameters (m_χ, $c_{\chi\psi}$, *etc.*) are compatible with each other, the claim of a "discovery" will hold much more weight.

1.3 Beyond Vanilla Dark Matter

In this work, we will explore what happens when we relax certain assumptions that are typically made about the dark sector. The first is that the coupling structure at low energies is described purely by scalar and axial-vector four-point interactions. As we have stated, one reason why these operators tend to be studied is that they lead to two phenomenologically distinct interactions at direct-detection experiments: spin-independent interactions,

which couple to the entire nucleon content of the target nucleus, and spin-dependent interactions, which couple to the unpaired spin of the nucleons within the nucleus. We also mentioned that these interactions arise naturally in one of the most theoretically motivated dark matter candidates, the LSP. There is, however, a more straight-forward reason for considering these specific operators: for other choices of Γ^X and Γ^Y in Eq. 1.2, the matrix elements at direct detection experiments either vanish completely, or are proportional to the relative velocity $v^2 \sim 10^{-6}$. Thus, naively these interactions are simply not-detectable at direct-detection experiments, which essentially are the strongest corner-stones in the complementarity relationship.

We will see in the next chapter, however, that neglecting these *velocity-suppressed* interactions is not always justified. In some cases, specifically the case of a pseudoscalar-type coupling, the velocity suppression is countered by a strong nuclear *enhancement*. Thus entire operator structures that were previously ignored turn out to have potentially important phenomenological consequences.

Next, in Chapter 3, we will explore the new phenomenology which arises when we allow more than one dark matter particle to exist and interact with the Standard Model. We will see that the complementarity structure becomes far more rich, and more importantly, entire new channels open up, giving us new ways to probe the dark sector.

CHAPTER 2
PSEUDOSCALAR COUPLINGS: OVERCOMING VELOCITY SUPPRESSION

There are two coupling structures that are typically studied in the context of dark-matter phenomenology: the scalar and axial-vector interactions. These particular interaction structures receive the most attention because they lead to particularly strong signals at direct-detection experiments, and are thus the most efficient at probing the parameter space using the complementarity framework. Unfortunately, by neglecting other operators within the class of four-Fermi effective interactions, we are leaving many "stones unturned" in the hunt for dark matter. In particular, it may turn out that certain coupling structures which are seemingly suppressed (and thus are not considered) are actually enhanced by other factors. Such enhancements could conceivably overcome the apparent suppressions associated with these operators, implying that the contributions from such operators are not negligible after all.

In this chapter, we show that this is indeed the case for *pseudoscalar* coupling structures between dark matter and SM particles. The standard lore is that such coupling structures lead to direct-detection event rates which are suppressed relative to those associated with similar axial-vector coupling structures by factors of the χ/nucleus relative velocity $v \sim \mathcal{O}(10^{-3})$. However, the main point of this chapter is to emphasize that there is a corresponding mitigating factor that can potentially overcome this velocity suppression: the process of transitioning from a fundamental pseudoscalar *quark* coupling to an effective pseudoscalar *nucleon* coupling introduces into the corresponding dark-matter scattering rate additional factors of order $\mathcal{O}(m_N/m_q) \sim 10^3$, where $m_{q,N}$ are the masses of the corresponding quarks and nucleons. Such enhancements, for example, are not present for axial-vector interactions, which are the canonical couplings which lead to spin-dependent interactions, and which in some ways the closest cousins to the pseudoscalar interactions. In addition, we find that both axial-vector and pseudoscalar couplings are further enhanced

in cases in which the dark-matter couplings are ultimately isospin-violating, with these enhancements becoming particularly striking in the case of pseudoscalar interactions. Thus, contrary to popular lore, we conclude that pseudoscalar couplings between dark matter and Standard-Model matter can indeed be probed at dark-matter direct-detection experiments.

This chapter is organized as follows. First, we discuss the origins of the quark-to-nucleon enhancement factor that emerges for pseudoscalar interactions, and provide a careful analysis of the corresponding uncertainties that are inherent in such calculations. We also demonstrate that the possibility of isospin-violating pseudoscalar interactions only enhances these couplings further. We then proceed to present a model-independent analysis of pseudoscalar interactions at direct-detection experiments. In so doing, we also identify those portions of the corresponding dark-matter parameter space which can be probed at current and future experiments of this type.

2.1 From quarks to nucleons: Velocity suppression and nucleon enhancement for pseudoscalar couplings

We begin by discussing the matrix elements and couplings that describe the contact interactions between fermionic dark matter and ordinary Standard-Model matter. This will also serve to introduce our notation and provide a point of comparison between interactions involving different Lorentz and parity structures. Ultimately, we shall focus on the cases of axial-vector and pseudoscalar interactions. It turns out that these two cases are closely related, yet have different resulting phenomenologies.

2.1.1 General preliminaries: Quark- and nucleon-level matrix elements and pseudoscalar velocity suppression

In general, we shall assume that our dark matter is a Dirac fermion χ whose dominant couplings to the visible sector are to Standard-Model quarks through dimension-six four-

fermi contact interactions described by Lagrangian operators of the bilinear form

$$\mathcal{O}_{\chi q}^{(XY)} \;=\; \frac{c_q^{(XY)}}{\Lambda^2}\,(\overline{\chi}\Gamma^X\chi)\,(\overline{q}\Gamma^Y q)\;. \tag{2.1}$$

Here $q = u, d, s, ...$ specifies a particular species of quark, c_q is the corresponding χ/q coupling, and Λ corresponds to the mass scale of the new (presumably flavor-diagonal) physics which might generate such an effective interaction. The $\Gamma^{X,Y}$ factors are appropriate combinations of Dirac gamma-matrices, with the X and Y indices ranging over the values $\{\mathrm{S},\mathrm{P},\mathrm{V},\mathrm{A},\mathrm{T}\}$ corresponding to $\Gamma^{(\mathrm{S})} \equiv \mathbf{1}$ (scalar interaction), $\Gamma^{(\mathrm{P})} \equiv i\gamma^5$ (pseudoscalar), $\Gamma^{(\mathrm{V})} \equiv \gamma^\mu$ (vector), $\Gamma^{(\mathrm{A})} \equiv \gamma^\mu\gamma^5$ (axial vector), and $\Gamma^{(\mathrm{T})} \equiv \sigma^{\mu\nu}$ (tensor) respectively. The form in Eq. (2.1) respects $U(1)_{\mathrm{EM}}$ and $SU(3)_{\mathrm{color}}$, as required, although $SU(2)_{\mathrm{weak}}$ is broken. This is appropriate for energy and momentum scales below the electroweak scale. The operator in Eq. (2.1) is also Lorentz invariant provided that X and Y are both chosen from the set $\{\mathrm{S},\mathrm{P}\}$, the set $\{\mathrm{V},\mathrm{A}\}$, or $\{\mathrm{T}\}$; note that in this last case, there are actually two ways in which the spacetime indices on each tensor can be contracted (either $\sigma_{\mu\nu}\sigma^{\mu\nu}$ or $\epsilon_{\mu\nu\lambda\rho}\sigma^{\mu\nu}\sigma^{\lambda\rho}$) when forming the Lorentz-invariant operator. In general, the operator $\mathcal{O}_{\chi q}^{(XY)}$ will be CP-even in all Lorentz-invariant cases except when XY = SP, PS, or TT with a contraction through the ϵ-tensor. In direct-detection experiments, these operators induce scattering between the dark-matter fermion χ and the individual nucleons N of the detector substrate. The tree-level matrix element describing this χ/N scattering is therefore given by

$$\mathcal{M}_{\chi N}^{(XY)} \;=\; \sum_q \frac{c_q^{(XY)}}{\Lambda^2}\,\langle\chi_f|\overline{\chi}\Gamma^X\chi|\chi_i\rangle\,\langle N_f|\overline{q}\Gamma^Y q|N_i\rangle \tag{2.2}$$

where N denotes the particular nucleon species in question (either proton p or neutron n). Note that because the dark matter is a $U(1)_{\mathrm{EM}}$ singlet, N_i and N_f are both of the same species N and possibly differ only in their momenta and/or spins as the result of the scattering. The same will be assumed true for χ_i and χ_f, even in cases such as those in Refs. [25–28] in which the dark sector has multiple components.

In general, the nucleonic matrix element of the quark current $\overline{q}\Gamma^Y q$ cannot be evaluated

analytically within a nucleonic background defined by N_i and N_f. Indeed, to do so would require a complete understanding of the manner in which the quark degrees of freedom are directly mapped onto those of the nucleon through the non-perturbative process of confinement. However, it is conventional to make the assumption that the nucleonic matrix element of the quark current is proportional to that of the corresponding *nucleon* current in the limit of vanishing momentum transfer [29–32]:

$$\langle N_f|\overline{q}\Gamma^Y q|N_i\rangle \;\equiv\; \Delta q^{(N)}\,\langle N_f|\overline{N}\Gamma^Y N|N_i\rangle \;, \tag{2.3}$$

where $\Delta q^{(N)}$ represents a fixed constant of proportionality that encapsulates the non-perturbative physics inherent in low-energy QCD. Indeed, this constant of proportionality is assumed to depend on the quark and nucleon in question, and also the specific choice of the Dirac-matrix structure Γ^Y involved, but is otherwise assumed to be independent of all other relevant variables (such as the particular spin and velocity configurations of the initial and final N_i and N_f states). In practice, the values of $\Delta q^{(N)}$ for the different relevant cases are calculated numerically through lattice gauge-theory techniques and/or extracted experimentally. We should emphasize, however, that the relation in Eq. (2.3) holds only as an approximate phenomenological "rule of thumb", and comes with several correction terms which can be taken to be small or even vanishing in various limits. Further details can be found in Ref. [29].

Given the numerical values of $\Delta q^{(N)}$ in Eq. (2.3), the rest of the matrix element (2.2) is now in a form which can be evaluated analytically. We then find

$$\mathcal{M}_{\chi N}^{(XY)} \;=\; \frac{g_{\chi N}}{\Lambda^2}\,\langle\chi_f|\overline{\chi}\Gamma^X\chi|\chi_i\rangle\,\langle N_f|\overline{N}\Gamma^Y N|N_i\rangle \;, \tag{2.4}$$

where the final dark-matter/nucleon coupling $g_{\chi N}$ is given by

$$g_{\chi N} \;\equiv\; \sum_q c_q^{(XY)}\,\Delta q^{(N)} \;. \tag{2.5}$$

In what follows, we shall be concerned with three particular Dirac-matrix bilinears: the scalar (S), the pseudoscalar (P), and the axial vector (A). In the non-relativistic limit, the scalar bilinear matrix element behaves to leading order as

$$S: \quad \langle \psi_f | \overline{\psi} \psi | \psi_i \rangle \;\sim\; 2m_\psi \, (\xi_\psi^{s'})^\dagger \xi_\psi^s \;, \tag{2.6}$$

where ξ_ψ^s represents the two-component spinor corresponding to the fermion ψ with spin s, and where s and s' represent the spins of ψ_i and ψ_f respectively. By contrast, the corresponding pseudoscalar and axial-vector bilinear matrix elements behave to leading order as

$$\begin{aligned} P: \qquad & \langle \psi_f | \overline{\psi} \gamma^5 \psi | \psi_i \rangle \;\sim\; (\xi_\psi^{s'})^\dagger \left[(\vec{p}_f - \vec{p}_i) \cdot \vec{\sigma} \right] \xi_\psi^s \\ A: \qquad & \begin{cases} \langle \psi_f | \overline{\psi} \gamma^0 \gamma^5 \psi | \psi_i \rangle \;\sim\; 0 \\ \langle \psi_f | \overline{\psi} \vec{\gamma} \gamma^5 \psi | \psi_i \rangle \;\sim\; 2m_\psi \, (\xi_\psi^{s'})^\dagger \vec{\sigma} \, \xi_\psi^s \;, \end{cases} \end{aligned} \tag{2.7}$$

where $\vec{\sigma}$ are the Pauli spin matrices. Taking ψ to correspond to our nucleon field N, we thus see that both the pseudoscalar and axial-vector cases lead to a *spin-dependent* scattering amplitude to leading order. It is for this reason that the coefficients $\Delta q^{(N)}$ for these cases can be interpreted as characterizing the fraction of the spin of the nucleon N that is carried by the quark q. Indeed, in the case of pseudoscalar couplings, it is easy to show that *all* terms — and not just those at leading order — are spin-dependent; this follows directly from the symmetry-based observation that any CP-odd Lorentz-scalar quantity which depends on only the properties of the nucleon must involve the nucleon spin [33–36]. On the other hand, we see that the pseudoscalar case also leads to a *velocity suppression*: the corresponding matrix element in Eq. (2.7) is proportional to the velocity transfer $\Delta\vec{v} \equiv \vec{v}_f - \vec{v}_i$, which is $\mathcal{O}(10^{-3})$ for most regions of interest involving dark-matter particles originating in the galactic halo. It is this velocity suppression which lies at the root of the relative disregard for pseudoscalar interactions in the dark-matter literature.

2.1.2 An enhancement factor for pseudoscalar matrix elements

Given these observations, our next task is to determine the numerical values of the $\Delta q^{(N)}$ coefficients for the different cases of interest. In this chapter, our interest in the scalar coupling structure will be restricted to the dark-matter bilinear rather than the quark bilinear — *i.e.*, in the language of Eq. (2.1) we will wish to consider the case with $X = \mathrm{S}$, but never $Y = \mathrm{S}$. Consequently, we shall only require the values of the coefficients $\Delta q^{(N)}$ for the axial-vector ($Y = \mathrm{A}$) and pseudoscalar ($Y = \mathrm{P}$) cases. We also emphasize that we are not merely interested in the "central values" of these coefficients; we are also interested in understanding their associated statistical and experimental *uncertainties*. As we shall see, it is only by keeping track of these uncertainties that we can make solid statements about the phenomenological consequences of the different couplings in each case.

Historically, the numerical values of the $\Delta q^{(N)}$ coefficients for the axial-vector case have been extracted through nucleon-structure scattering experiments [37–41] and through lattice gauge-theory calculations [42]. The results that we shall use in this chapter are quoted in Table 2.1, and represent the most current values taken from experiment and theory. In this context, it is important to note that there are rather significant uncertainties associated with the values of the $\Delta q^{(N)}$. While the measured values for $\Delta u^{(N)}$ and $\Delta d^{(N)}$ tend to agree reasonably well with results from lattice calculations, the values for $\Delta s^{(N)}$ obtained using these two methods can differ quite significantly. In this chapter, we shall therefore adopt the $\Delta u^{(N)}$ and $\Delta d^{(N)}$ values quoted in Ref. [42], but choose values for the $\Delta s^{(N)}$ such that they lie between these lattice results and the experimentally measured values in Ref. [40], roughly two standard deviations away from the central value obtained in each analysis.

We also observe that the results quoted in Table 2.1 respect *quark-level* isospin invariance — *i.e.*, they satisfy

$$\Delta u^{(p,n)} = \Delta d^{(n,p)} \; , \qquad \Delta s^{(p)} = \Delta s^{(n)} \; . \tag{2.8}$$

This makes sense, as the results in Table 2.1 are derived in the limit in which the three

	$N = p$	$N = n$
$\Delta u^{(N)}$	0.787 ± 0.158	-0.319 ± 0.066
$\Delta d^{(N)}$	-0.319 ± 0.066	0.787 ± 0.158
$\Delta s^{(N)}$	-0.040 ± 0.03	-0.040 ± 0.03

Table 2.1: Values used in this chapter for the axial-vector coefficients $\Delta q^{(N)}$. The values for the $\Delta u^{(N)}$ and $\Delta d^{(N)}$ are taken from the recent lattice results reported in Ref. [42], while the values for the $\Delta s^{(N)}$ have been chosen such that they lie between these lattice results and the experimentally measured values in Ref. [40], roughly two standard deviations away from the central value obtained in each analysis.

light quarks are considered to be effectively massless. Likewise, in this approximation, the remaining quarks are considered to be too heavy to contribute significantly to proton-level and neutron-level couplings. Thus, in the axial-vector case, we shall additionally take

$$\Delta c^{(p,n)} = \Delta b^{(p,n)} = \Delta t^{(p,n)} = 0 \ . \tag{2.9}$$

We now turn to consider the corresponding coefficients in the pseudoscalar case. In order to distinguish these coefficients from the axial-vector coefficients above, we shall denote the pseudoscalar coefficients as $\Delta\tilde{q}^{(N)}$.

Rather than representing an independent degree of freedom, it turns out [43–45] that the pseudoscalar coefficients $\Delta\tilde{q}^{(N)}$ can actually be determined theoretically in terms of the axial-vector coefficients $\Delta q^{(N)}$. This is ultimately because a general axial-vector current $j^{\mu 5} \equiv \overline{\psi}\gamma^\mu\gamma^5\psi$ is not conserved in a theory in which $m_\psi \neq 0$, but is instead related to the pseudoscalar current $j^5 \equiv \overline{\psi}i\gamma^5\psi$ through a divergence relation of the form

$$\partial_\mu j^{\mu 5} \ = \ 2m_\psi \, j^5 + \frac{\alpha_s}{4\pi} G_{\mu\nu}\tilde{G}^{\mu\nu} \ , \tag{2.10}$$

where the final term reflects the possible additional contribution to the non-conservation of $j^{\mu 5}$ coming from a chiral anomaly (such as the chiral anomaly of QCD). Indeed, amongst all the fermion bilinears $\overline{\psi}\Gamma^Y\psi$ with which we started, it is only the axial-vector and pseudoscalar bilinears which can be connected to each other through such a direct relation.

Exploiting this observation and following Ref. [43, 44], we can now proceed to derive an

expression for the pseudoscalar coefficients $\Delta\tilde{q}^{(N)}$ in terms of the axial-vector coefficients $\Delta q^{(N)}$. We begin by noting that

$$\begin{aligned} m_N \Delta q^{(N)} \langle N_f | \overline{N} i\gamma^5 N | N_i \rangle & \\ &= \tfrac{1}{2} \Delta q^{(N)} \partial_\mu \langle N_f | \overline{N} \gamma^\mu \gamma^5 N | N_i \rangle \\ &= \tfrac{1}{2} \partial_\mu \left[\Delta q^{(N)} \langle N_f | \overline{N} \gamma^\mu \gamma^5 N | N_i \rangle \right] \\ &= \tfrac{1}{2} \partial_\mu \langle N_f | \overline{q} \gamma^\mu \gamma^5 q | N_i \rangle \\ &= m_q \langle N_f | \overline{q} i\gamma^5 q | N_i \rangle + \frac{\alpha_s}{8\pi} \langle N_f | G\tilde{G} | N_i \rangle \ . \end{aligned} \tag{2.11}$$

In Eq. (2.11), the first equality follows from the current relation (2.10) in the nucleon-level theory, where (since all nucleons are color-neutral) no QCD chiral anomaly exists. The second equality, by contrast, follows from the fact that the $\Delta q^{(N)}$ coefficients are presumed to be constants without spacetime dependence, while the third equality follows from the definition of $\Delta q^{(N)}$ as relating the nucleon-level and quark-level axial-vector matrix elements. The final equality then again follows from Eq. (2.10), now evaluated in the quark-level theory for which the QCD chiral anomaly is non-zero.

For each nucleon N, the relation in Eq. (2.11) furnishes three constraint equations (one for each of the light quarks $q = u, d, s$). However, recognizing that our three desired coefficients $\Delta\tilde{q}^{(N)}$ are nothing but the ratios between the $\langle N_f | \overline{q} i\gamma^5 q | N_i \rangle$ and $\langle N_f | \overline{N} i\gamma^5 N | N_i \rangle$ matrix elements, we see that we still have one unknown remaining, namely the matrix element involving the QCD anomaly. An additional constraint equation is therefore called for. Towards this end, it is traditional (see, *e.g.*, Ref. [43, 44]) to assume that the large-N_c chiral limit is a valid approximation. This then implies the additional constraint [46]

$$\langle N_f | \overline{u} \gamma^5 u | N_i \rangle + \langle N_f | \overline{d} \gamma^5 d | N_i \rangle + \langle N_f | \overline{s} \gamma^5 s | N_i \rangle \ = \ 0 \ . \tag{2.12}$$

In principle, we could then proceed with this as our remaining constraint equation. However, the appeal to the large-N_c limit introduces a rather significant new source of

uncertainties of order $\mathcal{O}(1/N_c)$ into our calculation. Since we wish to keep track of these uncertainties, we will ultimately need to find a way to parametrize the uncertainties inherent in the relation (2.12). We shall therefore write Eq. (2.12) in the modified form

$$\begin{aligned} &\langle N_f|\overline{u}\gamma^5 u|N_i\rangle + \langle N_f|\overline{d}\gamma^5 d|N_i\rangle + \langle N_f|\overline{s}\gamma^5 s|N_i\rangle \\ &\qquad = \ \eta\,\langle N_f|\overline{N}\gamma^5 N|N_i\rangle \end{aligned} \tag{2.13}$$

where the right side of this equation is designed to reflect this uncertainty, with the numerical coefficient η assumed to have a vanishing central value but a relatively large uncertainty $\delta\eta \sim \mathcal{O}(1/N_c)$.

This system of equations (2.11) and (2.13) may now be solved for the coefficients $\Delta\tilde{q}^{(N)} \equiv \langle N_f|\overline{q}i\gamma^5 q|N_i\rangle/\langle N_f|\overline{N}i\gamma^5 N|N_i\rangle$ as well as an analogous anomaly coefficient

$$\Delta\tilde{G}^{(N)} \ \equiv \ \frac{\alpha_s}{8\pi}\,\frac{\langle N_f|G\tilde{G}|N_i\rangle}{\langle N_f|\overline{N}i\gamma^5 N|N_i\rangle} \ . \tag{2.14}$$

The results are then given by

$$\begin{aligned} \Delta\tilde{q}^{(N)} \ &= \ \frac{m_N}{m_q}\left[\Delta q^{(N)} - X^{(N)}\right] \\ \Delta\tilde{G}^{(N)} \ &= \ m_N\, X^{(N)} \ , \end{aligned} \tag{2.15}$$

where we have defined

$$X^{(N)} \ \equiv \ \left(\sum_{q=u,d,s}\frac{1}{m_q}\right)^{-1}\left[\left(\sum_{q=u,d,s}\frac{\Delta q^{(N)}}{m_q}\right) - \frac{\eta}{m_N}\right] \ . \tag{2.16}$$

As we see in Eq. (2.15), the natural scale of the pseudoscalar $\Delta\tilde{q}^{(N)}$ coefficients is greater than the natural scale of the axial-vector $\Delta q^{(N)}$ coefficients by a factor of m_N/m_q. This effect thus tends to *enhance* the pseudoscalar couplings relative to the axial-vector couplings, thereby giving us hope that we might eventually be able to overcome the velocity suppression that afflicts the case of pseudoscalar scattering.

It is perhaps worth pausing to discuss the theoretical origin of this enhancement factor. In general, the definition of the $\Delta q^{(N)}$ coefficients in Eq. (2.3) suggests that these coefficients are fractional quantities which describe "how much" of some physical quantity associated with the nucleon N can be attributed to a constituent quark q. For example, in the case of the axial-vector coefficients, this physical quantity is spin, and the corresponding $\Delta q^{(N)}$ coefficient is known as a spin fraction. Naïvely, this would lead one to expect that the quantities $\Delta q^{(N)}$ should be relatively small, and certainly less than one. However, there is also another feature whose effects are reflected in the magnitudes of these coefficients: this is the difference in the intrinsic overall normalizations associated with the quark and nucleon fields q and N respectively. Indeed, as is conventional, each field q or N is normalized to its mass so that the corresponding state kets will satisfy relations such as $\langle q|q\rangle = 2m_q$ and $\langle N|N\rangle = 2m_N$ [or equivalently, relations such as those in Eq. (2.6)]. Thus, quantities such as the $\Delta q^{(N)}$ coefficients which convert from quark currents to nucleon currents will also intrinsically include factors that reflect this change in normalization.

Given this, it might be tempting to identify the pseudoscalar enhancement factor m_N/m_q appearing in Eq. (2.15) as reflecting this second contribution, namely a change in normalization. However, we can easily see that this is *not* the case: the axial-vector coefficients $\Delta q^{(N)}$ and the pseudoscalar coefficients $\Delta\tilde{q}^{(N)}$ each already intrinsically incorporate such normalization factors, yet our enhancement factor in Eq. (2.15) is one which rescales our pseudoscalar coefficients *relative to the axial-vector coefficients.* Indeed, this is an *extra* enhancement which emerges *beyond* the mere effects of normalization, and which ultimately reflects the fact that the pseudoscalar and axial-vector coefficients are locked together as a single degree of freedom through a relation such as that in Eq. (2.10). Or, phrased somewhat differently, the factor of $2m_\psi$ which appears in Eq. (2.10) — and which ultimately leads directly to our enhancement factor in Eq. (2.15), thereby driving the $\Delta\tilde{q}^{(N)}$ coefficients above unity — follows not from a normalization but rather from an *equation of motion*. Thus, our enhancement factor reflects far more than mere normalization conversion; it is instead deeply rooted in the dynamics of the quark and nucleon fields and the fact that their

	$N = p$	$N = n$
$\Delta\tilde{u}^{(N)}$	110.55 ± 21.87	-108.03 ± 21.33
$\Delta\tilde{d}^{(N)}$	-107.17 ± 21.14	108.60 ± 21.29
$\Delta\tilde{s}^{(N)}$	-3.37 ± 1.01	-0.57 ± 0.78
$\Delta\tilde{G}^{(N)}$	(395.2 ± 124.4) MeV	(35.7 ± 95.4) MeV

Table 2.2: Numerical values for the pseudoscalar coefficients $\Delta\tilde{q}^{(N)}$, as obtained from Eq. (2.15). Details concerning the calculation of these quantities and their associated uncertainties are discussed in the text. It is readily observed that these pseudoscalar coefficients $\Delta\tilde{q}^{(N)}$ are larger than the corresponding axial-vector coefficients $\Delta q^{(N)}$ in Table 2.1 by a factor of $\mathcal{O}(10^2 - 10^3)$. This can enhance the dark-matter/nucleon scattering amplitudes associated with pseudoscalar interactions, and thereby potentially overcome the velocity suppression that would otherwise render such cases unobservable in direct-detection experiments.

corresponding pseudoscalar and axial-vector currents are tied together through Eq. (2.10).

Using the algebraic results in Eq. (2.15) and the numerical results in Table 2.1, we can evaluate the $\Delta\tilde{q}^{(N)}$ coefficients explicitly. Our results, along with associated uncertainties, are shown in Table 2.2. As we see, the pseudoscalar $\Delta\tilde{q}^{(N)}$ coefficients are indeed larger than the corresponding axial-vector $\Delta q^{(N)}$ coefficients in Table 2.1 by a factor of $\mathcal{O}(10^2 - 10^3)$ in each case, as promised. Indeed, as we shall demonstrate below, it is precisely the relatively large size of the pseudoscalar coefficients $\Delta\tilde{q}^{(N)}$ which compensates for the velocity suppression. For these numerical calculations, we have taken $\eta = 0.0 \pm 0.33$, as discussed above, and we have taken the masses of the light quarks (and their associated uncertainties) from Ref. [9]. In particular, we have taken $m_u = 2.3 \pm 0.7$ MeV, $m_d = 4.8 \pm 0.5$ MeV, and $m_s = 95 \pm 5$ MeV, corresponding to the quark masses at the renormalization scale $\mu = 2$ GeV in the $\overline{\text{MS}}$ renormalization scheme, and then rescaled each mass and uncertainty by a factor of 1.35 in order to account for the effect of renormalization-group running down to the scale $\mu \approx 1$ GeV appropriate for dark-matter/nucleon scattering [9]. All uncertainties were then added together in quadrature in order to produce the final uncertainties quoted in Table 2.2.

As evident from Table 2.2, the results for the pseudoscalar $\Delta\tilde{q}^{(N)}$ coefficients no longer respect quark-level isospin invariance, as defined in Eq. (2.8). [In this connection we observe that quark-level isospin invariance would also require $\Delta\tilde{G}^{(p)} = \Delta\tilde{G}^{(n)}$.] This is a clear distinction relative to the axial-vector case in Table 2.1, but there are several ways in

which to understand this result. At an algebraic level, the breaking of quark-level isospin invariance arises because the transition from the axial-vector coefficients to the pseudoscalar coefficients explicitly involves the quark masses; by contrast, the axial-vector coefficients were derived under approximations in which the light quarks are effectively treated as massless. Or, phrased somewhat differently, the leading terms in the axial-vector matrix elements are independent of the quark masses; it is only the subleading terms which depend on these masses explicitly. This is different from the situation one faces in dealing with the pseudoscalar matrix elements, for which the leading terms are already mass dependent. On a more physical level, this difference can alternatively be understood as arising from the fact that the axial-vector current is somewhat special in that its matrix element essentially counts the number of fermions minus anti-fermions, weighted by chirality and normalized to the mass of the nucleon bound state. [This is analogous to the vector-current matrix element, which also counts the normalized number of fermions minus anti-fermions but without a chirality weighting.] As a result, the leading-order results in the axial-vector case depend on the number and charges of the parton constituents, but not their masses. This is to be contrasted with the pseudoscalar matrix elements, for which an additional quark mass dependence can arise. It should also be noted that while the uncertainties quoted in Table 2.2 are reliable in terms of their approximate overall magnitudes, there are certain effects which we have not taken into account which might alter these results slightly. Such effects will be discussed more fully as part of an exhaustive uncertainty analysis in Ref. [47]. For example, we have treated the uncertainties in Table 2.1 for the axial-vector $\Delta q^{(N)}$ coefficients as independent of each other (*i.e.*, uncorrelated), but in truth (see, *e.g.*, Ref. [32]) the $\Delta u^{(N)}$ and $\Delta d^{(N)}$ coefficients are actually extracted as linear combinations of two more fundamental variables $a_3^{(N)}$ and $a_8^{(N)}$. It is actually the uncertainties on these latter variables which are independent, not those on the $\Delta q^{(N)}$ coefficients. Likewise, the uncertainties on the quark masses are also not independent, as these masses are typically extracted in terms of a single reference quark mass (typically that of the down quark) and the ratios of the other quark masses relative to this reference mass. The truly independent uncertainties

are therefore those for the down-quark mass and the corresponding ratios. Moreover, the uncertainties on the quark masses are not necessarily Gaussian, since they typically have both systematic and random contributions. Combining these into a single uncertainty, as we have done here, and then treating this single uncertainty as Gaussian when performing a quadrature-based analysis represents yet another approximation. Indeed, η is an example of a variable whose uncertainty is completely systematic rather than experimental, yet its uncertainty is being treated as if were Gaussian as well. Finally, there is even some leeway concerning how one treats isospin symmetry in a rigorous uncertainty analysis. Isospin symmetry, as mentioned above, is usually invoked in order to relate quantities such as $\Delta u^{(p)}$ and $\Delta d^{(n)}$ — indeed, it is typically the case that these quantities are not measured independently. As a result of this presumed isospin symmetry, these quantities are necessarily quoted as having the same central values and same quoted uncertainties, as indicated in Table 2.1. However, it is not clear whether these uncertainties should be treated as independent or correlated when performing a quadrature-based uncertainty analysis of the sort we are performing here. While isospin symmetry would dictate that these uncertainties be treated as completely correlated, we know that isospin symmetry is only approximate in nature. Indeed, as mentioned above, the results in Table 2.2 for the central values of our pseudoscalar $\Delta\tilde{q}^{(N)}$ coefficients already fail to respect isospin symmetry because of their explicit dependence on the light-quark masses. We have therefore opted to treat the uncertainties in Table 2.1 as completely independent and uncorrelated.

Despite these observations, the uncertainties quoted in Table 2.2 are correct in terms of their overall magnitudes. It is also evident that the pseudoscalar uncertainties quoted in Table 2.2 are somewhat larger, in relative terms, than the corresponding axial-vector uncertainties quoted in Table 2.1. This is partially due to the dependence of the pseudoscalar results on a constraint which stems from a large-N_c approximation. As a result of these larger uncertainties, we see that certain quantities in Table 2.2, such as $\Delta\tilde{s}^{(n)}$ and $\Delta\tilde{G}^{(n)}$, are actually consistent with zero. As we shall see, these results will lead to considerably larger uncertainties for our eventual pseudoscalar dark-matter/nucleon couplings.

Finally, we now turn to the pseudoscalar $\Delta\tilde{q}^{(N)}$ coefficients for the heavy quarks $q = Q \equiv c, b, t$. As we shall see, these quantities will be relevant if our dark matter couples to such quarks. In the axial-vector case, the analogous coefficients were taken to be zero, reflecting the fact that such quarks are heavy and make only negligible contributions to axial-vector couplings. For pseudoscalar couplings, by contrast, the situation is different. Because of the current-algebra relation in Eq. (2.10), we see that the pseudoscalar current is related to the *derivative* of a different current involving the same heavy fermions. However, if the fermions in question are sufficiently heavy, they will have no dynamics and this derivative must vanish. We thus obtain the relation

$$2m_Q\langle N_f|\overline{Q}i\gamma^5 Q|N_i\rangle \;=\; -\frac{\alpha_s}{4\pi}\langle N_f|G\tilde{G}|N_i\rangle \;, \tag{2.17}$$

from which we see that

$$\begin{aligned}\langle N_f|\overline{Q}i\gamma^5 Q|N_i\rangle &= -\frac{1}{m_Q}\,\frac{\alpha_s}{8\pi}\langle N_f|G\tilde{G}|N_i\rangle \\ &= -\frac{1}{m_Q}\Delta\tilde{G}^{(N)}\langle N_f|\overline{N}i\gamma^5 N|N_i\rangle \;,\end{aligned} \tag{2.18}$$

where the values of $\Delta\tilde{G}^{(N)}$ are given algebraically in Eq. (2.15). We thus find that

$$\Delta\tilde{Q}^{(N)} \;=\; -\frac{1}{m_Q}\Delta\tilde{G}^{(N)} \;. \tag{2.19}$$

2.1.3 Pseudoscalar dark-matter/nucleon couplings and the effects of isospin violation

We now turn to the actual quantities $g_{\chi N}$ which parametrize how the dark-matter fermion χ couples to nucleons N in the case of pseudoscalar interactions. As evident in Eq. (2.5), these effective couplings $g_{\chi N}$ are directly determined in terms of the $\Delta\tilde{q}^{(N)}$ coefficients for

both light and heavy quarks:

$$g_{\chi N} \;=\; \sum_{q=u,d,s} c_q \Delta\tilde{q}^{(N)} - \sum_{Q=c,b,t} \frac{c_Q}{m_Q} \Delta\tilde{G}^{(N)} \;, \tag{2.20}$$

where the numerical values of the $\Delta\tilde{q}^{(N)}$ and $\Delta\tilde{G}^{(N)}$ coefficients are listed in Table 2.2.

The only task remaining, then, is to determine the values for the quark couplings c_q (henceforth taken to collectively denote the couplings for both light and heavy quarks). Of course, the expression in Eq. (2.20) for the $g_{\chi N}$ is completely general and applicable for any choice of operator coefficients c_q in the fundamental theory. In principle, any assignment of the c_q consistent with phenomenological constraints is therefore permitted. However, for concreteness, we shall here focus primarily on three particular benchmark scenarios:

- *Scenario I*: The case in which the c_q for all up-type quarks take a common value $c_u = c_c = c_t$ and the c_q for all down-type quarks likewise take a (potentially different) common value $c_d = c_s = c_b$. For this scenario, we parametrize these two independent operator coefficients in terms of a mass scale $M_{\rm I}$ and an angle θ such that $c_u/\Lambda^2 = \cos\theta/M_{\rm I}^2$ and $c_d/\Lambda^2 = \sin\theta/M_{\rm I}^2$. It then follows that $\tan\theta = c_d/c_u$ and $M_{\rm I}^2 = \Lambda^2/\sqrt{c_u^2 + c_d^2}$. Note that for $\theta = \pi/4$, this coupling structure respects quark-level isospin invariance. Varying θ will thus allow us to study the effects of isospin violation in a continuous fashion.

- *Scenario II*: A generalization of the oft-studied case in which the c_q are proportional to the Yukawa couplings y_q between the quarks and the SM Higgs boson, and thus to m_q. This scenario is motivated by the minimal-flavor-violation (MFV) assumption that the quark Yukawa couplings are wholly responsible for flavor violations. The generalization we consider here is one in which the c_q for the up-type quarks may also be scaled by an overall multiplicative factor relative to the c_q for the down-type quarks. Specifically, for this scenario, we define a mass scale $M_{\rm II}$ and an angle θ such that $c_q/\Lambda^2 = m_q\cos\theta/M_{\rm II}^3$ for up-type quarks and $c_q/\Lambda^2 = m_q\sin\theta/M_{\rm II}^3$ for down-type quarks. It then follows that $\tan\theta = (c_d m_u)/(c_u m_d)$ and

$M_{\rm II}^3 = \Lambda^2/\sqrt{(c_u/m_u)^2 + (c_d/m_d)^2}$, where $c_u/m_u = c_c/m_c = c_t/m_t$ and $c_d/m_d = c_s/m_s = c_b/m_b$.

- *Scenario III*: The related case in which the c_q are non-vanishing only for the first-generation quarks — *i.e.*, in which c_u and c_d are arbitrary, but in which $c_s = c_c = c_b = c_t = 0$. For this scenario, we likewise define $M_{\rm III}$ and θ such that $c_u/\Lambda^2 = m_u \cos\theta/M_{\rm III}^3$ and $c_d/\Lambda^2 = m_d \sin\theta/M_{\rm III}^3$. This coupling structure is of particular interest from a direct-detection perspective, implying that c_u and c_d uniquely determine the effective dark-matter/nucleon couplings $g_{\chi p}$ and $g_{\chi n}$ in Eq. (2.21), and *vice versa*. Moreover, with the couplings for the second- and third-generation quarks set to zero, this scenario is the only one which does not involve couplings which are essentially irrelevant for direct detection. Since non-zero couplings for second- and third-generation quarks could potentially have a significant effect on the rates for dark-matter production at colliders [48], this scenario is therefore in some sense the most "conservative" in that it does not assume any channels which might enhance collider signatures without affecting direct-detection signals. Study of this scenario will therefore lead to the most conservative set of limits consistent with collider data.

We emphasize that these three scenarios represent physically distinct coupling structures between χ and the SM quarks. It is for this reason that each scenario has been associated with its own independent mass scale above.

Given these three scenarios, we can now proceed to examine the behavior of our pseudoscalar dark-matter/nucleon couplings as functions of θ in each scenario. For Scenario I, the results in Table 2.2 yield the effective pseudoscalar couplings

$$\begin{aligned} g_{\chi p} &= 110.2\cos\theta - 110.6\sin\theta \\ g_{\chi n} &= -108.1\cos\theta + 108.0\sin\theta\ . \end{aligned} \tag{2.21}$$

Likewise, given the uncertainties in Table 2.2, we find that the associated *uncertainties* in these couplings are given by rather complicated expressions which can be extremely well

approximated as

$$\begin{aligned} \delta g_{\chi p} &\approx \left|21.79\cos\theta - 21.88\sin\theta\right| \\ \delta g_{\chi n} &\approx \left|21.32\cos\theta - 21.33\sin\theta\right| . \end{aligned} \tag{2.22}$$

We immediately note that both the couplings *and* their associated uncertainties are nearly vanishing at the quark-level isospin-preserving point $\theta = \pi/4$. Alternatively, given the couplings in Eq. (2.21), we can solve for the value θ^* at which *nucleon-level* isospin preservation takes place — *i.e.*, the value θ^* at which $g_{\chi p} = g_{\chi n}$. We find that in this scenario, the nucleon-level isospin-preserving point is extremely close to the quark-level isospin-preserving point, with only a very small net displacement $\theta^* - \pi/4 \approx -8.45 \times 10^{-4}$ radians.

At the nucleon-level isospin-preserving point, we find that $g_{\chi p} = g_{\chi n} \approx -0.155 \pm 0.25$ — a value consistent with zero. This is remarkable, representing a situation in which dark matter couples to quarks, but not to nucleons! Moreover, this is to be compared with the couplings that emerge for other, isospin-violating values of θ. For example, we find that the proton coupling takes the value $|g_{\chi p}| \approx 110.6 \pm 21.9$ at $\theta = \pi/2$, and reaches a maximum value $|g_{\chi p}| \approx 156.2 \pm 30.9$ at $\theta \approx 3\pi/4$. The behavior of the neutron coupling $|g_{\chi n}|$ is similar. Thus, relative to the central values of these couplings at the isospin-preserving point $\theta = \theta^*$, we see that these couplings experience a huge enhancement which can grow as large as a factor of 10^3!

We therefore conclude that isospin violation in Scenario I produces a huge enhancement in the corresponding pseudoscalar proton and neutron couplings. This is the direct result of the relatively large pseudoscalar coefficients $\Delta\tilde{q}^{(N)}$ in Table 2.2, operating within the framework of the particular quark coupling structure associated with Scenario I. However, it is important to stress that there is nothing intrinsic to the coupling structure of Scenario I by itself which causes such large proton and nucleon couplings to emerge. For example, as an algebraic exercise, we can calculate the proton and neutron couplings that would emerge under Scenario I in the *axial-vector* case — *i.e.*, using the axial-vector coefficients $\Delta q^{(N)}$

in Table 2.1 rather than the pseudoscalar coefficients $\Delta\tilde{q}^{(N)}$ in Table 2.2. In this case, because of the fact that isospin symmetry is exactly preserved for the $\Delta q^{(N)}$ coefficients, both quark-level and nucleon-level isospin preservation coincide exactly at $\theta = \pi/4$. Indeed, at this point we find $g_{\chi p} = g_{\chi n} \approx 0.303 \pm 0.12$, while the maximum value taken by these couplings for any isospin-violating value of θ is $|g_{\chi p}| \approx 0.865 \pm 0.15$ at $\theta \approx 2.714$ and $g_{\chi n} \approx 0.812 \pm 0.15$ at $\theta \approx 1.974$. Thus, for the axial-vector case, we see that isospin violation is capable of increasing the proton and neutron couplings only by mere factors of 2.85 and 2.68 respectively.

We also note, of course, that the overall *scale* of the axial-vector couplings is significantly smaller than that for the pseudoscalar couplings. While it is perhaps inappropriate to compare the magnitudes of these different couplings against each other (because they correspond to different operators with gamma-matrix bilinears exhibiting entirely different tensorial properties), at a purely algebraic level this difference can once again be attributed to the larger values of the $\Delta\tilde{q}^{(N)}$ coefficients that enter the calculation of the pseudoscalar proton and neutron couplings as compared with the values of the $\Delta q^{(N)}$ coefficients that enter the calculation of their axial-vector counterparts.

In Fig. 2.1, we have plotted the pseudoscalar proton and neutron couplings $g_{\chi p}$ and $g_{\chi n}$, along with their corresponding uncertainties, as functions of θ for all three of our coupling scenarios. For comparison purposes, we have also plotted the corresponding axial-vector couplings as functions of the same variable θ. Moreover, in each case we have normalized the proton and neutron couplings to the maximum value that the proton coupling ever attains as a function of θ.

Many features of these plots are worthy of note. Focusing first on the pseudoscalar couplings, we have already remarked that a significant degree of cancellation occurs within Scenario I when isospin is conserved at the nucleon level: both the proton and neutron pseudoscalar couplings, along with their associated uncertainties, become extremely small as a result of a near-perfect cancellation between their individual up-quark and down-quark contributions. As remarked earlier, this is then a situation in which our dark matter cou-

ples to quarks, but not to nucleons! What is now apparent from Fig. 2.1, however, is that this cancellation is a relatively sharp one, and that any movement away from this isospin-conserving value of θ in either direction results in a significant enhancement of these pseudoscalar nucleon couplings. As indicated above, this results in an $\mathcal{O}(10^3)$ enhancement in the pseudoscalar couplings for isospin-violating scenarios relative to the naïve isospin-conserving case, and thus to an $\mathcal{O}(10^6)$ enhancement in the cross-section for the scattering of χ off atomic nuclei. Thus, we see that even a relatively small amount of isospin violation can have a dramatic effect on direct-detection rates! The above behavior occurs for Scenario I. However, we now see from Fig. 2.1 that similar behavior also occurs for Scenario III, albeit at a somewhat shifted value of θ. This feature is also easy to understand. In Scenario I, the cancellation that occurs at θ^* truly reflects an approximate isospin symmetry. Indeed, while the term in Eq. (2.20) proportional to $\Delta\tilde{G}^{(N)}$ is manifestly isospin-violating, this contribution is suppressed by several orders of magnitude compared to the contributions from the light quarks in this scenario. Moreover, since the c_q are independent of the quark masses in Scenario I and since the $\Delta\tilde{q}^{(N)}$ are *approximately* isospin-conserving (particularly for the two lightest quarks), this cancellation occurs for a value of θ^* very close to $\theta \approx \pi/4$. Of course, in Scenario III, the $\Delta\tilde{G}^{(N)}$ contribution to the couplings vanishes outright because the dark-matter particle does not couple to the heavy quarks. However, the above cancellation now occurs at the value $\theta^* = \tan^{-1}(m_u/m_d) \approx 0.45$ rather than at $\theta^* \approx \pi/4$, for within Scenario III it is only at this shifted angle that $c_u = c_d$. Furthermore, within Scenario III, we see that the uncertainties are no smaller at θ^* than they are at any other angle — another distinction relative to Scenario I.

Finally, we observe that the pseudoscalar couplings shown for Scenario II differ quite significantly from those shown for Scenario III, both in terms of the locations of the nucleon-level isospin-preserving points as well as the overall magnitudes of the associated uncertainties. These differences ultimately reflect the contributions from the second- and third-generation quarks. One notable feature in Scenario II, for example, is the fact that the sort of cancellation which occurs for Scenarios I and III does not occur for Scenario II. The

reason for this is also easy to understand. In Scenario II, we have $c_q \propto m_q$ for all quark species. For such a coupling structure, it turns out that the magnitudes of the two terms on the right side of Eq. (2.20) are roughly commensurate. Thus, even if θ were set at a value for which the light-quark contributions roughly cancelled, the heavy-quark contributions would still be significant. Indeed, for this scenario, we find that nucleon-level isospin preservation arises at $\theta^* \approx 3.12$ — a value much closer to π than to $\pi/4$ — but the proton and neutron couplings at this point are clearly non-zero.

In Fig. 2.1 we have also illustrated what occurs for the corresponding *axial-vector* couplings in each scenario. For example, as already discussed above, we see that the isospin-preserving points no longer correspond to vanishing proton and neutron couplings — even for Scenarios I and III. Thus isospin violation will no longer produce as dramatic an enhancement for the axial-vector proton and neutron couplings as it does for the corresponding pseudoscalar couplings, even in these scenarios. Moreover, we observe that unlike the situation for the pseudoscalar couplings, there are no values of θ in Scenarios I or III for which both $g_{\chi p}$ and $g_{\chi n}$ vanish simultaneously. Thus, for axial-vector couplings, dark-matter couplings to quarks always imply a dark-matter coupling to at least one nucleon. Furthermore, we see that the uncertainties are so large for the axial-vector neutron coupling in Scenario II that the value of this coupling is consistent with zero for almost all values of θ. Finally, although it is not visible from the plots in Fig. 2.1, we again stress that the overall magnitude of the axial-vector couplings is a factor of $\mathcal{O}(10^2 - 10^3)$ smaller than the magnitude of the pseudoscalar couplings. This is perhaps the most important difference of all.

Despite the rather compelling nature of these differences, it is important to bear in mind that the pseudoscalar and axial-vector couplings correspond to entirely different operators. Thus, a direct comparison between these couplings is fraught with a number of theoretical subtleties. For example, Scenarios II and III are rather unnatural within an axial-vector framework, and it is difficult to imagine a high-scale model which might yield such an axial-vector effective operator with the quark-level couplings of Scenarios II or III at lower energies. This is completely different from what happens within the pseudoscalar

framework, where the coupling structures of Scenarios II and III are particularly well motivated. Nevertheless, we have undertaken such a direct coupling-to-coupling comparison in order to expose the primary numerical differences that emerge when the axial-vector $\Delta q^{(N)}$ coefficients of Table 2.1 are replaced with the pseudoscalar $\Delta\tilde{q}^{(N)}$ coefficients of Table 2.2. Indeed, from a purely bottom-up perspective, the coupling structures of all three scenarios can be taken to represent interesting benchmarks which are introduced purely for the purpose of studying varying resulting phenomenologies in a model-independent framework. We have therefore chosen to study the resulting couplings free of any theoretical prejudice stemming from considerations of high-scale physics.

Of course, what ultimately matters in each case are not the couplings themselves, but rather the implications of these couplings for the reach of actual direct-detection experiments. For example, we have seen that even a small amount of isospin violation can dramatically enhance our pseudoscalar couplings, but it remains to be seen whether this effect is large enough to compensate for the velocity suppression which is also associated with pseudoscalar interactions, and thereby render such interactions potentially relevant for detection at the next generation of spin-dependent dark-matter direct-detection experiments. This is therefore the topic to which we now turn.

2.2 CP or not CP, that is the question: An interlude on the choice of Lagrangian operators

In this work, our analysis has focused on those interactions between dark matter and Standard-Model matter which take the form of effective four-Fermi contact interactions whose operators exhibit the double-bilinear form in Eq. (2.1). Thus far, our interest has focused on the unique physics that emerges from assuming a pseudoscalar structure for the quark bilinear in Eq. (2.1), and indeed all of our results thus far have relied on this choice. However, we have yet to select a tensor structure for the corresponding dark-matter bilinear,

and Lorentz invariance dictates that there are only two possible choices open to us:

$$\begin{aligned} \mathcal{O}_{\chi q}^{(\mathrm{SP})} &\equiv \frac{c_q}{\Lambda^2}\left(\overline{\chi}\chi\right)\left(\overline{q}i\gamma^5 q\right) \\ \mathcal{O}_{\chi q}^{(\mathrm{PP})} &\equiv \frac{c_q}{\Lambda^2}\left(\overline{\chi}i\gamma^5\chi\right)\left(\overline{q}i\gamma^5 q\right) . \end{aligned} \tag{2.23}$$

The first of these operators breaks CP symmetry, while the second preserves it. Unfortunately, we can proceed no further in our discussion of actual direct-detection experimental prospects without making a specific choice between these two operators. The CP-violating operator $\mathcal{O}_{\chi q}^{(\mathrm{SP})}$ is often neglected in direct-detection studies, even in comparison with $\mathcal{O}_{\chi q}^{(\mathrm{PP})}$. One reason for this is that $\mathcal{O}_{\chi q}^{(\mathrm{PP})}$ is CP-invariant and can therefore be generated at a non-trivial level in many top-down theoretical constructions which yield a stable dark-matter candidate, such as the constrained minimal supersymmetric model (CMSSM) in which there is no additional source of CP violation. However, in a bottom-up effective-theory approach such as the one we adopt here, the aim is to examine and constrain the properties of all possible interactions which could arise between the dark-matter candidate and the particles of the SM in as model-independent a framework as possible, without theoretical prejudice. Indeed, while the operator $\mathcal{O}_{\chi q}^{(\mathrm{PP})}$ is typically assumed to be irrelevant for direct detection, it is instructive to revisit why this is the case — and also why this is *not* the case for $\mathcal{O}_{\chi q}^{(\mathrm{SP})}$, despite the fact that the structure of the quark bilinear is the same in both cases.

Let us first consider the situation in which χ couples to SM particles primarily via $\mathcal{O}_{\chi q}^{(\mathrm{PP})}$. We assume for the purposes of this discussion that this operator provides the dominant contribution both to the cross-section for nuclear scattering events at direct-detection experiments and to the annihilation rate of χ and $\overline{\chi}$ in the early universe. For purposes of illustration, we also restrict our attention to the case in which χ couples to only one quark flavor; thus only one of the c_q is non-vanishing. We have already seen for $\mathcal{O}_{\chi q}^{(\mathrm{PP})}$ that both the dark-matter bilinear and the quark-bilinear give rise to a velocity suppression in the dark-matter/nucleon cross-section for direct detection. Thus, for $\mathcal{O}_{\chi q}^{(\mathrm{PP})}$, the resulting

(spin-dependent) cross-section can be expected to scale like

$$\text{PP}: \qquad \sigma_{\text{SD}}^{(\chi N)} \;\sim\; \frac{c_q^2 \left[\Delta\tilde{q}^{(N)}\right]^2 \mu_{\chi N}^6 v^4}{m_\chi^2 m_N^2 \Lambda^4} \;, \tag{2.24}$$

where $\mu_{\chi N} \equiv m_\chi m_N/(m_\chi + m_N)$ denotes the reduced mass of the χ/nucleon system.

There are clearly many unknown parameters in Eq. (2.24), making it difficult to provide an actual numerical estimate of this cross-section. However, we may appeal to a somewhat orthogonal constraint which applies to any thermal dark-matter candidate: that through which the annihilation rate of χ and $\overline{\chi}$ sets an overall dark-matter abundance in the early universe. For $\mathcal{O}_{\chi q}^{(\text{PP})}$, the annihilation of χ and $\overline{\chi}$ in the early universe has no chirality suppression since the initial state is CP-odd, with quantum numbers $S = 0$, $L = 0$, and $J = 0$ [36]. In an s-wave annihilation scenario of this sort, the thermal annihilation cross-section $\langle\sigma|v|\rangle$ scales like

$$\text{PP}: \qquad \langle\sigma|v|\rangle \;\sim\; \frac{c_q^2 m_\chi^2}{\Lambda^4} \tag{2.25}$$

at around the time of freeze-out. Moreover, in order for the relic-abundance contribution from freeze-out to agree with observation (*i.e.*, $\Omega_\chi \approx \Omega_{\text{DM}}$), this cross-section must be roughly $\langle\sigma|v|\rangle \sim 1$ pb at such times.

Given this constraint, we can substitute back into Eq. (2.24) in order to find that

$$\text{PP}: \qquad \sigma_{\text{SD}}^{(\chi N)} \;\sim\; (1\text{ pb}) \times \frac{\left[\Delta\tilde{q}^{(N)}\right]^2 \mu_{\chi N}^6 v^4}{m_\chi^4 m_N^2} \;. \tag{2.26}$$

Since $v^4 \sim \mathcal{O}(10^{-12})$, we see that extremely large values of $\Delta\tilde{q}^{(N)}$ would be required to overcome this velocity suppression and yield a χ/nucleon cross-section of sufficient magnitude to be probed at any foreseeable direct-detection experiment, even for low-mass dark matter. Indeed, since both $\langle\sigma|v|\rangle$ and $\sigma_{\text{SD}}^{(\chi N)}$ depend on Λ in the same manner for a thermal relic, this unhappy consequence exists regardless of the scale Λ at which Ω_χ is generated via thermal freeze-out for a dark-matter particle with this coupling structure. Unfortunately, we have already seen that our pseudoscalar $\Delta\tilde{q}^{(N)}$ coefficients, although significantly en-

hanced relative to their axial-vector counterparts, are not large enough to overcome this degree of velocity suppression. Thus we do not expect the operator $\mathcal{O}_{\chi q}^{(\mathrm{PP})}$ to have much relevance for direct-detection experiments.

Let us now turn to the situation in which χ primarily couples to SM particles through the operator $\mathcal{O}_{\chi q}^{(\mathrm{SP})}$. In sharp contrast to the $\mathcal{O}_{\chi q}^{(\mathrm{PP})}$ case discussed above, in this case only the quark bilinear gives rise to a velocity suppression in the cross-section for non-relativistic χ/nucleon scattering. This cross-section therefore scales like

$$\mathrm{SP}: \qquad \sigma_{\mathrm{SD}}^{(\chi N)} \;\sim\; \frac{c_q^2 \left[\Delta\tilde{q}^{(N)}\right]^2 \mu_{\chi N}^4 v^2}{m_N^2 \Lambda^4} \;. \tag{2.27}$$

Moreover, in this case we see that dark-matter annihilation in the early universe is p-wave suppressed, since the initial state is CP-even, with quantum numbers $S = 1$, $L = 1$, and $J = 0$. The annihilation cross-section in this case scales like

$$\mathrm{SP}: \qquad \langle \sigma |v| \rangle \;\sim\; v_{\chi,\mathrm{fr}}^2 \frac{c_q^2 m_\chi^2}{\Lambda^4} \;, \tag{2.28}$$

where $v_{\chi,\mathrm{fr}}$ denotes the average speed of χ and $\overline{\chi}$ at freeze-out. Typically, $v_{\chi,\mathrm{fr}}^2 \sim 0.1$. Imposing, as before, the condition $\langle \sigma |v| \rangle \sim 1$ pb in order to ensure that $\Omega_\chi \approx \Omega_{\mathrm{DM}}$, we find that

$$\mathrm{SP}: \qquad \sigma_{\mathrm{SD}}^{(\chi N)} \;\sim\; (1 \text{ pb}) \times \frac{10 \left[\Delta\tilde{q}^{(N)}\right]^2 \mu_{\chi N}^4 v^2}{m_\chi^2 m_N^2} \;. \tag{2.29}$$

Since the velocity suppression $v^2 \sim \mathcal{O}(10^{-6})$ obtained in this case is far less severe than that obtained in Eq. (2.26), we see that only moderately large values for the $\Delta\tilde{q}^{(N)}$ coefficients are required in order to compensate for this velocity suppression and render the operator $\mathcal{O}_{\chi q}^{(\mathrm{SP})}$ relevant for direct detection. Moreover, as we have seen in Sect. 2.1, these coefficients are indeed enhanced by the required amount.

We thus conclude that $\mathcal{O}_{\chi q}^{(\mathrm{SP})}$, rather than $\mathcal{O}_{\chi q}^{(\mathrm{PP})}$, has greater prospects for being relevant to future direct-detection experiments. As a result, we shall concentrate on $\mathcal{O}_{\chi q}^{(\mathrm{SP})}$ in the remainder of this chapter.

2.3 Phenomenological consequences: Direct detection and related benchmarks

We now turn to investigate the direct-detection prospects for a dark-matter candidate in each of the three benchmark coupling scenarios defined in Sect. 2.1.3. In particular, we wish to determine the bounds imposed by existing direct-detection data on the corresponding suppression scale $M_{\rm I}$, $M_{\rm II}$, or $M_{\rm III}$ in each of these scenarios as a function of the dark-matter mass m_χ and the coupling angle θ, and to assess the extent to which the next generation of direct-detection experiments will be able to probe the remaining parameter space in each scenario.

In interpreting the results of such a direct-detection analysis, it is also useful to examine the relationship between the region of parameter space accessible by direct-detection experiments in each of these coupling scenarios and regions of parameter space which are relevant for other aspects of dark-matter phenomenology. For example, thermal freeze-out offers a natural mechanism for generating a relic abundance of the observed magnitude for a massive dark-matter particle which can annihilate to SM particles. It is therefore interesting to examine whether successful thermal freeze-out can be realized within the region of parameter space accessible to the next generation of direct-detection experiments for a dark-matter particle which annihilates primarily via $\mathcal{O}_{\chi q}^{(\rm SP)}$. In addition, new-physics searches in a variety of channels at the LHC constrain the parameter space of operators which couple the dark and visible sectors. It is therefore also interesting to examine the interplay between these constraints and those from direct-detection data.

The plan of this section is as follows. We begin by briefly reviewing the physics of direct detection and assessing the extent to which the next generation of direct-detection experiments will be capable of probing the parameter space of each of our benchmark coupling scenarios. We then identify the regions of that parameter space which yield a thermal dark-matter relic abundance of the correct order, and discuss how LHC data serve to constrain that parameter space. As we shall see, the magnitudes of the pseudoscalar

$\Delta\tilde{q}^{(N)}$ coefficients have a profound effect on the direct-detection phenomenology of a dark-matter particle which interacts with the visible sector primarily via the $\mathcal{O}_{\chi q}^{(\mathrm{SP})}$ operators.

2.3.1 Direct detection

The principal physical quantity probed by direct-detection experiments is the total event rate R for dark-matter scattering off the nuclei in the detector target. For a generic dark-matter model, the expectation value for R at any particular such experiment is obtained by integrating the differential rate dR/dE_R over the range of recoil energies E_R probed by that experiment, convolved with the appropriate detector-efficiency function $\mathcal{E}(E_R)$. This differential event rate (for reviews, see, *e.g.*, Refs. [14, 15]) is given by the general expression

$$\frac{dR}{dE_R} \;=\; \frac{N_T \rho_\chi^{\mathrm{loc}}}{m_\chi} \int_{v>v_{\mathrm{min}}}^{\infty} v f(\vec{v}) \left(\frac{d\sigma_{\chi T}}{dE_R} \right) d^3 v \;, \tag{2.30}$$

where N_T is the number of nuclei in the detector target, where ρ_χ^{loc} is the local density of χ within the galactic halo, where $f(\vec{v})$ is the velocity distribution of dark-matter particles in the reference frame of the detector, where $v \equiv |\vec{v}|$, and where $d\sigma_{\chi T}/dE_R$ is the differential scattering cross-section. The lower limit v_{min} on the integral over halo velocities corresponds to the kinematic threshold for non-relativistic scattering of a dark-matter particle off one of the target nuclei.

While substantial uncertainties exist concerning many of the aforementioned quantities which characterize the properties of the dark-matter halo, our focus here is on the pseudoscalar nucleon coefficients $\Delta\tilde{q}^{(N)}$ and their implications for direct detection. We therefore adopt a set of standard benchmark assumptions about the dark-matter halo. In particular, we take $\rho_\chi^{\mathrm{loc}} = 0.3\ \mathrm{GeV\,cm^{-3}}$; we take $f(\vec{v})$ to be Maxwellian, but truncated above the galactic escape velocity $v_{\mathrm{esc}} \approx 550$ km/s in the halo frame; and we take $v_e = 232$ km/s as the speed of the Earth with respect to the dark-matter halo. Moreover, we focus on the case in which χ/nucleus scattering is purely elastic, for which $v_{\mathrm{min}} = \sqrt{E_R m_T / 2\mu_{\chi T}^2}$, where m_T denotes the mass of the target nucleus and where $\mu_{\chi T}$ is the reduced mass of the χ/nucleus system.

The differential cross-section for χ/nucleus scattering is given by the general expression

$$\frac{d\sigma_{\chi T}}{dE_R} \;=\; \frac{m_T}{2\pi v^2}\left\langle |\mathcal{M}_{\chi T}|^2 \right\rangle \;, \tag{2.31}$$

where $\langle|\mathcal{M}_{\chi T}|^2\rangle$ is the corresponding squared S-matrix element, averaged over initial spin states and summed over final spin states. For the scalar-pseudoscalar interaction we are considering here, we recall Eq. (2.7) to find that this matrix element in the non-relativistic limit takes the form

$$\begin{aligned}\mathcal{M}_{\chi T} \;&=\; \sum_{N=n,p}\frac{g_{\chi N}}{\Lambda^2}\langle\chi_f|\overline{\chi}\chi|\chi_i\rangle\langle T_f|\overline{N}\gamma^5 N|T_i\rangle \\ &\approx\; \frac{4m_\chi m_T}{\Lambda^2}(\xi_\chi^{s'})^\dagger\xi_\chi^s\sum_{N=n,p}\frac{g_{\chi N}}{m_N}\langle T_f|\vec{q}\cdot\vec{S}_N|T_i\rangle \;,\end{aligned} \tag{2.32}$$

where $\langle T_f|\vec{S}_N|T_i\rangle$ denotes the matrix element for the nucleon-spin operator within the target nucleus and where $\vec{q}$ is the momentum transferred to the nucleus. Note that the m_T/m_N factor in Eq. (2.32) arises due the difference in normalization between the constituent nucleons and the bound-state nucleus, where we have retained the relativistic normalization in both cases. Proceeding by analogy with the axial-vector case [49], we invoke the Wigner-Eckart theorem in order to make the replacement

$$\langle T_f|\vec{S}_N|T_i\rangle \;\rightarrow\; \frac{\langle S_N\rangle}{J_T}\langle T_f|\vec{J}_T|T_i\rangle \tag{2.33}$$

in Eq. (2.32), where $\langle S_N\rangle/J_T = \langle T_f|S_N|T_i\rangle/J_T$ again represents the fraction of the total nuclear spin carried by the nucleon N. In the approximation that $m_p \approx m_n$, this yields

$$\begin{aligned}\mathcal{M}_{\chi T} \;&=\; \frac{4m_\chi m_T}{J_T\Lambda^2 m_N}\Big(g_{\chi p}\langle S_p\rangle + g_{\chi n}\langle S_n\rangle\Big)(\xi_\chi^{s'})^\dagger\xi_\chi^s \\ &\qquad\times\;\langle T_f|\vec{q}\cdot\vec{J}_T|T_i\rangle \;.\end{aligned} \tag{2.34}$$

The spin-averaged squared matrix element is therefore

$$\begin{aligned}\left\langle|\mathcal{M}_{\chi T}|^2\right\rangle &= \frac{16m_\chi^2 m_T^2}{J_T^2(2J_T+1)m_N^2\Lambda^4}\left(g_{\chi p}\langle S_p\rangle + g_{\chi n}\langle S_n\rangle\right)^2 \\ &\quad\times \sum_{T_i,T_f}\langle T_f|\vec{q}\cdot\vec{J}_T|T_i\rangle\langle T_i|\vec{q}\cdot\vec{J}_T|T_f\rangle \\ &= \frac{16m_\chi^2 m_T^2|\vec{q}|^2}{3m_N^2}\frac{J_T+1}{J_T}\left(\frac{g_{\chi p}}{\Lambda^2}\langle S_p\rangle + \frac{g_{\chi n}}{\Lambda^2}\langle S_n\rangle\right)^2 . \end{aligned} \tag{2.35}$$

Substituting this result into Eq. (2.31) and dividing by $16m_\chi^2 m_T^2$ in order to account for the difference between relativistic and non-relativistic normalization conventions for the χ and nucleus states, we arrive at our final expression for the differential cross-section for χ/nucleus scattering:

$$\begin{aligned}\frac{\partial\sigma_{\chi T}^{(\mathrm{SP})}}{\partial E_R} &= \frac{m_T^2 E_R}{3\pi v^2 m_N^2}\frac{J_T+1}{J_T} \\ &\quad\times\left(\frac{g_{\chi p}}{\Lambda^2}\langle S_p\rangle + \frac{g_{\chi n}}{\Lambda^2}\langle S_n\rangle\right)^2 \widetilde{F}^2(E_R)\ , \end{aligned} \tag{2.36}$$

where $\widetilde{F}^2(E_R)$ is a nuclear form factor. Note that we have explicitly distinguished this form factor from the usual form factor $F^2(E_R) = S(E_R)/S(0)$ associated with spin-dependent scattering via an axial-vector interaction. Indeed, in the axial-vector case, the scattering cross-section depends on the projection of $\vec{S}_N$ along the direction of the spin vector $\vec{S}_\chi$ of the dark-matter particle. By contrast, in the scalar-pseudoscalar case, the corresponding cross-section depends on the projection of $\vec{S}_N$ along the direction of the momentum transfer [50].

A wealth of data from direct-detection experiments already significantly constrains the set of possible interactions between dark-matter particles and atomic nuclei, and several additional experiments are poised to probe even more deeply over the coming decade into the parameter space of allowed couplings between the dark and visible sectors. For each of our three benchmark coupling scenarios for scalar-pseudoscalar interactions, the relevant parameter space comprises m_χ, θ, and the corresponding suppression scale M_{I}, M_{II}, or M_{III}. The first of these parameters enters the expected event rate for a given detector

in a complicated way through the scattering kinematics, while the second and third enter through the ratios $g_{\chi p}/\Lambda^2$ and $g_{\chi n}/\Lambda^2$ in Eq. (2.36), as discussed in Sect. 2.1.3.

Since the χ/nucleus interactions which follow from $\mathcal{O}_{\chi q}^{(\mathrm{SP})}$ involve the nuclear spin $\vec{S}_N$, the relevant constraints on these parameters are those which pertain to spin-dependent scattering. Several direct-detection experiments already provide comparable, stringent limits on spin-dependent scattering [51–53]. Moreover, the next generation of these experiments, including COUPP-60 and PICO-250L, are projected to significantly extend the reach of these experiments in the near future [54]. In this chapter, our primary aim is to investigate the sensitivity of these latter experiments to scalar-pseudoscalar interactions between dark-matter particles and atomic nuclei. We therefore focus on the results from COUPP-4, for which the experimental setup and analysis parallel those for COUPP-60 and PICO-250L, when discussing existing limits on spin-dependent scattering. These limits are typically expressed as bounds on the spin-dependent dark-matter/proton scattering cross-section $\sigma_{\chi p}^{(\mathrm{AA})}$ for a dark-matter particle whose interactions with nuclei are primarily due to the axial-vector operators $\mathcal{O}_{\chi q}^{(\mathrm{AA})}$. This cross-section may be parametrized as

$$\sigma_{\chi p}^{(\mathrm{AA})} \;=\; \frac{3 a_{\chi p}^2 \mu_{\chi p}^2}{\pi \Lambda^4} \;, \tag{2.37}$$

where μ_p is the reduced mass of the χ/proton system and where

$$a_{\chi N} \;\equiv\; \sum_{q=u,d,s} c_q^{(\mathrm{AA})} \Delta q^{(N)} \tag{2.38}$$

are the axial-vector analogues of the χ/nucleon couplings $g_{\chi N}$ given in Eq. (2.20). Note that because we take χ to be a Dirac fermion, this expression differs by a factor of 4 from the standard expression for a Majorana fermion. The differential cross-section for χ/nucleus

scattering for such an interaction, expressed in terms of $\sigma_{\chi p}^{(\mathrm{AA})}$, is given by

$$\frac{\partial \sigma_{\chi T}^{(\mathrm{AA})}}{\partial E_R} = \frac{2\sigma_{\chi p}^{(\mathrm{AA})} m_T}{3\mu_p^2 v^2} \frac{J_T + 1}{J_T} \times \left(\langle S_p \rangle + \frac{a_{\chi n}}{a_{\chi p}} \langle S_n \rangle \right)^2 F^2(E_R) \ . \tag{2.39}$$

It is therefore straightforward to convert the limits on $\sigma_{\chi p}^{(\mathrm{AA})}$ into limits on the expected event rate for dark-matter scattering off nuclei within the detector volume. The latter limits are model-independent and applicable to any interaction between dark-matter and atomic nuclei, including the scalar-pseudoscalar interactions which are the focus of this current work.

The bounds implied by COUPP-4 data on the parameter space of each of our three coupling scenarios, along with the projected reach into that parameter space for both COUPP-60 and PICO-250L, will be discussed in the next section. These bounds and sensitivities will be expressed as contours in (m_χ, M_*) space for each scenario and for several benchmark values of θ, where M_* denotes the corresponding suppression scale M_{I}, M_{II}, or M_{III}. In evaluating these contours, we will make use of the DMFormFactor package [50]. We will also include bands indicating the uncertainties in these contours which arise as a result of the uncertainties in the nucleon couplings $g_{\chi N}$ discussed in Sect. 2.1.

2.3.2 Relic abundance

Thermal freeze-out is a natural mechanism through which a sizable relic abundance can be generated for a massive particle with suppressed couplings to SM states. It is therefore useful to identify the regions of parameter space within which the relic abundance of a dark-matter particle which annihilates via the $\mathcal{O}_{\chi q}^{(\mathrm{SP})}$ operator reproduces the observed dark-matter relic abundance $\Omega_{\mathrm{DM}} \approx 0.26$ [8]. In this section, we briefly summarize the relic-abundance calculation for an interaction of this sort. Note that we take χ to be a Dirac fermion throughout and make use of the general formalism in Ref. [55] for multi-particle freeze-out dynamics in order to evaluate the total relic abundance of χ and its conjugate $\overline{\chi}$, which in

this case represent distinct degrees of freedom.

The evolution of the total number density $Y \equiv Y_\chi + Y_{\bar{\chi}}$ of particles which contribute to the dark-matter abundance at late times due to thermal freeze-out in this scenario can be described by the single differential equation

$$\frac{dY}{dt} \;=\; -\,s\,\langle\sigma|v|\rangle\left[Y^2 - (Y^{\rm eq})^2\right]\,, \tag{2.40}$$

where $Y^{\rm eq}$ is the value which Y would have were χ and $\overline{\chi}$ in thermal equilibrium at time t; where $s = 2\pi^2 g_{*s}(T)T^3/45$ is the entropy density of the universe, expressed here in terms of the temperature T of the thermal bath at time t and the number of effectively massless degrees of freedom $g_*(T)$ at that temperature T; and where $\langle\sigma|v|\rangle$ is the thermally-averaged total cross-section for dark-matter annihilation. The total present-day dark-matter-abundance contribution from χ and $\overline{\chi}$ due to thermal freeze-out is related to the present-day value $Y_{\rm now}$ of Y by

$$\Omega_\chi \;\equiv\; \frac{\rho_\chi}{\rho_{\rm crit}} \;=\; \frac{s_{\rm now}\,m_\chi\,Y_{\rm now}}{\rho_{\rm crit}}\,, \tag{2.41}$$

where $s_{\rm now} \approx 2.22 \times 10^{-38}$ GeV^3 and $\rho_{\rm crit} \approx 4.18 \times 10^{-47}$ GeV^4 are the present-day entropy density and present-day critical energy density of the universe, respectively.

In the case in which χ and $\overline{\chi}$ annihilate primarily to SM quarks via $\mathcal{O}_{\chi q}^{\rm (SP)}$, we find that the thermally-averaged annihilation cross-section for processes of the form $\overline{\chi}\chi \to \overline{q}q$ is given by

$$\langle\sigma|v|\rangle \;=\; \frac{3x}{256\pi m_\chi^5 K_2(x)}\sum_q \frac{c_q^2}{\Lambda^4}\mathcal{I}_q(x)\,, \tag{2.42}$$

where we have defined

$$\mathcal{I}_q(x) \;\equiv\; \int_{4m_\chi^2}^{\infty} ds\sqrt{s(s-4m_\chi^2)^3(s-4m_q^2)}\,K_1\left(\frac{x\sqrt{s}}{m_\chi}\right)\,. \tag{2.43}$$

In these expressions, $x \equiv m_\chi/T$, $s = (p_\chi + p_{\bar{\chi}})^2$ is the usual Mandelstam variable (*not* the entropy density of the universe, and *not* the strange quark either), and $K_1(x)$ and $K_2(x)$

denote the modified Bessel functions of the second kind of degree one and two, respectively.

In the next section we will display contours corresponding to the condition $\Omega_\chi = \Omega_{\rm DM}$, as well as contours of $\langle\sigma|v|\rangle$. In accord with expectation, we will find that a relic abundance of the correct order is obtained for $\langle\sigma|v|\rangle \approx 1$ pb. In interpreting these results, it should be noted that Ω_χ depends on m_χ in the usual manner, whereas this quantity depends on θ and the corresponding suppression scale $M_{\rm I}$, $M_{\rm II}$, or $M_{\rm III}$ in each of our coupling scenarios through the ratio c_q^2/Λ^4 in Eq. (2.42). Generally speaking, $\Omega_\chi \propto \langle\sigma|v|\rangle^{-1}$ for thermal freeze-out, and therefore a higher suppression scale corresponds to a smaller $\langle\sigma|v|\rangle$ and a larger relic abundance.

2.3.3 Collider constraints

Colliders offer a complementary way of probing the couplings between dark-sector and visible-sector fields. In particular, the effective operators given in Eq. (2.1) generically contribute to the event rate for processes of the form $pp \to X + \not{E}_T$ at the LHC — *i.e.*, so-called "mono-anything" processes — where X denotes a single SM particle such as a photon (the monophoton channel), an electroweak gauge boson, or even a "particle" such as a hadronic jet (the monojet channel). While the results depend on the particular operator and the relative values of the coupling coefficients (see, *e.g.*, Ref. [56–61]), the most stringent constraints on such operators are typically those derived from limits on monojet production at ATLAS [62, 63] and CMS [64, 65] and from limits on the production of a hadronically decaying $W^\pm$ or Z boson at ATLAS [66, 67]. We will henceforth focus on these channels, but we also note that a combined analysis [68, 69] involving all relevant $pp \to X + \not{E}_T$ processes would lead to a slight enhancement of the bounds from these two leading channels individually. Moreover, we also note that searches in the mono-b and $t\bar{t} + \not{E}_T$ channels can potentially supersede these limits for models in which the couplings between the dark matter and the third-generation quarks are enhanced [48], as is the case in our Scenario II.

We now proceed to derive a set of rough limits on the corresponding suppression scale $M_{\rm I}$, $M_{\rm II}$, or $M_{\rm III}$ associated with each of our benchmark coupling scenarios. We derive these

limits under the assumption that a contact-operator description of the interactions between χ and the SM quarks remains valid up to the center-of-mass-energy scale $\sqrt{s} \approx 8$ TeV of the LHC. We then return to discuss how these results are altered in cases in which the contact-operator description is valid at scales relevant for direct detection, but breaks down at scales well below $\sqrt{s}$.

We begin by noting that the monojet [65] and mono-W/Z [66, 67] analyses which correspond to the most stringent current limits on dark-matter production at the LHC are effectively counting experiments which serve to constrain the total cross-section for the corresponding production processes. A lower limit $M_* > M_{\rm min}$ on the heavy mass scale M_* defined for the operator D3 in the standard operator-classification scheme of Ref. [70] [which corresponds to our scalar-pseudoscalar operator $\mathcal{O}_{\chi q}^{\rm (SP)}$] from either of these analyses corresponds to a limit $M_{\rm II} > M_{\rm min}/2^{1/6}$ in our Scenario II with $\theta = \pi/4$. We also note that the production cross-section for each process scales like $\sigma_{\rm I}(m_\chi, M_{\rm I}, \theta) \propto M_{\rm I}^{-4}$ in Scenario I, whereas it scales like $\sigma_{\rm II,III}(m_\chi, M_{\rm II,III}, \theta) \propto M_{\rm II,III}^{-6}$ in Scenarios II and III. It therefore follows that bounds on $M_{\rm I}$ can be derived from the bounds on $M_{\rm min}$ quoted in Refs. [65] and [66, 67] and the ratio of the corresponding production cross-sections for the same m_χ and the same fiducial value of $M_{\rm I}$. In this analysis, we choose 1 TeV as our fiducial mass scale. We therefore have

$$\frac{M_{\rm I}}{\rm GeV} \gtrsim \left[\frac{\sigma_{\rm I}(m_\chi, 1\,{\rm TeV}, \theta)}{2\,\sigma_{\rm II}(m_\chi, 1\,{\rm TeV}, \pi/4)}\right]^{1/4} \left(\frac{M_{\rm min}}{10\,{\rm GeV}}\right)^{3/2} . \tag{2.44}$$

Likewise, lower limits on $M_{\rm II}$ and $M_{\rm III}$ may be derived using the relation

$$M_{\rm II,III} \gtrsim \left[\frac{\sigma_{\rm II,III}(m_\chi, 1\,{\rm TeV}, \theta)}{2\,\sigma_{\rm II}(m_\chi, 1\,{\rm TeV}, \pi/4)}\right]^{1/6} M_{\rm min} . \tag{2.45}$$

Constraint contours corresponding to the limits on contact-operator interactions from these most recent monojet and mono-W/Z analyses will be discussed in the next section for each of our three coupling scenarios. The relevant cross-sections in each case are evaluated at parton level using the MadGraph/MadEvent package [71] (with the CTEQ6L1 PDF

set [72]) including the contribution from processes involving b quarks in the initial state. The event-selection criteria we employ in estimating these limits are modeled on those described in Ref. [65] for the mono-jet channel and Ref. [66, 67] for the mono-W/Z channel, and we have verified that minor alterations in these cuts do not have significant effects on our results.

As mentioned above, it is important to note that constraints derived in this manner are valid only in the regime in which interactions between dark-matter particles and SM quarks can legitimately be modeled as contact operators at energies comparable to $\sqrt{s}$. In other words, they are valid for processes in which the mass m_ϕ of the particle ϕ which mediates the interaction is much larger than the momentum transfer to the dark-matter system. By contrast, for lower mediator masses $m_\phi \lesssim 1$ TeV, these limits are no longer applicable — even for $m_\phi > m_\chi$. Constraints on interactions between dark-matter particles and SM quarks can still be derived from LHC data for theories in which $m_\phi \lesssim 1$ TeV; however, such constraints are highly model-dependent, sensitive to the full structure of the dark sector, and frequently weaker than the naïve limits one would obtain for these same channels in the contact-operator regime [73, 74].

On the other hand, while the contact-operator approximation becomes unreliable from the perspective of collider phenomenology for $m_\phi \lesssim 1$ TeV, it remains valid for direct-detection phenomenology down to far lower values of m_ϕ. Indeed, interactions involving light mediators can still be reliably modeled as contact interactions at energies relevant for direct detection, provided that $m_\phi \gtrsim 1$ GeV. Moreover, the relic-density calculation in Sect. 2.3.2 also remains qualitatively unaltered in the presence of a light mediator down to the kinematic threshold $m_\phi = m_\chi$. Below this threshold, annihilation into pairs of on-shell mediators becomes kinematically accessible. Moreover, below this threshold, the behavior of the thermally-averaged annihilation cross-section transitions from $\langle\sigma|v|\rangle \propto m_\chi^2/m_\phi^4$ to $\langle\sigma|v|\rangle \propto 1/m_\chi^2$ because m_χ is always the dominant energy scale entering into the propagators for all diagrams contributing to this annihilation cross-section. Above this kinematic threshold, by contrast, we find that the correct relic density can be obtained for perturba-

tive couplings between ϕ and both the dark-sector and visible-sector fermions in our theory, provided that $m_\chi \lesssim \mathcal{O}(10 \text{ TeV})$.

In light of these considerations, we emphasize that the monojet and mono-W/Z limits we have discussed here should not be interpreted as exclusion bounds, but rather as relations which indicate the regions within which LHC data can be interpreted as requiring that the mediator particle(s) ϕ not be particularly heavy. Indeed, the suppression scale $M_{\rm I}$, $M_{\rm II}$, or $M_{\rm III}$ in each of our three coupling scenarios can still be large even if m_ϕ is light, provided the coupling between ϕ and either χ or the SM quarks is small.

2.4 Results

In the previous section, we outlined the physics that determines the reach of various direct-detection experiments, assuming only pseudoscalar interactions between dark matter and Standard-Model quarks. We also outlined the physics that determines the cosmological dark-matter abundances after freeze-out, and summarized the physics that determines the reach of monojet and mono-W/Z searches at the LHC. As we saw in Sect. 2.3, all of these calculations depend to varying degrees on the particular flavor coupling structure assumed (*i.e.*, whether we are operating within Scenario I, Scenario II, or Scenario III), and on the particular value of θ in each case.

The results of these analyses are shown in Fig. 2.2. The reaches of the current and future direct-detection experiments considered in this study are shown in red, purple, and blue (along with their associated uncertainties); for the COUPP-60 experiment we have assumed an exposure of 10^5 kg d while for the PICO-250L experiment we have assumed three years of running with a 500 kg fiducial mass [54]. Likewise, the black contour in each case corresponds to the condition $\Omega_\chi = \Omega_{\rm DM}$, which one would naïvely expect to occur for $\langle \sigma |v| \rangle \approx 1$ pb. The orange dashed curve, by contrast, explicitly indicates the points for which $\langle \sigma |v| \rangle = 1$ pb, and the peach-colored and yellow-colored bands around it correspond to the regions within which the annihilation cross-section matches this value to within an increasing number of powers of ten (*i.e.*, 0.1 pb $\leq \langle \sigma |v| \rangle \leq$ 10 pb and 0.01 pb $\leq \langle \sigma |v| \rangle \leq$ 100 pb

respectively). Finally, the blue dashed curve and cyan dot-dashed curve respectively indicate the lower limits on $M_{\rm I}$, $M_{\rm II}$, or $M_{\rm III}$ from monojet and mono-W/Z searches at the LHC in the case of a heavy mediator.

Note that we have included the abundance and collider curves within these plots merely in order to provide guidance when interpreting the impact of the direct-detection curves, and to indicate regions of specific interest. In particular, the collider and abundance curves do not represent strict bounds in any sense. For example, within each panel of Fig. 2.2, the region of the (m_χ, M_*) plane *below* the $\Omega_\chi \sim \Omega_{\rm DM}$ contour (with M_* representing either $M_{\rm I}$, $M_{\rm II}$, or $M_{\rm III}$, as appropriate) is actually consistent with observational limits under the assumption that some additional contribution makes up the remainder of $\Omega_{\rm DM}$. Conversely, the region *above* this contour can also be consistent with a thermal relic dark-matter candidate if the branching fraction for dark-matter annihilation into visible-sector particles is less than unity due to the presence of additional annihilation channels. This will also be true if an additional source of entropy production dilutes the relic abundance after freeze-out. Moreover, as discussed in Sect. 2.3.2, the abundance-related orange and black curves in Fig. 2.2 do not represent true relic-density limits if $m_\phi < m_\chi$. Similarly, as discussed in Sect. 2.3, our monojet and mono-W/Z collider curves only represent exclusion bounds under the assumption that the contact-operator description of our scalar/pseudoscalar interaction remains valid up to the TeV scale. When this is not the case, the bounds can be far weaker or even effectively disappear.

As we see from Fig. 2.2, the dark-matter abundance does not depend significantly on the value of θ in Scenarios I or III. By contrast, in Scenario II, our results depend sensitively on θ due to the enhanced couplings to third-generation quarks relative to those of the first and second generations. Indeed, in Scenario II the abundance contours have sharp kinks or discontinuities that are not apparent in Scenarios I or III. This behavior ultimately arises because the couplings to the SM quarks in Scenario II are proportional to their masses, leading to a dramatic enhancement in the annihilation rate when the thresholds for new annihilation channels into heavy quark species are crossed. However, this assumes that

the dark-matter coupling to these heavy-quark species is substantial — a feature that is ultimately θ-dependent.

Overall, examining the plots in Fig. 2.2, we see that there are three main conclusions which may be drawn. The first and most significant result demonstrated in Fig. 2.2 is that there are regions of parameter space for which a thermal abundance matching $\Omega_{\rm DM}$ is not only consistent with current experimental limits on the pseudoscalar operator, but can actually be probed by the next generation of direct-detection experiments. This does not occur in merely one or two fine-tuned cases, but rather as a fairly generic result for all three scenarios defined in Sect. 2.1 and for most values of θ.

Second, we observe that in some cases, the opposite is true: the reach of our direct-detection experiments is significantly less than might be expected based on the magnitudes of the $\Delta\tilde{q}^{(N)}$ coefficients. This is particularly true for the $\theta = \pi/4$ case of Scenario I, or the $\theta = 0$ case of Scenario II. Indeed, in such cases, we see that the direct-detection experiments cannot even probe that portion of the parameter space that would be associated with a thermal relic. Moreover, we see from Fig. 2.2 that the uncertainties in these cases are sufficiently broad that the direct-detection experiments may not even have any significant reach at all! Ultimately, these effects can easily be understood in relation to Fig. 2.1, where we have seen that for both of these cases the effective dark-matter/nucleon couplings themselves come extremely close to vanishing. (A similar thing would also have happened for $\theta \approx \pi/8$ in Scenario III, if such a θ-value were being plotted in Fig. 2.2.) As discussed in Sect. 2.1, these are situations in which the dark matter couples significantly to quarks, but not to nucleons. In such cases, we conclude that the non-observation of a dark-matter signal in COUPP-4 and in future direct-detection experiments need not rule out the existence of dark matter which nevertheless still couples to quarks and which could therefore potentially produce a signal at collider experiments.

Finally, conversely, we see that the effects of isospin violation (*i.e.*, variations in the value of θ) can have dramatic effects, potentially enhancing the reach of direct-detection experiments quite significantly compared with the reach of these experiments when nucleon-

level isospin symmetry is preserved. For example, in Scenario I, we note that the reach of PICO-250L is approximately 20 times greater (in terms of the values of $M_{\rm I}$ being probed) for $\theta = 0$ than for $\theta = \pi/4$.

2.5 Conclusions

In this chapter, we have studied the sensitivity of direct-detection experiments to dark matter which couples to quarks through dimension-six effective operators of the form $\mathcal{O}_{\chi q}^{(\rm SP)} \sim c_q(\overline{\chi}\chi)(\overline{q}i\gamma^5 q)$, utilizing (for illustrative purposes) several distinct benchmark choices for the quark couplings c_q. As we discussed, such effective operators give rise to velocity-suppressed spin-dependent dark-matter/nucleon scattering. Such operators can also give rise to $\overline{\chi}\chi \to \overline{q}q$ annihilation from a p-wave initial state, as well as "mono-anything" signals at the LHC.

Although it might naïvely be supposed that velocity-dependent spin-dependent scattering would produce an unobservably small event rate at direct-detection experiments, we have demonstrated that this in fact need not be the case. Indeed, as we have seen, the velocity-suppression factors that arise in the pseudoscalar matrix element can be compensated by extra enhancement factors which also emerge in the pseudoscalar case when relating the corresponding pseudoscalar quark currents to effective pseudoscalar nucleon currents. These latter enhancement factors are of size $\mathcal{O}(10^2 - 10^3)$ relative to similar factors associated with velocity-*independent* spin-dependent scattering (such as arises through axial-vector interactions). As a result, contrary to popular lore, we see that velocity-suppressed scattering may actually be within reach of current and upcoming direct-detection experiments. This then necessitates a sensitivity study of the sort that we have performed.

Specifically, our main conclusions are as follows:

- We have shown that there exist a large class of models for which the couplings of the $\mathcal{O}_{\chi q}^{(\rm SP)}$ operators are consistent with a thermal relic density which matches observation.
- A subset of the above parameter space is excluded by current bounds from COUPP-4,

and it is expected that an even larger region of this viable parameter space will be probed by COUPP-60 and PICO-250L.

- While part of the parameter space may be constrained by LHC bounds if the contact-operator approximation remains valid at the TeV scale, there are a wide range of models for which spin-dependent scattering is actually the discovery channel. As we have seen, this is true because the velocity-suppression effects normally associated with pseudoscalar couplings can be overcome through nucleonic effects that emerge in relating quark pseudoscalar currents to nucleon pseudoscalar currents.

- Conversely, there are special situations (often associated with isospin-preserving limits) in which these same nucleonic effects render direct-detection experiments utterly insensitive to non-zero couplings between dark matter and SM quarks. In other words, we have seen that dark matter can have a significant, non-vanishing coupling to quarks and yet simultaneously have no coupling to nucleons! This opens up the intriguing possibility that collider experiments and other indirect-detection experiments could potentially see dark-matter signals to which direct-detection experiments would be utterly blind. This may be extremely relevant in case of future apparent conflicts between positive signals from collider experiments and negative results from direct-detection experiments.

- Finally, we see that isospin-*violation* generally tends to *enhance* dark-matter signals in direct-detection experiments relative to the signals which would have been expected if the quark/nucleon couplings were isospin-preserving. Moreover, for pseudoscalar couplings, this enhancement is not just a factor of two or three (as would be the case for axial-vector interactions), but a factor of ten or more. This then opens up the possibility that direct-detection experiments can be sensitive to such pseudoscalar couplings.

A few comments are in order, especially in relation to the last two points above. In Scenario I, dark-matter/nucleon couplings are maximally isospin-violating when $\theta \approx 0$ or

$\theta = \pi/2$. Interestingly, these cases provide the greatest sensitivity for direct-detection experiments (such as PICO-250L) which are sensitive to spin-dependent scattering. By contrast, detectors which are only sensitive to spin-independent scattering would have no chance of discovering such events, even if velocity-dependent effects are included. This is because, as discussed in Sect. 2.1, all terms originating from $\mathcal{O}_{\chi q}^{(\mathrm{SP})}$ which contribute to the scattering cross-section — and not just those at leading order — are spin-dependent.

On the other hand, we have seen that the sensitivity of direct-detection experiments is especially poor in the isospin-conserving cases (such as $\theta \approx \pi/4$ in our Scenario I) for which the couplings to up- and down-quarks are similar. This poor sensitivity is ultimately the result of a destructive interference amongst these quark-level couplings, resulting in a small net coupling to both protons and neutrons. Indeed, in the limit within Scenario I for which $m_{u,d} \ll m_s$ and $\Delta\tilde{G}^{(N)} \sim 0$, we find $g_{\chi p}, g_{\chi n} \to 0$ identically at $\theta = \pi/4$. Note that result is detector-independent: one obtains a large suppression in the event rate *regardless* of whether the detector is sensitive to spin-dependent scattering from protons or neutrons. Moreover, since the dark-matter bilinear is a scalar, dark-matter annihilation is p-wave-suppressed. Thus, although the annihilation rate at the time of freeze-out may have been large enough to ensure the correct relic density, the annihilation cross-section at the current epoch would be so small as to be unobservable. Dark-matter models of this sort would be difficult to probe via any direct- or indirect-detection experiments.

In this chapter, we considered three different scenarios for the couplings c_q between the dark matter and SM quarks. These correspond to different weightings for the various contributions from the light quarks to the resulting dark-matter/nucleon couplings and their associated dark-matter scattering rates. In Scenario I, for example, the dominant contributions came from the couplings of the quarks of the first generation, but we found that there also exist small contributions from the strange quark and heavier quarks. Likewise, in Scenario I we found that $g_{\chi p}, g_{\chi n} \to 0$ for $\theta = \pi/4$. In Scenario III, by contrast, the additional contributions from the strange and heavier quarks are absent. Moreover, since the c_q coefficients of Scenario III scale with the masses of the quarks, we instead find that

$g_{\chi p}, g_{\chi n} \to 0$ for $\tan\theta = m_u/m_d$. In this connection, it is perhaps worth emphasizing that it is only for the pseudoscalar interactions that there exist values of θ for which both $g_{\chi p}$ and $g_{\chi n}$ vanish simultaneously. As can be seen in Fig. 2.1, this does not happen for any of the analogous couplings in the axial-vector case.

Finally, Scenario II is an example of a class of models in which the largest dark-matter coupling is to the strange quark or the heavy quarks. As discussed earlier, this particular example is motivated by minimal flavor-violation. As evident from Fig. 2.2, the sensitivity of direct-detection experiments to viable dark-matter models is suppressed for such cases. It is clear why this occurs. In Scenario II, the largest dark-matter couplings are those to the second- and third-generation quarks — indeed, these are ultimately bounded by constraints on the relic density. Unfortunately, the contributions from these second- and third-generation quark couplings to dark-matter scattering are relatively small as a result of a suppression of the corresponding nucleon enhancement factors, while the coupling to first-generation quarks is necessarily small by assumption in this scenario.

Depending on the details of the short-distance (ultraviolet) physics model we imagine, dark matter which couples to quarks through an effective operator such as $\mathcal{O}_{\chi q}^{(\mathrm{SP})}$ may also be amenable to "mono-anything" searches at the LHC. In particular, for isospin-conserving variants in which the first-generation quarks dominate the scattering, LHC searches may be the only viable options for discovery. Moreover, LHC sensitivity may be enhanced for flavor structures such as those in Scenario II which are motivated by minimal flavor-violation, due to the large contribution to the LHC event rate that arises from the couplings to the heavy quarks. Ultimately, however, LHC sensitivity depends on the details of the model, and in particular on the flavor structure of the couplings. For the wide class of models in which such large LHC event rates do not occur, spin-dependent direct-detection will then be the discovery search channel.

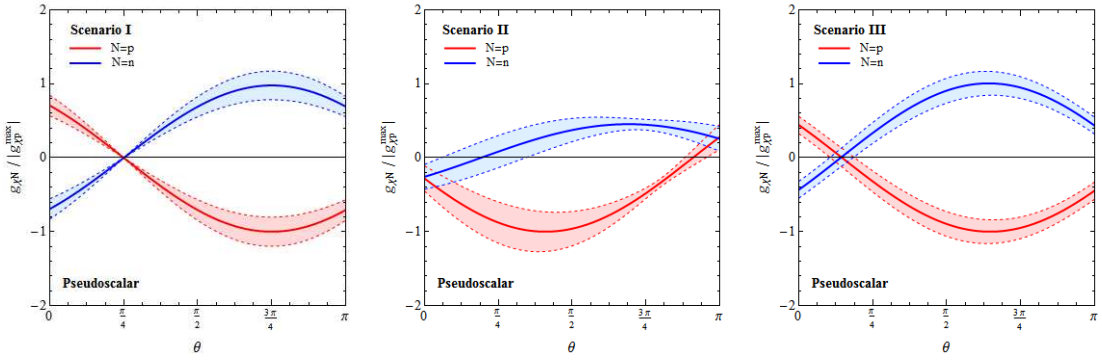

for comparison purposes:

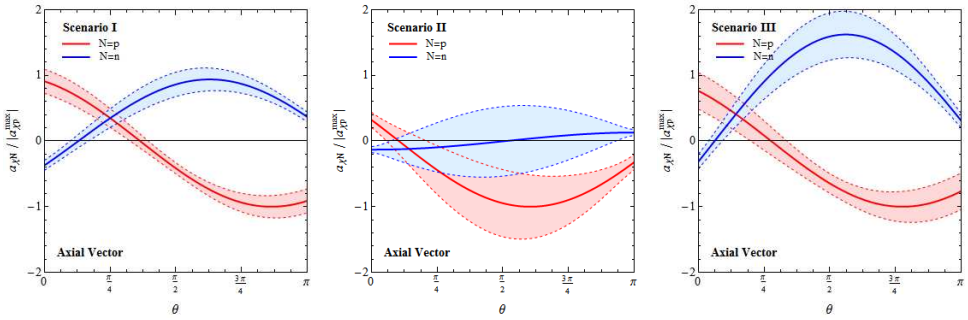

Figure 2.1: The effective proton and neutron dark-matter couplings $g_{\chi p}$ (red) and $g_{\chi n}$ (blue), plotted as functions of θ for each of the three coupling scenarios discussed in the text. Panels in the upper row show the behavior of the pseudoscalar couplings in each scenario, while the panels in the lower row show the behavior of the corresponding axial-vector couplings. The dashed lines in each panel correspond to the central values for these couplings, while the shaded regions indicate the 1σ uncertainty bands around these central values. Note that in each panel, both $g_{\chi p}$ and $g_{\chi n}$ have been normalized to the maximum possible central value of $|g_{\chi p}|$ attainable in each scenario.

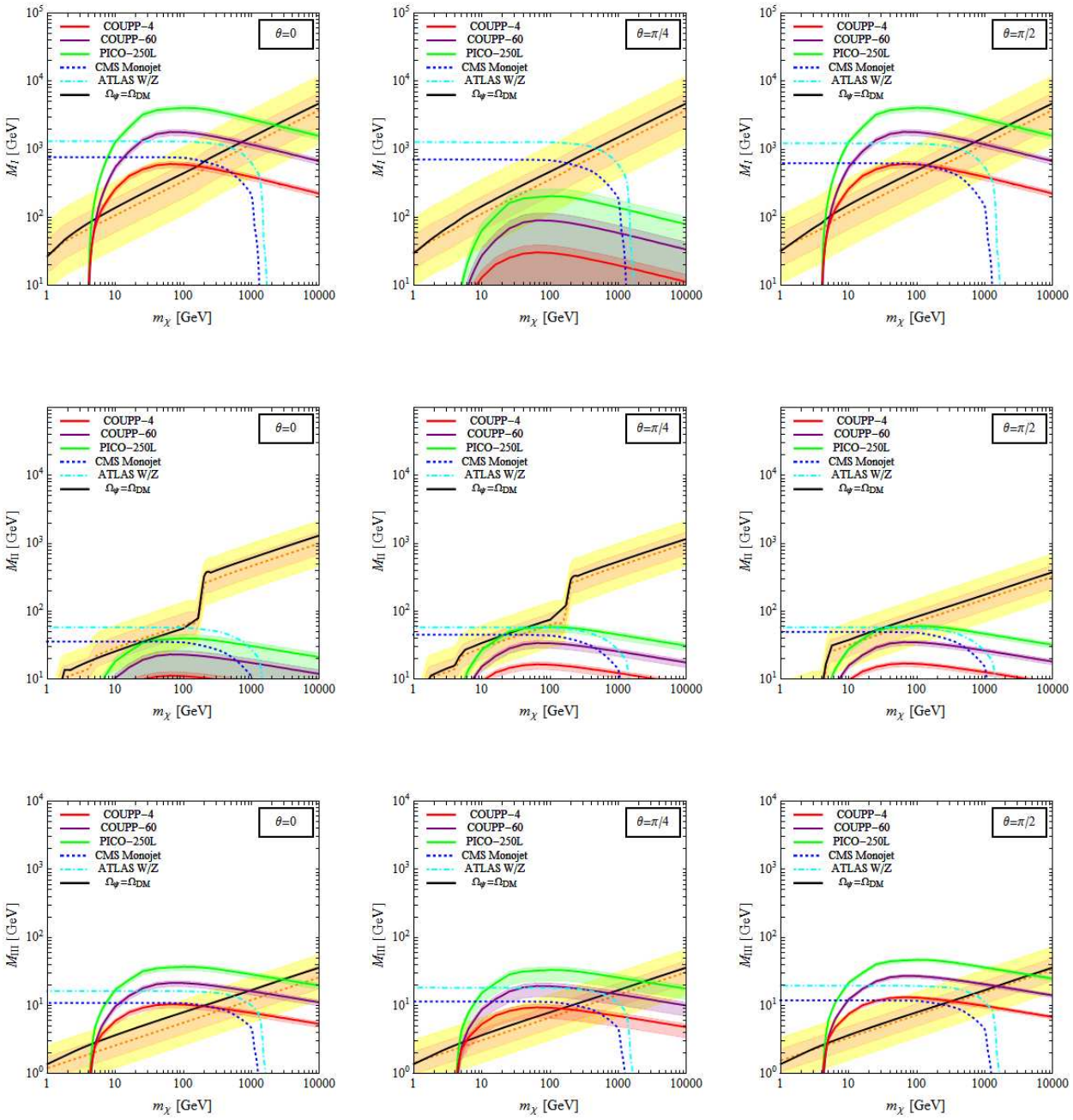

Figure 2.2: Experimental reach of direct-detection experiments, assuming pseudoscalar interactions with the benchmark coupling structures of our Scenario I (top row), Scenario II (center row), and Scenario III (bottom row), with $\theta = 0$ (left column), $\theta = \pi/4$ (center column), and $\theta = \pi/2$ (right column) in each case. These coupling structures are discussed in Sect. 2.1.3, and each panel is plotted as a function of the dark-matter mass m_χ and the mass scale $M_{\rm I}$, $M_{\rm II}$, or $M_{\rm III}$ associated with the corresponding scenario. We see from these plots that there are many situations in which upcoming direct-detection experiments can easily reach into the range of greatest interest for thermally-produced dark matter and its possible collider signatures — even when only pseudoscalar interactions between dark matter and Standard-Model quarks are assumed.

CHAPTER 3
A NEW CHANNEL IN DARK-MATTER COMPLEMENTARITY

There are many seemingly-independent signals we can search for in the hunt for dark matter. At colliders, we can search for dark matter production by searching for high p_T jets and W/Z bosons associated with large missing energy/momentum – a sign of the inert dark matter streaming freely through the detector. Another possibility is the direct detection of interactions between galactic-halo dark matter and standard model target material at sensitive underground detectors. A third avenue involves the indirect detection of dark matter through self-annihilations of it's cosmological abundance into standard model decay products. These indirect searches can be carried out by observing, with both terrestrial and satellite telescopes, astrophysical objects expected to have high densities of cosmological dark matter. As we have discussed, these seemingly-different processes are often related to each other through crossing symmetries, and thus can lead to a rich *complementarity* structure between the processes. In this way, we can use different experiments to cover different areas of the parameter space and thus "cover more ground." Alternatively, we can use the results (ideally, the detection of dark matter) at one experiment to predict the results of another experiment.

Most studies of this complementarity implicitly assume that the dark sector consists of a single particle χ. Indeed, many studies further focus on a particular effective $2 \to 2$ interaction between dark matter and ordinary matter, as sketched in Fig. 3.1(a); the three complementary search strategies then correspond to physical processes in which we imagine time flowing in the directions associated with the three different blue arrows. Indeed, because of the assumed single-particle nature of the dark sector, we further observe that the scattering that underlies direct-detection experiments is necessarily elastic. Likewise, the dark-matter-induced production of ordinary matter that underlies indirect-detection experiments exclusively takes place through annihilation of the dark-matter particle with

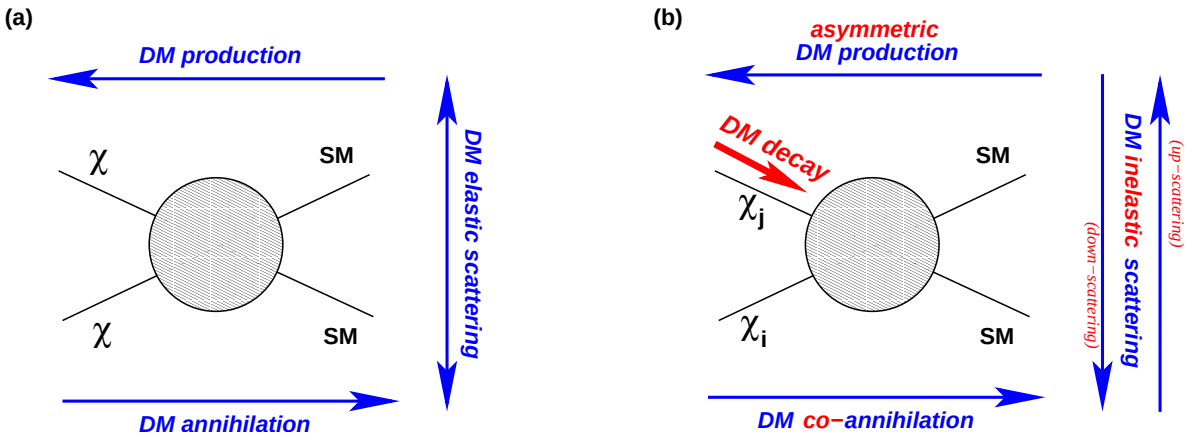

Figure 3.1: (a) In single-component theories of dark matter, the $2 \to 2$ amplitudes for dark-matter production, annihilation, and scattering are related to each other through various crossing symmetries. These different processes correspond to different directions (blue arrows) for the imagined flow of time through a single four-point diagram. (b) In *multi-component* theories of dark matter, by contrast, there can be many different dark-matter components χ_i with differing masses m_i. Taking $m_i \neq m_j$ then changes the kinematics associated with each of the previous complementary directions: dark-matter production becomes *asymmetric* rather than symmetric; dark-matter annihilation of one dark particle against itself becomes *co*-annihilation between two different dark species; and elastic dark-matter scattering becomes *inelastic*, taking the form of either "down-scattering" or "up-scattering" depending on whether it is the incoming or outgoing dark-matter particle which has greater mass. Even more importantly, however, the existence of a non-minimal dark sector opens up the possibility for an additional process which is also related the others by crossing symmetries: dark-matter *decay* from heavier to lighter dark-matter components. This process corresponds to a *diagonal* direction for the imagined flow of time, as shown, and thus represents a new direction for dark-matter complementarity.

itself or its antiparticle.

This situation becomes far richer in *multi-component* theories of dark matter[1]. In particular, if we assume that the dark sector consists of at least two different dark-matter components χ_i and χ_j with differing masses $m_i \neq m_j$, then for $i \neq j$ the situation differs from the single-particle case in two fundamental ways. First, the kinematics associated with each of the traditional complementarity directions is altered: dark-matter production becomes *asymmetric* rather than symmetric; dark-matter annihilation of one dark particle against itself or its antiparticle becomes *co*-annihilation between two different dark

[1]For examples of top-down models which give rise to specific multi-component scenarios, see [75–80]

species; and dark-matter scattering — previously exclusively elastic — now becomes *inelastic*, taking the form of either "up-scattering" [25, 81–83] or "down-scattering" [27, 84–86] depending on whether it is the incoming or outgoing dark-matter particle which has greater mass. These kinematic changes are illustrated in Fig. 3.1(b), and can significantly affect the phenomenology of the corresponding processes. But perhaps even more importantly, an entirely new direction for dark-matter complementarity also opens up: this is the possibility of dark-matter *decay* from heavier to lighter dark-matter components. Indeed, this process corresponds to the *diagonal* direction for the imagined flow of time, as shown in Fig. 3.1(b), and thus represents an entirely new direction for dark-matter complementarity. Such a direction was not available in single-component theories of dark matter due to phase-space constraints, and is ultimately driven by the non-zero mass difference between the associated parent and daughter dark-matter particles.

Thus, if the dark sector consists of multiple components, a generic four-point interaction of the sort shown in Fig. 3.1 will lead to an enhanced set of complementarities across different classes of dark-matter experiments. Direct-detection experiments will potentially be sensitive to nuclear recoils from elastic scattering, up-scattering, and down-scattering, while indirect-detection experiments will potentially be able to measure fluxes from dark-matter self-annihilation, dark-matter co-annihilation, and dark-matter decay. Likewise, collider experiments will potentially involve dark-matter production which is both symmetric and asymmetric. Of course, neither inelastic down-scattering nor dark-matter decay will be relevant for present-day experiments unless the more massive dark-matter components have significant cosmological abundances at the present time; indeed, this already places one set of constraints on their decay widths. In this connection, we also note that this same four-point interaction can in principle also give rise to an additional process in which a heavy ordinary-matter particle decays to a lighter ordinary-matter particle along with two dark-sector particles. However, for all cases involving two quarks (which will be our main interest in this chapter), such processes cannot occur in a flavor-conserving theory. Processes of this type will therefore not be considered further in this work. We nevertheless

note that in general, exotic decays of the Higgs or of Standard-Model electroweak gauge bosons could potentially provide yet another complementary probe into the nature of the dark sector [87–90].

Two Examples

In order to illustrate these extra complementarities and the power they provide in surveying the parameter space of theories with multi-component dark sectors, let us imagine that the dark sector consists of two Dirac fermions χ_1 and χ_2 which are neutral under all Standard-Model gauge symmetries and have corresponding masses m_1 and m_2 respectively, with $m_2 > m_1$. We shall also assume that our fundamental four-point interaction in Fig. 3.1(b) is described by an effective dimension-six four-fermi contact Lagrangian operator that couples these two dark-matter particles to two Standard-Model quarks q. For concreteness, in this chapter we shall consider two distinct examples of such operators, with the first taking the form of a flavor-conserving scalar (S) interaction

$$\mathcal{L}_{\rm int}^{\rm (S)} \;=\; \sum_{q=u,d,s,\ldots} \frac{c_q^{\rm (S)}}{\Lambda^2} (\overline{\chi}_2 \chi_1)(\overline{q} q) \;+\; \text{h.c.}\;, \tag{3.1}$$

and the second taking the form of a flavor-conserving axial-vector (A) interaction

$$\mathcal{L}_{\rm int}^{\rm (A)} \;=\; \sum_{q=u,d,s,\ldots} \frac{c_q^{\rm (A)}}{\Lambda^2} (\overline{\chi}_2 \gamma_\mu \gamma^5 \chi_1)(\overline{q} \gamma^\mu \gamma^5 q) \;+\; \text{h.c.} \tag{3.2}$$

We have chosen these two forms of interactions as canonical examples of operators giving rise to spin-independent (SI) and spin-dependent (SD) interactions, respectively. In these operators, $q = u, d, s, \ldots$ specifies a particular quark flavor while c_q is the corresponding dark-matter/quark coupling and Λ denotes the mass scale of the new (presumably flavor-diagonal) physics which might generate such effective interactions. Note that these operators are separately invariant under both charge conjugation (C) and parity (P).

Within the operators in Eqs. (3.1) and (3.2), we shall make two further assumptions. First, in each case, we shall assume a flavor structure for our dark-matter/quark couplings

c_q such that

$$c_u = -c_d = c_c = -c_s = c_t = -c_b \;\equiv\; c \;. \tag{3.3}$$

We have chosen this flavor structure, which is maximally isospin-violating within each generation, because it ultimately maximizes the axial-vector decay rate and thereby places the strongest bounds on our examples. Second, we shall assume (as a cosmological input) that the heavier dark-matter particle χ_2 is metastable and carries the vast majority of the dark-matter abundance, *i.e.*, $\Omega_2 = \Omega_{\rm CDM} \approx 0.26$ and $\Omega_1 = 0$. As we shall see, this assumption also maximizes the rates for all relevant processes and thereby places the strongest bounds on our examples. This assumption also simplifies our analysis somewhat. We shall therefore take this to be a conservative "benchmark" for our study. We remark, however, that none of the primary qualitative aspects of our results will ultimately depend on this choice, and indeed other choices such as $\Omega_1 \approx \Omega_2 \approx \Omega_{\rm CDM}/2$ also lead to results which are very similar to those we shall obtain here. Such general scenarios will be explored in Ref. [47].

Given these assumptions, our examples each have three fundamental parameters: the effective coupling c/Λ^2, the mass m_2 of the heavier dark-matter component, and the dark-sector mass splitting $\Delta m_{12} \equiv m_2 - m_1$. Our goal is to explore the resulting $(c/\Lambda^2, \Delta m_{12})$ parameter space for different values of m_2. In this connection, however, we remark that since the operators in Eqs. (3.1) and (3.2) are non-renormalizable, they can only be interpreted within the context of an effective field theory whose cutoff scale is parametrically connected to Λ. As a result, our use of such operators when calculating phenomenological bounds already presupposes that the energy scales associated with the relevant processes in each case do not exceed Λ. Assuming $\mathcal{O}(1)$ operator coefficients, this requires $\Lambda \gtrsim \mathcal{O}({\rm GeV})$ for direct-detection bounds; indeed, as we shall see, this value corresponds to nuclear recoil energies $E_R \lesssim 100$ keV in direct-detection experiments. Likewise, for indirect-detection bounds, our requirement for Λ depends on whether we are dealing with dark-matter annihilation or decay: for annihilation this requires $\Lambda \gtrsim \mathcal{O}(m)$ where m is a typical mass of a dark-sector component, while for a dark-matter decay of the form $\chi_2 \to \chi_1 \overline{q} q$ this requires $\Lambda \gtrsim \mathcal{O}(\Delta m_{12})$. Finally, for calculating collider-production bounds, the use of such operators

is strictly valid only if $\Lambda \gtrsim \mathcal{O}(\text{TeV})$. If this last condition is not met, the resulting collider bounds should be viewed only as heuristic, and one would require a more complete theory (for example, involving potentially light mediators connecting the dark and visible sectors) before being able to make more precise statements.

As $\Delta m_{12} \to 0$, our dark-matter production and direct-detection processes proceed exactly as they would for a single dark-matter particle χ of mass $m = m_2$. Indeed, in this limit direct detection can only proceed through elastic scattering; likewise, the interactions in Eq. (3.1) or (3.2) do not permit dark-matter decay. Thus, the $\Delta m_{12} \to 0$ limit effectively embodies the physics of a traditional single-component dark sector with mass m_2, and in this case our bounds are relatively straightforward: one simply finds that direct-detection and collider experiments place m_2-dependent upper limits on the coupling c/Λ^2. For example, for the coupling structure in Eq. (3.3) and for $m_2 = 100$ GeV, we find from direct-detection experiments [51, 91] that

$$\begin{cases} c^{(\text{S})}/\Lambda^2 \lesssim 2.8 \times 10^{-10}\ \text{GeV}^{-2}\ , \\ c^{(\text{A})}/\Lambda^2 \lesssim 1.1 \times 10^{-5}\ \text{GeV}^{-2}\ ; \end{cases} \tag{3.4}$$

we likewise find from collider monojet [62–65] and mono-W/Z [66, 67] constraints that

$$\begin{cases} c^{(\text{S,A})}/\Lambda^2 \lesssim 1.4 \times 10^{-6}\ \text{GeV}^{-2}\ \ (\text{monojet})\ , \\ c^{(\text{S})}/\Lambda^2 \lesssim 5.0 \times 10^{-7}\ \text{GeV}^{-2}\ \ (\text{mono-}W/Z)\ , \\ c^{(\text{A})}/\Lambda^2 \lesssim 3.1 \times 10^{-7}\ \text{GeV}^{-2}\ \ (\text{mono-}W/Z)\ . \end{cases} \tag{3.5}$$

However, by turning on Δm_{12}, we can now explore the effects of non-minimality in the dark sector and thereby assess the impact of the new kinematics and new complementarities that arise.

With an eye towards exploring those regions of parameter space which are likely to be of maximal phenomenological interest from a complementarity perspective, we shall restrict our attention to situations with $\Delta m_{12} \lesssim \mathcal{O}(\text{MeV})$; we stress, however, that there

is no fundamental reason that larger Δm_{12} cannot also be considered. Likewise, since we are taking $\Omega_1 = 0$ for simplicity, the relevant dark-matter processes for the operators in Eqs. (3.1) and (3.2) are limited to inelastic down-scattering, asymmetric collider production, and dark-matter decay. We shall now discuss each of these in turn.

3.1 Inelastic Down-Scattering

We begin by considering the bounds from direct-detection experiments through the inelastic down-scattering process $\chi_2 N_i \to \chi_1 N_f$ where N_i and N_f denote the initial and final states of the nucleus N in the detector substrate. In general, the total differential nuclear-recoil rate is given by

$$\frac{dR}{dE_R} \;=\; \frac{\tilde{N}\rho_2^{\rm loc}}{m_2} \int_{v>v_{\rm min}^{(21)}} v\mathcal{F}_2(\vec{v}) \left(\frac{d\sigma_{21}}{dE_R}\right) d^3v \;, \tag{3.6}$$

where $\tilde{N}$ is the number of nuclei per unit detector mass, where $\rho_2^{\rm loc}$ is the local energy density of χ_2, where $\mathcal{F}_2(\vec{v})$ is the distribution of detector-frame velocities $\vec{v}$ for χ_2 in the local dark-matter halo, where $v = |\vec{v}|$, where $v_{\rm min}^{(21)}$ is the E_R-dependent "threshold" velocity (*i.e.*, the minimum incoming velocity for which scattering with recoil energy E_R is possible), and where $d\sigma_{21}/dE_R$ is the differential cross-section for the process $\chi_2 N_i \to \chi_1 N_f$. When evaluating these cross-sections, we require nuclear form factors; for this purpose we utilize the software packages associated with Ref. [50]. The corresponding limits on our $(c/\Lambda^2, \Delta m_{12})$ parameter space are then respectively derived using the most recent LUX [91] and COUPP-4 [51] data for the scalar and axial-vector cases, respectively. Roughly speaking, this data can be taken as requiring $R \lesssim 1.81 \times 10^{-4}\,{\rm kg}^{-1}{\rm day}^{-1}$ and $R \lesssim 4.97 \times 10^{-2}\,{\rm kg}^{-1}{\rm day}^{-1}$ for the recoil-energy windows 3 keV $\leq E_R \leq$ 25 keV and 7.8 keV $\leq E_R \leq$ 100 keV, respectively. In this connection, we note that a threshold detector such as COUPP-4 is actually sensitive to scattering events with arbitrarily large recoil energies. However, for $E_R \gtrsim 100$ keV, there are considerable uncertainties associated with distinguishing these events from background. To be conservative, we therefore adopt the above upper limit for the corresponding E_R window.

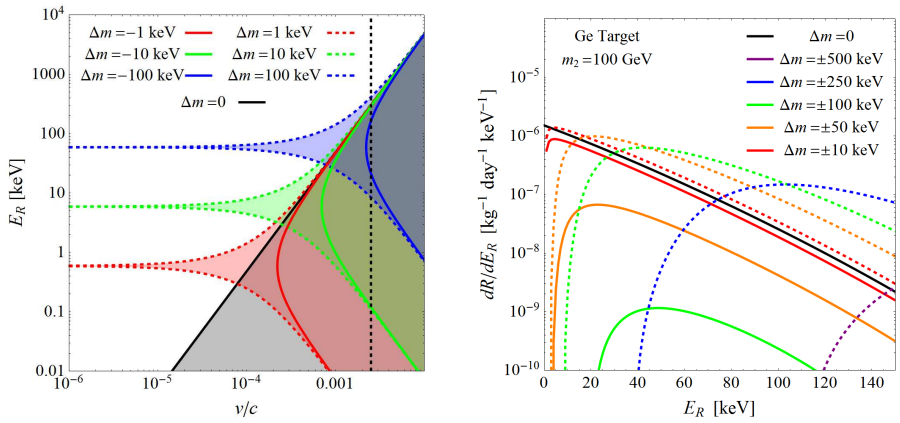

Figure 3.2: Recoil-energy spectra for inelastic scattering $\chi_2 N_i \to \chi_1 N_f$ off a germanium nucleus, with $m_1 \neq m_2 = 100$ GeV. *Left panel:* Allowed ranges of recoil energy E_R as a function of incoming dark-matter particle velocity v for different $\Delta m \equiv m_2 - m_1$, for both "down-scattering" ($\Delta m > 0$, dotted lines) and "up-scattering" ($\Delta m < 0$, solid lines). The elastic case with $\Delta m = 0$ is also shown (solid black line), as is the maximum velocity cutoff associated with the galactic escape velocity (dashed black line). *Right panel:* Corresponding recoil spectra dE_R/dR for both down-scattering (dotted lines) and up-scattering (solid lines), for different values of Δm. The solid black curve represents the $\Delta m = 0$ elastic-scattering case. For all spectra shown, the scattering is assumed to be spin-independent, with cross-section per nucleon $\sim 10^{-46}$ cm^{-2}.

While much of this analysis is completely standard, the primary new ingredient is the change in scattering kinematics from elastic to inelastic. If the scattering had been elastic (*e.g.*, $\chi_j N_i \to \chi_j N_f$), the possible allowed recoil energies would have been given by the standard expression $E_R = E_{jN}(1 + \cos\theta)$ where $E_{jN} \equiv \mu_{jN}^2 v_j^2 / m_N$ and $0 \leq \theta \leq \pi$. Here v_j is the speed of the incoming dark-matter particle in the detector frame, m_N the mass of the nucleus, θ the scattering angle in the center-of-mass frame, and $\mu_{\chi N}$ the reduced mass of the χ/N system. For inelastic $\chi_j N_i \to \chi_i N_f$ scattering, by contrast, the possible allowed recoil energies are instead given by $E_R = E_{jN}(1+r+\sqrt{1+2r}\cos\theta)$ where $r \equiv [\mu_{iN}/(\beta\mu_{jN})^2]\Delta m_{ij}$ with $\beta \equiv v_j/c$ and $\Delta m_{ij} \equiv m_j - m_i$.

There are two important consequences of this change in kinematics. First, in the case of down-scattering, we see that for $E_R \approx E_R^* \equiv [m_i/(m_i + m_N)]\Delta m_{12} c^2$ the required incoming velocity is essentially zero. Such threshold-free scattering with non-zero recoil energy would not have been possible in the traditional case of elastic scattering, but the required input

energy in the inelastic case comes directly from species conversion within the dark sector (essentially from rest mass liberated within the dark sector) rather than from incoming dark-sector kinetic energy.

Second, we also observe that for any incoming dark-matter velocity v, we have not only a finite upper limit on the allowed nuclear recoil energy E_R but also a non-zero *lower* limit. This feature holds for both down-scattering and up-scattering, and in turn implies that the corresponding recoil spectrum dR/dE_R is negligible not only above a maximum value of nuclear recoil energy *but also below a minimal value.* Indeed, in the case of down-scattering (*i.e.*, $\Delta m_{ij} > 0$), this allowed range of recoil energies is centered around E_R^* and becomes exceedingly narrow as the incoming velocity goes to zero. This is especially important since $v \leq v_{\rm esc} + v_E$, where $v_{\rm esc} \approx 540$ km/s is the galactic escape velocity and $v_E \approx 231$ km/s is the speed of the Earth in the galactic frame. These features are illustrated in Fig. 3.2, and will play an important role in what follows.

3.2 Asymmetric Collider Production

Multi-component operators such as those in Eqs. (3.1) and (3.2) can also be probed through the collider-production direction. However, unlike the single-component case, the production processes induced by the operators in Eqs. (3.1) and (3.2) take the form $qq \to \chi_1\chi_2$. Thus, we are dealing with *asymmetric* collider production of dark matter.

Despite this new feature, such dark-matter production processes can nevertheless be most effectively constrained just as for single-component theories — *i.e.*, through monojet searches at ATLAS [62, 63] and CMS [64, 65] and mono-W/Z searches at ATLAS [66, 67]. Indeed, these limits are directly applicable to the asymmetric production of dark-matter particles χ_1 and χ_2 as well as to a pair of identical dark-matter particles because the values of Δm_{12} for which inelastic scattering can play a significant role in direct detection (and for which χ_2 is stable on cosmologically timescales without exceedingly large Λ) are negligibly small in comparison with the energy scales relevant for collider physics. Thus, while the kinematics associated with the asymmetric production of dark matter differs from that

associated with the more traditional symmetric production, this difference ultimately does not prove phenomenologically significant within the parameter ranges of greatest interest from a complementarity perspective.

3.3 Dark-Matter Decay

We now turn to an analysis of the new (diagonal) complementarity direction which comes into existence for non-zero Δm_{ij}, namely the possibility of decay from heavier to lighter dark-matter components. Once again, our starting points are the operators in Eqs. (3.1) and (3.2) which describe the microscopic (short-distance) interactions between our dark-sector particles χ_i and Standard-Model quarks. However, because we are considering dark-sector mass splittings of size $\Delta m_{12} \lesssim \mathcal{O}(\text{MeV})$, our study of the dark-matter decay induced by the operators in Eqs. (3.1) and (3.2) must instead be performed within the framework of a low-energy *macroscopic* effective field theory in which the physics of Eqs. (3.1) and (3.2) is recast in terms of interactions between our dark-sector particles and the lightest color-neutral states in the visible sector.

In order to transition between these two descriptions, we can use the formalism of chiral perturbation theory[2] based on the low-energy $SU(2)_L \times SU(2)_R \times U(1)_V$ flavor symmetry group of the light (u,d) quarks [97–99]. This technique allows us to systematically generate a complete set of operators which capture the exact symmetry structure of our underlying microscopic Lagrangian, up to unknown (but ultimately measurable) coefficients $\tilde{\lambda}_i \sim \mathcal{O}(1)$. The details behind this calculation will be discussed more fully in Ref. [47]. The upshot, however, is that the scalar interaction in Eq. (3.1) gives rise to an effective Lagrangian of the form [100–103]

$$\begin{aligned}\mathcal{L}_{\text{eff}}^{(\text{S})} &= -\frac{B_0^2(m_u-m_d)\tilde{\lambda}_1 c^{(\text{S})}}{8\pi^2\Lambda^2}\,\overline{\chi}_2\chi_1 \\ &\quad + \frac{B_0\alpha_{\text{EM}}\tilde{\lambda}_2 c^{(\text{S})}}{4\pi\Lambda_C^2\Lambda^2}\,(\overline{\chi}_2\chi_1)F_{\mu\nu}F^{\mu\nu} + \ldots\,, \end{aligned} \tag{3.7}$$

[2] For reviews, see [92–96]

where $B_0 \equiv m_\pi^2/(m_u+m_d)$ and where Λ_C denotes the confinement scale $\Lambda_C \equiv 4\pi f_\pi/\sqrt{N_f}$, with $f_\pi \approx 93$ MeV and $N_f = 2$. Likewise, the axial-vector interaction in Eq. (3.2) gives rise to an effective Lagrangian of the form

$$\begin{aligned}\mathcal{L}_{\rm eff}^{(\rm A)} &= -\frac{c^{(\rm A)}\Lambda_C}{\sqrt{2}\pi\Lambda^2}\left[1+\frac{m_\pi^2}{2\Lambda_C^2}\tilde{\lambda}_3\right](\overline{\chi}_2\gamma^\mu\gamma^5\chi_1)(\partial_\mu\pi^0) \\ &\quad + \frac{\alpha_{\rm EM}\tilde{\lambda}_4 c^{(\rm A)}}{4\pi\Lambda_C^2\Lambda^2}(\overline{\chi}_2\gamma^\mu\gamma^5\chi_1)\partial_\mu(F_{\nu\rho}\tilde{F}^{\nu\rho}) \ + \ldots \end{aligned} \tag{3.8}$$

We stress, however, that there are numerous subtleties involved in extracting these terms from the full chiral perturbation theory formalism. These will be discussed more fully in Ref. [47].

Somewhat surprisingly, the first term of Eq. (3.7) is not an interaction term, but rather an off-diagonal contribution to the mass matrix of the individual dark-sector components! At first glance, this might seem to suggest that the mass eigenstates of the dark sector are not given by the individual $\chi_{1,2}$ components with which we started, but rather by some new linear combinations of these states. However, our original supposition has always been that χ_1 and χ_2 are our physical mass eigenstates with masses m_1 and m_2 respectively — even in the confined phase of QCD within which we have been operating throughout this chapter — and we know that the mass eigenstates of our theory should not change when we reshuffle our strongly interacting degrees of freedom from quarks to color-neutral hadrons. Thus, the contribution from this extra mass term within Eq. (3.7) must ultimately be cancelled by other additional mass terms (*e.g.*, coming from ultraviolet physics and/or other hadronic effects) so as to reproduce the mass eigenstates with which we started. That said, we might worry whether this cancellation might involve a significant degree of fine-tuning. However, it is easy to verify that this is not the case throughout the region of parameter space in which we are primarily interested — *i.e.*, that within which $\Delta m_{12} \gtrsim \mathcal{O}(\text{keV})$ and $\Lambda \gtrsim \mathcal{O}(10\text{ GeV})$. Indeed, within this region of parameter space, the degree of mixing associated with the mass matrix within Eq. (3.7) is negligible compared to Δm_{12}.

We therefore conclude that the mass term appearing within Eq. (3.7) is relatively unim-

portant for the present analysis in which we are focusing exclusively on dark-matter phenomenology within the confined phase of QCD. However, it is perhaps nevertheless worth remarking that terms of this sort can potentially play an important role in dark-matter *cosmology*, especially if the universe experiences a post-inflationary phase with a sufficiently high reheating temperature $T > \Lambda_{\rm QCD}$. At such temperatures, the dark-sector mass matrix could in principle differ from its present-day form in a non-trivial manner. The process of confinement itself might then actually *induce* a rediagonalization of the dark-sector mass eigenstates as part of the QCD phase transition, precisely through the appearance of terms such as those in Eq. (3.7). As a result, the mass eigenstates of the dark sector might not be the same before and after the QCD phase transition. In general, this is a novel effect which arises only for multi-component dark sectors. However, this effect can have a wealth of important theoretical and phenomenological implications, especially for dark-sector components χ_i and χ_j whose mass splittings Δm_{ij} are extremely small. These effects will be discussed further in Ref. [47].

The remaining terms in Eqs. (3.7) and (3.8) are *bona fide* interaction terms. As we see, they come in two types: contact operators (ultimately obtained from integrating out heavy hadronic degrees of freedom) which directly couple our dark-sector components χ_i to photons, and operators which couple our dark-sector components to off-shell pions (which then subsequently decay to two photons). These two sets of operators are illustrated in Fig. 3.3. Together, however, these operators allow us to calculate the widths for the decays $\chi_2 \to \chi_1\gamma\gamma$ through either the scalar or the axial-vector interaction. For $\Delta m_{12} \ll m_{1,2}$, we obtain

$$\begin{aligned}
\Gamma_{\gamma\gamma}^{(\rm S)} &\approx \frac{B_0^2 \alpha_{\rm EM}^2 \tilde{\lambda}_2^2 [c^{(\rm S)}]^2}{8(105\pi^5)\Lambda_C^4 \Lambda^4} (\Delta m_{12})^7 \; , \\
\Gamma_{\gamma\gamma}^{(\rm A)} &\approx \frac{\alpha_{\rm EM}^2 [c^{(\rm A)}]^2}{8(315\pi^5)\Lambda_C^4 \Lambda^4} \left[\tilde{\lambda}_3 - \tilde{\lambda}_4 + \frac{2\Lambda_C^2}{m_\pi^2}\right]^2 (\Delta m_{12})^9 \; .
\end{aligned} \tag{3.9}$$

These decay rates may then be compared against existing bounds on observed photon fluxes in order to constrain our fundamental parameters $(c/\Lambda^2, \Delta m_{12})$ for different values of m_2.

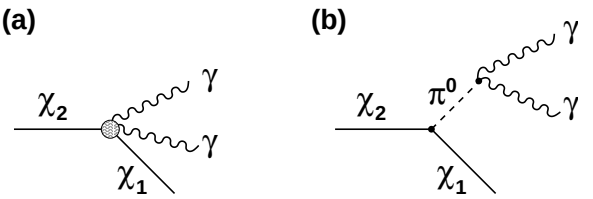

Figure 3.3: Dominant dark-matter decay processes at energies $E \lesssim \mathcal{O}(10^2)$ keV. (a) Dark-matter decay produces two photons through an effective contact operator induced in the chiral perturbation theory by integrating out heavy hadrons. This process is the dominant contributor in the case of the microscopic (quark-level) scalar interaction in Eq. (3.1). (b) Dark-matter decay produces produces two photons via off-shell neutral-pion exchange. Both this process and the process in (a) are the dominant contributors in the case of the microscopic (quark-level) axial-vector interaction in Eq. (3.2).

In particular, assuming an NFW profile for the dark-matter distribution [10], we use the PPPC4DMID software package [104] to determine the diffuse galactic and extragalactic contributions to the differential photon flux arising from dark-matter decay, and require that the predicted photon count not exceed that measured in any bin at the 2σ confidence level. In this context we remark that decays to final states involving neutrinos are also kinematically allowed. However, the contributions to the total widths from such decays are negligible compared with the above, and are thus neglected.

3.4 Results

Combining the constraints from each of the dark-matter directions discussed above, we can now map out the current bounds on the operators in Eqs. (3.1) and (3.2) in the $(c/\Lambda^2, \Delta m_{12})$ parameter space for different values of m_2. Our results are shown in Fig. 3.4 for $m_2 = \{10, 100, 1000\}$ GeV, with $c^{(\mathrm{S})} = c^{(\mathrm{A})} = 1/\sqrt{2}$ and $\tilde{\lambda}_i = 1$ chosen as fixed reference values.

In Fig. 3.4, the pink regions are excluded by bounds on inelastic scattering from direct-detection experiments (LUX [91] and COUPP-4 [51] for the scalar and axial-vector cases, respectively), while the green contour indicates the projected future reach of the LZ 7.2-ton detector [105, 106] in the scalar case and the PICO-250L experiment [54] in the axial-vector case. Likewise, the vertical blue and cyan contours respectively correspond to LHC con-

straints on asymmetric collider production from monojet [62–65] and hadronically-decaying mono-W/Z [66, 67] searches. The collider analysis was performed by generating signal events using the MadGraph 5 [71], Pythia 6.4 [107], and Delphes 2.0.5 [108] software packages, and comparing to the number of background events reported in Refs. [63, 65–67] in order to determine the region excluded at 90% confidence level. Note that there is a $\sim 40\%$ systematic uncertainty in the number of signal events, attributable to uncertainties in the correct treatment of soft QCD and hadronic physics; this uncertainty can affect the bounds on Λ by $\sim 10\%$. In this connection we also remind the reader that these collider-based bounds should be interpreted at best only heuristically if the operators in Eqs. (3.1) and (3.2) are generated by integrating out light mediators or by other new physics which renders $\Lambda \lesssim \mathcal{O}(\text{TeV})$. The yellow and purple shaded regions are excluded by constraints on dark-matter decay from the total diffuse X-ray background measurements of HEAO-1 [109] and INTEGRAL [110], respectively, as these are the experiments which probe the particular energy region of the photon spectrum which is most relevant for the Δm_{12} range with which we are most concerned. Finally, the diagonal dashed black lines from left to right respectively indicate contours corresponding to dark-matter lifetimes $\tau_2 = 10^{22}$ s, 10^{24} s, and 10^{26} s. By contrast, the solid black triangular regions are excluded by metastability constraints which require that $\tau_2 \gtrsim t_{\text{now}}$, where $t_{\text{now}} \approx 4.35 \times 10^{17}$ s is the current age of the universe. Note that in all cases, these metastability bounds for χ_2 are superseded by the results from dark-matter decay.

There are many important features contained within the plots in Fig. 3.4. Since Δm_{12} effectively quantifies departures from the standard single-component story, we shall discuss these features "from bottom up", in order of increasing Δm_{12}. First, for $\Delta m_{12} \lesssim \mathcal{O}(10\,\text{keV})$, we see that all of the features within these plots are virtually insensitive to Δm_{12} and effectively reproduce the physics of a traditional single-component dark sector with mass m_2. This behavior is certainly expected in the $\Delta m_{12} \to 0$ limit, and as a check we see that the middle panels of Fig. 3.4 correctly reproduce the results in Eqs. (3.4) and (3.5) in this limit. However, we now observe that these results persist all the way up to $\Delta m_{12} \lesssim$

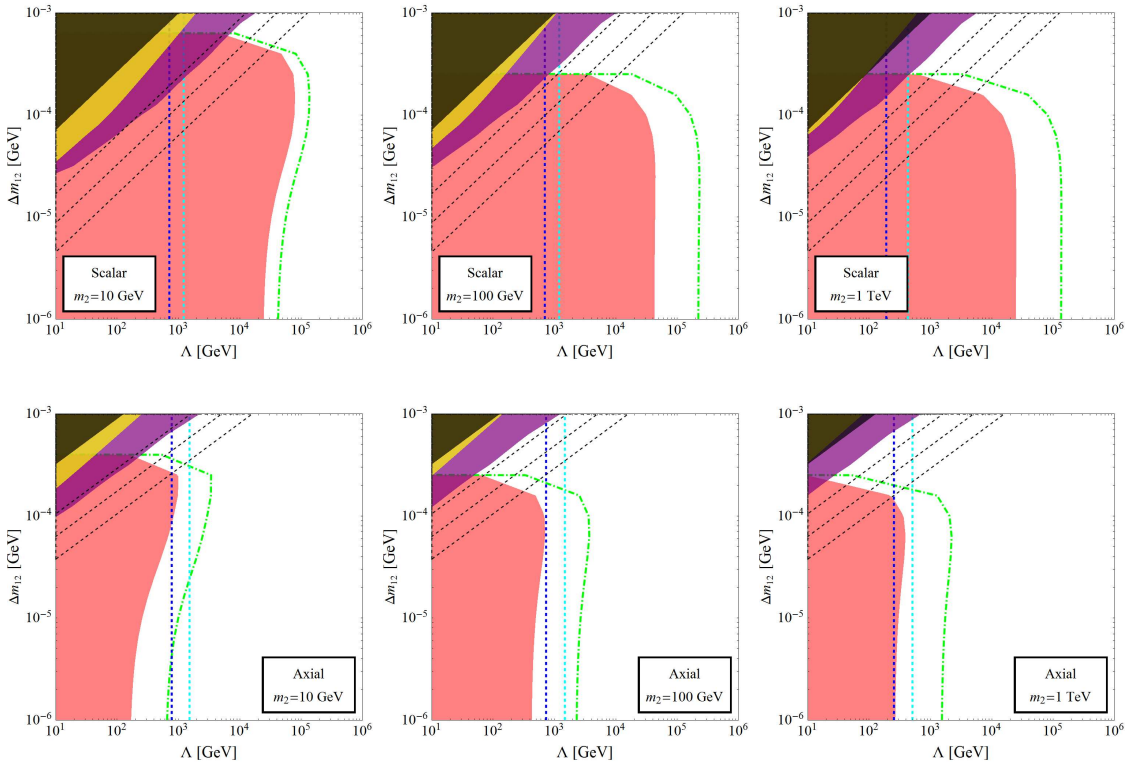

Figure 3.4: Complementary bounds on the scalar operator in Eq. (3.1) and axial-vector operator in Eq. (3.2), plotted within the associated $(\Lambda, \Delta m_{12})$ parameter spaces for $m_2 = \{10, 100, 1000\}$ GeV and $c^{(\mathrm{S})} = c^{(\mathrm{A})} = 1/\sqrt{2}$. Bounds from inelastic-scattering direct-detection experiments (pink exclusion regions), asymmetric collider production (blue and cyan vertical lines), and dark-matter decay constraints (yellow and purple exclusion regions) are shown, as discussed in the text; the green dashed lines denote the reaches of possible future direct-detection experiments, while the black dashed lines indicate dark-matter decay lifetime contours and the solid black triangular regions in each panel are excluded by metastability constraints. Remarkably, the constraints from dark-matter decay dominate in exactly those regions with relatively large Δm_{12} that lie beyond the reach of current and future direct-detection experiments, thereby illustrating the new sorts of complementarities that are possible for such multi-component dark sectors.

$\mathcal{O}(10\text{ keV})$, thereby forming an "asymptotic" region in which the physics remains largely Δm_{12}-independent. Thus, for the operators in Eq. (3.1) and (3.2), we see that it is only for $\Delta m_{12} \gtrsim \mathcal{O}(10\text{ keV})$ that the effects of dark-sector non-minimality become evident.

Second, for $\Delta m_{12} \approx \mathcal{O}(10{-}100\text{ keV})$, we see that the bounds from direct-detection experiments actually strengthen somewhat and begin to extend towards larger values of Λ. As we see from Fig. 3.4, this behavior is more pronounced for the axial-vector interaction than

the scalar interaction and for smaller values of m_2 rather than larger. This strengthening can more than double the values of Λ probed by such experiments, and is particularly important because it has the power to alter the identity of the specific dark-matter detection method which provides the leading constraint on the scale Λ as a function of Δm_{12}. For example, in the case of the axial-vector interaction with $m_2 = 10$ GeV (corresponding to the lower left panel of Fig. 3.4), we see that the monojet and mono-W/Z collider processes provide the strongest constraints for $\Delta m_{12} \lesssim \mathcal{O}(10 \text{ keV})$, but that the bounds from the direct-detection processes become increasingly strong with growing Δm_{12}, ultimately matching and perhaps even superseding the monojet collider bounds for $\Delta m_{12} \approx \mathcal{O}(100 \text{ keV})$. This strengthening of the direct-detection bounds as a function of increasing Δm_{12} is a direct consequence of the inelastic nature of the scattering process involved.

Third, moving towards even larger values $\Delta m_{12} \approx \mathcal{O}(100 - 1000 \text{ keV})$, we see that the plots in Fig. 3.4 now reveal a dramatic feature: a "ceiling" for Δm_{12} beyond which direct-detection experiments cease to provide any bounds at all and become virtually insensitive to the underlying dark-sector physics! This is also ultimately a consequence of the unique kinematics associated with inelastic down-scattering. As discussed above, for down-scattering there is a lower limit of nuclear recoil energies $E_R^{(\text{min})}$ below which the differential scattering rate dE_R/dR becomes negligible. This lower limit generally increases with increasing Δm_{ij} and is not too far below E_R^* for the non-relativistic dark-matter velocities concerned. However, a given dark-matter direct-detection experiment is typically designed to probe only a particular window of recoil energies. While the precise window of recoil energies depends on the type of experiment and the cuts imposed as part of the data analysis, this window typically falls within the range 1 keV $\lesssim E_R \lesssim$ 100 keV, as discussed above. Scattering events with recoil energies outside this range do not contribute to the measured signal-event rate. As a result, there exists a critical value of Δm_{12} beyond which the corresponding down-scattering events have a minimum recoil energy $E_R^{(\text{min})}$ exceeding 100 keV, thereby escaping detection.

Fourth, moving towards even larger values $\Delta m_{12} \lesssim \mathcal{O}(\text{MeV})$, we see from Fig. 3.4 that

the physics is now dominated by the constraints from dark-matter decay. Indeed, these constraints become significantly more stringent as Δm_{12} increases, with the maximum reach $\Lambda_{\rm max}$ scaling approximately as $(\Delta m_{12})^{7/4}$ and $(\Delta m_{12})^{9/4}$ for the scalar and axial-vector interactions, respectively. It should also be noted that these decay constraints even have a subtle dependence on m_2. Indeed, although the decay widths in Eq. (3.9) are independent of m_2 for $\Delta m_{12} \ll m_2$, we see that m_2 nevertheless enters the calculation of the total fluxes of the remnants of such decays through its appearance in the χ_2 number density $n_2 \approx \Omega_2/m_2$, where Ω_2 is the dark-matter abundance which we have assumed fixed at $\Omega_2 = \Omega_{\rm CDM} \approx 0.26$. There are, of course, further m_2-dependent corrections to both the decay widths and the injection spectra which emerge once we go beyond the $\Delta m_{12} \ll m_2$ approximation; these have been included in the plots shown in Fig. 3.4, but otherwise have a negligible effect on our results.

Finally, although we have restricted our focus in this chapter to the region $\Delta m_{12} \lesssim \mathcal{O}(\text{MeV})$, it is interesting to contemplate what occurs for even greater Δm_{12}. For $\Delta m_{12} \gtrsim \mathcal{O}(\text{MeV})$, additional decay channels for χ_2 open up in which electron/positron pairs are the end products. This only increases the decay widths for χ_2, thereby strengthening the Λ-reach of the decay-related bounds even further. For even greater values of Δm_{12}, these decay widths increase still further as additional decay channels become kinematically accessible. Ultimately, however, Δm_{12} reaches a point at which even the metastability that underlies our assumption of a non-zero present-day abundance for χ_2 is threatened. In this connection, it is important to note that this does not render such multi-component theories inconsistent; indeed, for multi-component theories it has been demonstrated that dark-matter stability is not a fundamental requirement — all that is required is a balancing of their individual component lifetimes against their cosmological abundances [111–113]. However, this shift does alter the initial assumptions that enter into the types of calculations we have performed in this work. It would nevertheless be interesting to extend this type of complementarity analysis to the constraints emerging from such a scenario.

The plots in Fig. 3.4 thus provide dramatic illustration of the new complementarities

that emerge within the context of non-minimal dark sectors. Together, the bounds from asymmetric collider-production processes, inelastic-scattering processes, and dark-matter decay processes not only help to increase the *coverage* of the relevant parameter spaces of these models but also provide useful *correlations* between these processes in those regions of parameter space in which these constraints overlap. For example, it is somewhat remarkable that the constraints from dark-matter decay emerge and dominate in exactly those regions that lie just beyond the Δm_{12} "ceiling" that caps the reach of current and future direct-detection experiments. Perhaps even more interestingly, we see that in the axial-vector case there even exists a small window within the "cross-over" region $\Delta m_{12} \approx 500$ keV (sandwiched between the bounds from direct-detection and dark-matter decay processes) in which it is the mono-W/Z *collider* bounds which provide the strongest current constraints. Taken together, this non-trivial structure is testament to the richness of the complementarities that emerge when Δm_{12} is lifted beyond the $\Delta m_{12} = 0$ axis to which the traditional complementarities that govern the physics of single-component dark sectors are restricted.

3.5 Conclusions

The idea of complementarity has long infused our thinking about the hunt for dark matter, but most work on this subject has focused on the case of single-component dark sectors. In this chapter, by contrast, we have considered the case of a multi-component dark sector, and demonstrated that there exist entirely new directions for complementarity which are absent in single-component theories. In particular, we demonstrated that the important class of interactions involving two dark components and two visible components can simultaneously contribute to *inelastic* scattering at direct-detection experiments, *asymmetric* dark-matter production at colliders, and indirect-detection signals due to dark-matter *decay*. Indeed, the latter phenomenon is completely absent for such interactions within single-component dark-matter theories, and thus represents an entirely new direction for dark-matter complementarity that emerges only within the multi-component context.

We have also demonstrated the power of these complementarity relations by consider-

ing two particular examples of such interactions, one based on a scalar (spin-independent) interaction and the other based on an axial-vector (spin-dependent) interaction. In some regimes involving large couplings or small cutoff scales Λ, we found that there is significant overlap between the regions excluded by direct- and indirect-detection limits. Taken together, these complementary probes of the dark sector combine to provide complete coverage of the relevant parameter space in this regime. By contrast, in other regimes involving smaller couplings and/or larger cutoff scales Λ, a small slice of parameter space opens up for which the dark sector escapes detection.

The existence of such regions of parameter space provides extra motivation for the development of new experimental detection strategies which are specifically targeted towards physics in these regions. For example, it would be interesting to explore how improvements in, *e.g.*, the angular resolution of future X-ray telescopes could improve the reach of indirect-detection experiments within the parameter space of non-minimal dark sectors. Likewise, designing a calibration for incorporating higher-energy nuclear recoils into threshold-detector analyses of the data from direct-detection experiments also represents a possible future method of "filling in the gap" between the bounds from direct-detection experiments and those from dark-matter decay. Finally, we note that direct-detection experiments using heavier target nuclei would in principle be capable of probing regions of parameter space with larger Δm_{12}.

Needless to say, there are also many future theoretical directions that can be pursued. One is to consider a wider class of operators beyond those considered here [47]. As we have seen in Chapter 2, the case of pseudoscalar operators, in particular, may be of particular interest due to the existence of previously unnoticed effects which are capable of overcoming the velocity suppression that would otherwise affect the corresponding direct-detection processes [114].

Another possible future direction is to consider the physics that might result from different configurations of initial abundances Ω_1 and Ω_2. In this chapter, we have focused on the case with $\Omega_1 \approx 0$ and $\Omega_2 \approx \Omega_{\rm CDM}$, since this configuration leads to the strongest possible

bounds for both direct- and indirect-detection experiments. Although this configuration may initially seem somewhat unnatural or fine-tuned, one can imagine that it is realized in cosmological scenarios in which the production of heavier dark-matter states is overwhelmingly favored relative to that of lighter dark-matter states, or in which the bulk of the dark matter is somehow excited into the higher-mass χ_2 state after production. It is nevertheless of interest to explore the phenomenology associated with more general configurations, particularly those such as $\Omega_1 \approx \Omega_2 \approx \Omega_{\rm CDM}/2$ which might be imagined as emerging from a straightforward thermal-production mechanism. Obviously, any scenario with non-zero Ω_1 will generally involve contributions from processes such as up-scattering (in addition to down-scattering) and dark-matter co-annihilation (in addition to dark-matter decay). However, it often turns out that the constraints from both of these processes are subleading within their respective classes (direct- and indirect-detection signals, respectively); indeed, co-annihilation will not even occur in scenarios (such as those associated with asymmetric dark matter [115–118]) in which the abundance of dark anti-matter does not match that of dark matter and is effectively zero at present times. Thus, in such cases, the primary effect of shifting some abundance $\Delta\Omega$ from Ω_2 to Ω_1 (thereby resulting in $\Omega_2' \equiv \Omega_2 - \Delta\Omega$) is merely to weaken the constraints from down-scattering and dark-matter decay by the factor $\Omega_2'/\Omega_2 \equiv 1 - \Delta\Omega/\Omega_2$. On logarithmic plots such as those in Fig. 3.4, such $\mathcal{O}(1)$ rescaling factors are barely noticeable. Such effects will be discussed further in Ref. [47].

A third possible future direction is to realize that even though we have restricted our attention to operators such as those in Eqs. (3.1) and (3.2) which only couple χ_i to χ_j with $i \neq j$, a more general theory involving four-fermi operators of this sort is likely to include the "diagonal" $i = j$ operators as well. In such cases, as discussed in the Introduction, both elastic and inelastic scattering events can simultaneously occur within a given direct-detection experiment, while dark-matter production at colliders can have both symmetric and asymmetric channels and the cosmic-ray fluxes relevant for indirect-detection experiments can potentially include the products of dark-matter self-annihilation as well as co-annihilation between different dark-matter species and dark-matter decay. It will

clearly be of interest to study the experimental complementarity bounds that emerge when all of these processes are included simultaneously. In particular, we note that it might even be possible to establish *correlations* between the signals from dark-matter decay and dark-matter (co-)annihilation in such a way as to potentially distinguish these signals from those which might be produced through other, unrelated astrophysical phenomena such as pulsars.

Finally, a fourth possible direction for future study is to recognize that a non-minimal dark sector may have a relatively large number of individual components which could potentially give rise to collective effects that transcend the two-component effects studied here. A dramatic example of this occurs within the so-called "Dynamical Dark Matter" (DDM) framework [111–113]; this framework gives rise to unexpected signatures not only for collider experiments [119] but also for direct-detection experiments [120] and indirect-detection experiments [121]. Studying the full parameter space of such models, especially from a complementarity perspective, should be an interesting exercise [47].

BIBLIOGRAPHY

[1] G. Bertone, D. Hooper, and J. Silk, *Particle dark matter: Evidence, candidates and constraints*, *Phys.Rept.* **405** (2005) 279–390, [hep-ph/0404175].

[2] F. Zwicky, *On the Masses of Nebulae and of Clusters of Nebulae*, *Astrophysical Journal* **86** (1937) 217.

[3] V. C. Rubin and W. K. Ford, Jr., *Rotation of the Andromeda Nebula from a Spectroscopic Survey of Emission Regions*, *Astrophysical Journal* **159** (1970) 379.

[4] M. R. Merrifield, *The rotation curve of the Milky Way to 2.5 R_0 from the thickness of the H I layer*, *Astronomical Journal* **103** (1992) 1552–1563.

[5] J. Bovy and S. Tremaine, *On the Local Dark Matter Density*, *Astrophysical Journal* **756** (2012) 89, [arXiv:1205.4033].

[6] J. I. Read, *The local dark matter density*, *Journal of Physics G Nuclear Physics* **41** (2014) 063101, [arXiv:1404.1938].

[7] S. Dodelson, *Modern Cosmology*. Academic Press. Academic Press, 2003.

[8] **Planck** Collaboration, P. Ade et al., *Planck 2013 results. XVI. Cosmological parameters*, arXiv:1303.5076.

[9] **Particle Data Group** Collaboration, J. Beringer et al., *Review of Particle Physics (RPP)*, *Phys.Rev.* **D86** (2012) 010001.

[10] J. F. Navarro, C. S. Frenk, and S. D. White, *The Structure of cold dark matter halos*, *Astrophys.J.* **462** (1996) 563–575, [astro-ph/9508025].

[11] H. Baer and X. Tata, *Weak Scale Supersymmetry: From Superfields to Scattering Events*. Cambridge University Press, 2006.

[12] L. Wang, J. M. Yang, and J. Zhu, *Dark matter in the little Higgs model under current experimental constraints from the LHC, Planck, and Xenon data*, *Phys.Rev.* **D88** (2013) 075018, [arXiv:1307.7780].

[13] S. Arrenberg, L. Baudis, K. Kong, K. T. Matchev, and J. Yoo, *Kaluza-Klein Dark Matter: Direct Detection vis-a-vis LHC (2013 update)*, arXiv:1307.6581.

[14] G. Jungman, M. Kamionkowski, and K. Griest, *Supersymmetric dark matter*, *Phys.Rept.* **267** (1996) 195–373, [hep-ph/9506380].

[15] J. Lewin and P. Smith, *Review of mathematics, numerical factors, and corrections for dark matter experiments based on elastic nuclear recoil*, *Astropart.Phys.* **6** (1996) 87–112.

[16] D. Hooper, *TASI 2008 Lectures on Dark Matter*, arXiv:0901.4090.

[17] N. Weiner, "Dark matter theory." Video lectures given at TASI, 2009.

[18] J. L. Feng, *Dark Matter Candidates from Particle Physics and Methods of Detection*, *Annual Review of Astronomy and Astrophysics* **48** (2010) 495–545, [arXiv:1003.0904].

[19] R. W. Schnee, *Introduction to Dark Matter Experiments*, in *Physics of the Large and the Small: TASI 2009* (C. Csaki and S. Dodelson, eds.), pp. 775–829, Mar., 2011. arXiv:1101.5205.

[20] P. J. Fox and E. Poppitz, *Leptophilic Dark Matter*, *Phys.Rev.* **D79** (2009) 083528, [arXiv:0811.0399].

[21] S. Arrenberg, H. Baer, V. Barger, L. Baudis, D. Bauer, et al., *Working Group Report: Dark Matter Complementarity*, arXiv:1310.8621.

[22] J. Kopp, V. Niro, T. Schwetz, and J. Zupan, *Leptophilic Dark Matter in Direct Detection Experiments and in the Sun*, *PoS* **IDM2010** (2011) 118, [arXiv:1011.1398].

[23] D. Schmidt, T. Schwetz, and T. Toma, *Direct Detection of Leptophilic Dark Matter in a Model with Radiative Neutrino Masses*, *Phys.Rev.* **D85** (2012) 073009, [arXiv:1201.0906].

[24] C. Wainwright and S. Profumo, *The Impact of a strongly first-order phase transition on the abundance of thermal relics*, *Phys.Rev.* **D80** (2009) 103517, [arXiv:0909.1317].

[25] D. Tucker-Smith and N. Weiner, *Inelastic dark matter*, *Phys.Rev.* **D64** (2001) 043502, [hep-ph/0101138].

[26] S. Chang, G. D. Kribs, D. Tucker-Smith, and N. Weiner, *Inelastic Dark Matter in Light of DAMA/LIBRA*, *Phys.Rev.* **D79** (2009) 043513, [arXiv:0807.2250].

[27] B. Batell, M. Pospelov, and A. Ritz, *Direct Detection of Multi-component Secluded WIMPs*, *Phys.Rev.* **D79** (2009) 115019, [arXiv:0903.3396].

[28] K. M. Zurek, *Multi-Component Dark Matter*, *Phys.Rev.* **D79** (2009) 115002, [arXiv:0811.4429].

[29] M. A. Shifman, A. Vainshtein, and V. I. Zakharov, *Remarks on Higgs Boson Interactions with Nucleons*, *Phys.Lett.* **B78** (1978) 443.

[30] J. Engel, S. Pittel, and P. Vogel, *Nuclear physics of dark matter detection*, *Int.J.Mod.Phys.* **E1** (1992) 1–37.

[31] R. Jaffe and A. Manohar, *The G(1) Problem: Fact and Fantasy on the Spin of the Proton*, *Nucl.Phys.* **B337** (1990) 509–546.

[32] J. R. Ellis, K. A. Olive, and C. Savage, *Hadronic Uncertainties in the Elastic Scattering of Supersymmetric Dark Matter*, *Phys.Rev.* **D77** (2008) 065026, [arXiv:0801.3656].

[33] P. Agrawal, Z. Chacko, C. Kilic, and R. K. Mishra, *A Classification of Dark Matter Candidates with Primarily Spin-Dependent Interactions with Matter*, arXiv:1003.1912.

[34] J. Fan, M. Reece, and L.-T. Wang, *Non-relativistic effective theory of dark matter direct detection*, *JCAP* **1011** (2010) 042, [arXiv:1008.1591].

[35] M. Freytsis and Z. Ligeti, *On dark matter models with uniquely spin-dependent detection possibilities*, *Phys.Rev.* **D83** (2011) 115009, [arXiv:1012.5317].

[36] J. Kumar and D. Marfatia, *Matrix element analyses of dark matter scattering and annihilation*, *Bull.Astron.Inst.Neth.* **D88** (2013) 014035, [arXiv:1305.1611].

[37] **SMC** Collaboration, B. Adeva et al., *Polarization of valence and nonstrange sea quarks in the nucleon from semi-inclusive spin asymmetries*, *Phys.Lett.* **B369** (1996) 93–100.

[38] **SMC** Collaboration, B. Adeva et al., *Polarized quark distributions in the nucleon from semiinclusive spin asymmetries*, *Phys.Lett.* **B420** (1998) 180–190, [hep-ex/9711008].

[39] **HERMES** Collaboration, A. Airapetian et al., *Quark helicity distributions in the nucleon for up, down, and strange quarks from semi-inclusive deep-inelastic scattering*, *Phys.Rev.* **D71** (2005) 012003, [hep-ex/0407032].

[40] G. Bimonte, E. Calloni, and L. Rosa, *The gravity of magnetic stresses and energy*, *Phys.Rev.* **D77** (2008) 044026, [arXiv:0707.1077].

[41] **COMPASS** Collaboration, M. Alekseev et al., *Quark helicity distributions from longitudinal spin asymmetries in muon-proton and muon-deuteron scattering*, *Phys.Lett.* **B693** (2010) 227–235, [arXiv:1007.4061].

[42] **QCDSF** Collaboration, G. S. Bali et al., *Strangeness Contribution to the Proton Spin from Lattice QCD*, *Phys.Rev.Lett.* **108** (2012) 222001, [arXiv:1112.3354].

[43] H.-Y. Cheng, *Low-energy Interactions of Scalar and Pseudoscalar Higgs Bosons With Baryons*, *Phys.Lett.* **B219** (1989) 347.

[44] H.-Y. Cheng and C.-W. Chiang, *Revisiting Scalar and Pseudoscalar Couplings with Nucleons*, *JHEP* **1207** (2012) 009, [arXiv:1202.1292].

[45] Y. Bai, P. J. Fox, and R. Harnik, *The Tevatron at the Frontier of Dark Matter Direct Detection*, *JHEP* **1012** (2010) 048, [arXiv:1005.3797].

[46] S. J. Brodsky, J. R. Ellis, and M. Karliner, *Chiral Symmetry and the Spin of the Proton*, *Phys.Lett.* **B206** (1988) 309.

[47] K. R. Dienes, J. Kumar, B. Thomas, D. Yaylali, et al. in progress.

[48] T. Lin, E. W. Kolb, and L.-T. Wang, *Probing dark matter couplings to top and bottom quarks at the LHC*, *Phys.Rev.* **D88** (2013) 063510, [arXiv:1303.6638].

[49] M. W. Goodman and E. Witten, *Detectability of Certain Dark Matter Candidates*, *Phys.Rev.* **D31** (1985) 3059.

[50] N. Anand, A. L. Fitzpatrick, and W. Haxton, *Model-independent WIMP Scattering Responses and Event Rates: A Mathematica Package for Experimental Analysis*, *Phys.Rev.* **C89** (2014) 065501, [arXiv:1308.6288].

[51] **COUPP** Collaboration, E. Behnke et al., *First dark matter search results from a 4-kg CF_3I bubble chamber operated in a deep underground site*, *Phys.Rev.* **D86** (2012) 052001, [arXiv:1204.3094].

[52] **SIMPLE** Collaboration, M. Felizardo et al., *Final Analysis and Results of the Phase II SIMPLE Dark Matter Search*, *Physical Review Letters* **108** (2012) 201302, [arXiv:1106.3014].

[53] **PICASSO** Collaboration, S. Archambault et al., *Constraints on Low-Mass WIMP Interactions on ^{19}F from PICASSO*, *Phys.Lett.* **B711** (2012) 153–161, [arXiv:1202.1240].

[54] R. Neilson, "Coupp: Bubble chambers for dark matter detection." Talk given at Aspen 2013, 2013.

[55] J. Edsjo and P. Gondolo, *Neutralino relic density including coannihilations*, *Phys.Rev.* **D56** (1997) 1879–1894, [hep-ph/9704361].

[56] A. Birkedal, K. Matchev, and M. Perelstein, *Dark matter at colliders: A Model independent approach*, *Phys.Rev.* **D70** (2004) 077701, [hep-ph/0403004].

[57] J. L. Feng, S. Su, and F. Takayama, *Lower limit on dark matter production at the large hadron collider*, *Phys.Rev.Lett.* **96** (2006) 151802, [hep-ph/0503117].

[58] J. Goodman, M. Ibe, A. Rajaraman, W. Shepherd, T. M. Tait, et al., *Constraints on Light Majorana dark Matter from Colliders*, *Phys.Lett.* **B695** (2011) 185–188, [arXiv:1005.1286].

[59] P. J. Fox, R. Harnik, J. Kopp, and Y. Tsai, *Missing Energy Signatures of Dark Matter at the LHC*, *Phys.Rev.* **D85** (2012) 056011, [arXiv:1109.4398].

[60] J. Goodman and W. Shepherd, *LHC Bounds on UV-Complete Models of Dark Matter*, arXiv:1111.2359.

[61] Y. Bai and T. M. Tait, *Searches with Mono-Leptons*, *Phys.Lett.* **B723** (2013) 384–387, [arXiv:1208.4361].

[62] **ATLAS** Collaboration, G. Aad et al., *Search for dark matter candidates and large extra dimensions in events with a jet and missing transverse momentum with the ATLAS detector*, *JHEP* **1304** (2013) 075, [arXiv:1210.4491].

[63] **ATLAS** Collaboration, *Search for New Phenomena in Monojet plus Missing Transverse Momentum Final States using 10fb-1 of pp Collisions at sqrts=8 TeV with the ATLAS detector at the LHC*, Tech. Rep. ATLAS-CONF-2012-147, CERN, Geneva, 2012.

[64] **CMS** Collaboration, S. Chatrchyan et al., *Search for dark matter and large extra dimensions in monojet events in pp collisions at* $\sqrt{s} = 7$ *TeV*, *JHEP* **1209** (2012) 094, [arXiv:1206.5663].

[65] **CMS** Collaboration, *Search for new physics in monojet events in pp collisions at sqrts= 8 TeV*, Tech. Rep. CMS-PAS-EXO-12-048, CERN, Geneva, 2013.

[66] **ATLAS** Collaboration, G. Aad et al., *Search for dark matter in events with a hadronically decaying W or Z boson and missing transverse momentum in pp collisions at* $\sqrt{s}$*=8 TeV with the ATLAS detector*, *Phys.Rev.Lett.* **112** (2014) 041802, [arXiv:1309.4017].

[67] **ATLAS** Collaboration, G. Aad et al., *Search for dark matter in events with a Z boson and missing transverse momentum in pp collisions at* $\sqrt{s}$*=8 TeV with the ATLAS detector*, arXiv:1404.0051.

[68] K. Cheung, P.-Y. Tseng, Y.-L. S. Tsai, and T.-C. Yuan, *Global Constraints on Effective Dark Matter Interactions: Relic Density, Direct Detection, Indirect Detection, and Collider*, *JCAP* **1205** (2012) 001, [arXiv:1201.3402].

[69] N. Zhou, D. Berge, and D. Whiteson, *Mono-everything: combined limits on dark matter production at colliders from multiple final states*, *Phys.Rev.* **D87** (2013) 095013, [arXiv:1302.3619].

[70] J. Goodman, M. Ibe, A. Rajaraman, W. Shepherd, T. M. Tait, et al., *Constraints on Dark Matter from Colliders*, *Phys.Rev.* **D82** (2010) 116010, [arXiv:1008.1783].

[71] J. Alwall, M. Herquet, F. Maltoni, O. Mattelaer, and T. Stelzer, *MadGraph 5 : Going Beyond*, *JHEP* **1106** (2011) 128, [arXiv:1106.0522].

[72] J. Pumplin, D. Stump, J. Huston, H. Lai, P. M. Nadolsky, et al., *New generation of parton distributions with uncertainties from global QCD analysis*, *JHEP* **0207** (2002) 012, [hep-ph/0201195].

[73] H. An, X. Ji, and L.-T. Wang, *Light Dark Matter and Z' Dark Force at Colliders*, *JHEP* **1207** (2012) 182, [arXiv:1202.2894].

[74] H. An, R. Huo, and L.-T. Wang, *Searching for Low Mass Dark Portal at the LHC*, *Phys.Dark Univ.* **2** (2013) 50–57, [arXiv:1212.2221].

[75] T. Hur, H.-S. Lee, and S. Nasri, *A Supersymmetric U(1)-prime model with multiple dark matters*, *Phys.Rev.* **D77** (2008) 015008, [arXiv:0710.2653].

[76] D. Feldman, Z. Liu, P. Nath, and G. Peim, *Multicomponent Dark Matter in Supersymmetric Hidden Sector Extensions*, *Phys.Rev.* **D81** (2010) 095017, [arXiv:1004.0649].

[77] P. T. Winslow, K. Sigurdson, and J. N. Ng, *Multi-State Dark Matter from Spherical Extra Dimensions*, *Phys.Rev.* **D82** (2010) 023512, [arXiv:1005.3013].

[78] D. Chialva, P. B. Dev, and A. Mazumdar, *Multiple dark matter scenarios from ubiquitous stringy throats*, *Phys.Rev.* **D87** (2013) 063522, [arXiv:1211.0250].

[79] F. Chen, J. M. Cline, and A. R. Frey, *Nonabelian dark matter: Models and constraints*, *Phys.Rev.* **D80** (2009) 083516, [arXiv:0907.4746].

[80] X. Gao, Z. Kang, and T. Li, *The Supersymmetric Standard Models with Decay and Stable Dark Matters*, *Eur.Phys.J.* **C69** (2010) 467–480, [arXiv:1001.3278].

[81] T. Han and R. Hempfling, *Messenger sneutrinos as cold dark matter*, *Phys.Lett.* **B415** (1997) 161–169, [hep-ph/9708264].

[82] L. J. Hall, T. Moroi, and H. Murayama, *Sneutrino cold dark matter with lepton number violation*, *Phys.Lett.* **B424** (1998) 305–312, [hep-ph/9712515].

[83] D. Tucker-Smith and N. Weiner, *The Status of inelastic dark matter*, *Phys.Rev.* **D72** (2005) 063509, [hep-ph/0402065].

[84] F. Chen, J. M. Cline, and A. R. Frey, *A New twist on excited dark matter: Implications for INTEGRAL, PAMELA/ATIC/PPB-BETS, DAMA*, *Phys.Rev.* **D79** (2009) 063530, [arXiv:0901.4327].

[85] D. P. Finkbeiner, T. R. Slatyer, N. Weiner, and I. Yavin, *PAMELA, DAMA, INTEGRAL and Signatures of Metastable Excited WIMPs*, *JCAP* **0909** (2009) 037, [arXiv:0903.1037].

[86] P. W. Graham, R. Harnik, S. Rajendran, and P. Saraswat, *Exothermic Dark Matter*, *Phys.Rev.* **D82** (2010) 063512, [arXiv:1004.0937].

[87] M. Pospelov and A. Ritz, *Higgs decays to dark matter: beyond the minimal model*, *Phys.Rev.* **D84** (2011) 113001, [arXiv:1109.4872].

[88] C. Cheung and Y. Nomura, *Higgs Descendants*, *Phys.Rev.* **D86** (2012) 015004, [arXiv:1112.3043].

[89] Y. Bai, P. Draper, and J. Shelton, *Measuring the Invisible Higgs Width at the 7 and 8 TeV LHC*, *JHEP* **1207** (2012) 192, [arXiv:1112.4496].

[90] J. Wang, *Determining the masses of invisible particles: Application to Higgs boson invisible decay*, *Phys.Rev.* **D89** (2014) 093019, [arXiv:1311.3442].

[91] **LUX** Collaboration, D. Akerib et al., *First results from the LUX dark matter experiment at the Sanford Underground Research Facility*, *Phys.Rev.Lett.* **112** (2014) 091303, [arXiv:1310.8214].

[92] U. G. Meissner, *Recent developments in chiral perturbation theory*, *Rept.Prog.Phys.* **56** (1993) 903–996, [hep-ph/9302247].

[93] G. Ecker, *Chiral perturbation theory*, *Prog.Part.Nucl.Phys.* **35** (1995) 1–80, [hep-ph/9501357].

[94] A. Pich, *Chiral perturbation theory*, *Rept.Prog.Phys.* **58** (1995) 563–610, [hep-ph/9502366].

[95] G. Colangelo and G. Isidori, *An Introduction to ChPT*, hep-ph/0101264.

[96] S. Scherer, *Introduction to chiral perturbation theory*, *Adv.Nucl.Phys.* **27** (2003) 277, [hep-ph/0210398].

[97] J. Gasser and H. Leutwyler, *On the low energy structure of QCD*, *Physics Letters B* **125** (1983) 321–324.

[98] H. Leutwyler, *On the foundations of chiral perturbation theory*, *Annals Phys.* **235** (1994) 165–203, [hep-ph/9311274].

[99] R. Kaiser, *Anomalies and WZW term of two flavor QCD*, *Phys.Rev.* **D63** (2001) 076010, [hep-ph/0011377].

[100] H. Fearing and S. Scherer, *Extension of the chiral perturbation theory meson Lagrangian to order p^6*, *Phys.Rev.* **D53** (1996) 315–348, [hep-ph/9408346].

[101] J. Bijnens, G. Colangelo, and G. Ecker, *The Mesonic chiral Lagrangian of order p^6*, *JHEP* **9902** (1999) 020, [hep-ph/9902437].

[102] T. Ebertshauser, H. Fearing, and S. Scherer, *The Anomalous chiral perturbation theory meson Lagrangian to order p^6 revisited*, *Phys.Rev.* **D65** (2002) 054033, [hep-ph/0110261].

[103] J. Bijnens, L. Girlanda, and P. Talavera, *The Anomalous chiral Lagrangian of order p^6*, *Eur.Phys.J.* **C23** (2002) 539–544, [hep-ph/0110400].

[104] M. Cirelli, G. Corcella, A. Hektor, G. Hutsi, M. Kadastik, et al., *PPPC 4 DM ID: A Poor Particle Physicist Cookbook for Dark Matter Indirect Detection*, *JCAP* **1103** (2011) 051, [arXiv:1012.4515].

[105] R. Gaitskell et al. **DM Tools Limit Plotter**. http://dmtools.brown.edu:8080.

[106] D. C. Malling et al., *After LUX: The LZ Program*, arXiv:1110.0103.

[107] T. Sjostrand, S. Mrenna, and P. Z. Skands, *PYTHIA 6.4 Physics and Manual*, *JHEP* **0605** (2006) 026, [hep-ph/0603175].

[108] S. Ovyn, X. Rouby, and V. Lemaitre, *DELPHES, a framework for fast simulation of a generic collider experiment*, arXiv:0903.2225.

[109] D. Gruber, J. Matteson, L. Peterson, and G. Jung, *The spectrum of diffuse cosmic hard X-rays measured with HEAO-1*, astro-ph/9903492.

[110] L. Bouchet, E. Jourdain, J. Roques, A. Strong, R. Diehl, et al., *INTEGRAL SPI All-Sky View in Soft Gamma Rays: Study of Point Source and Galactic Diffuse Emissions*, arXiv:0801.2086.

[111] K. R. Dienes and B. Thomas, *Dynamical Dark Matter: I. Theoretical Overview*, *Phys.Rev.* **D85** (2012) 083523, [arXiv:1106.4546].

[112] K. R. Dienes and B. Thomas, *Dynamical Dark Matter: II. An Explicit Model*, *Phys.Rev.* **D85** (2012) 083524, [arXiv:1107.0721].

[113] K. R. Dienes and B. Thomas, *Phenomenological Constraints on Axion Models of Dynamical Dark Matter*, *Phys.Rev.* **D86** (2012) 055013, [arXiv:1203.1923].

[114] K. R. Dienes, J. Kumar, B. Thomas, and D. Yaylali, *Overcoming Velocity Suppression in Dark-Matter Direct-Detection Experiments*, arXiv:1312.7772.

[115] K. Petraki and R. R. Volkas, *Review of asymmetric dark matter*, *Int.J.Mod.Phys.* **A28** (2013) 1330028, [arXiv:1305.4939].

[116] D. B. Kaplan, *A Single explanation for both the baryon and dark matter densities*, *Phys.Rev.Lett.* **68** (1992) 741–743.

[117] R. Kitano and I. Low, *Grand unification, dark matter, baryon asymmetry, and the small scale structure of the universe*, hep-ph/0503112.

[118] D. E. Kaplan, M. A. Luty, and K. M. Zurek, *Asymmetric Dark Matter*, *Phys.Rev.* **D79** (2009) 115016, [arXiv:0901.4117].

[119] K. R. Dienes, S. Su, and B. Thomas, *Distinguishing Dynamical Dark Matter at the LHC*, *Phys.Rev.* **D86** (2012) 054008, [arXiv:1204.4183].

[120] K. R. Dienes, J. Kumar, and B. Thomas, *Direct Detection of Dynamical Dark Matter*, *Phys.Rev.* **D86** (2012) 055016, [arXiv:1208.0336].

[121] K. R. Dienes, J. Kumar, and B. Thomas, *Dynamical Dark Matter and the positron excess in light of AMS results*, *Phys.Rev.* **D88** (2013) 103509, [arXiv:1306.2959].